Highly Compact and Low Mutual Coupling MIMO Antennas

A

Thesis Submitted

in Fulfilment of the Requirements

for the Dual Degree

M.S. [Engineering]

&

DOCTOR OF PHILOSOPHY

By

Mohit Mishra

Department of Electronics and Electrical Engineering

Indian Institute of Technology Guwahati

Guwahati, India.

January, 2023

Dedicated to

My Beloved Country 'Bharat'
and its people

for making me learn

वसुधैव कुटुम्बकम ***(whole world is a family)***

Certificate

This is to certify that the thesis entitled '**Highly Compact and Low Mutual Coupling MIMO Antennas**' is submitted by **Mohit Mishra**, a student with roll no. 156302008 in the Department of Electronics and Electrical Engineering, Indian Institute of Technology Guwahati, for the award of the **M.S. [Engineering]** and **Doctor of Philosophy** dual degree. He has carried out thesis work under my supervision and guidance. The thesis has fulfilled all requirements as per the regulations laid out by the Institute. The results embodied in this thesis have not been submitted to any other university or Institute for the award of any degree or diploma.

Prof. Rakhesh Singh Kshetrimayum

Dept. of Electronics and Electrical Engineering,

Indian Institute of Technology Guwahati,

Assam - 781039.

Acknowledgements

Words are less to express my gratitude to Prof. Rakhesh Singh Kshetrimayum (my supervisor) for providing me with an opportunity to be a part of his research team. I sincerely appreciate the continuous support, guidance, encouragement, and inspiration from his side throughout the academic program. His comments and suggestions on my work have added deep insights to my knowledge base, and I do not hesitate to admit that my Ph.D. journey would have been challenging without tremendous support from his side. I want to thank him for giving me freedom and liberty; otherwise, I could not have followed my other interests. I could serve well in various positions on the Students Council and learn many important things because he always appreciated my interest in extracurricular activities. Many thanks to him for his overall support.

At this phase of life, I would like to acknowledge the contributions of my teachers, including my parents, who have shaped my personality and helped me believe in myself at various levels, from elementary to higher education. A few names in this line are Shri Vishambhar Singh, Shri Anil Kumar Singh, Dr. Soma Das, and Dr. Nipun Kumar Mishra. I owe tremendous gratitude to the Government of India for providing free education from sixth to twelfth grades and highly subsidized higher education at the Central University of Chhattisgarh, India, and IIT Guwahati, India.

I take this opportunity to thank my Doctoral Committee members Dr. R. K. Sonkar, Prof. S. K. Nayak, Dr. Nagarjuna Nallam, and Dr. Salil Kashyap, for annually reviewing my work and providing insightful comments and suggestions. I am grateful to all my collaborators for their input and suggestions in improving the manuscripts. Thanks to the Head, staff, and officers of the EEE department, IIT Guwahati, for their support and help in the laboratory and official works.

My heartfelt gratitude goes to Prof. A. Alphonse, Prof. K. P. Esselle, Prof. M. S. Sharawi, and Prof. A. A. Kishk for their expert advice and comments on improving the works. I thank Dr. S. Chaudhuri, Mr. Utpal Sarma, Dr. K. Dutta, Mr. Sai Kiran, Mr. A. M. Sonagara, Mr. H. Chel, and Dr. S. Bhunia for their support and assistance.

I must thank Prof. T. G. Sitharam, former Director of IIT Guwahati and present Chairman of All India Council for Technical Education, India, for listening to me and for the proactive consideration of my proposals in the greater interest of the students's welfare. Many thanks to him for his guidance on the personal front as well. I thank all the Deputy Directors, Deans, Professors, my colleagues in the Students Council, and the student affairs section for their help and support during various events and student council works.

I express my heartfelt thanks and gratitude to Prof. Uday Shankar Dixit for showering his light full of vast and rich experiences during various conversations. I thank him for his guidance and continued support throughout my stay at IIT Guwahati. I must thank Dr. Gagan Kumar, Prof. V. V. Dasu, and many others for asking me about my well-being and the progress of my Ph.D. thesis from time to time. I thank my colleagues Dr. Pyarimohan Dehury, Mr. Rahul Sharma, Dr. Bikash Shah, Dr. Anirban Bhowal, Dr. Arijit Bhattacharjee, Mr. Aditya Pawar for their support and fantastic company during IIT Guwahati days.

I thank all the people who have helped and supported me directly or indirectly in becoming a better person with time.

This acknowledgement would remain incomplete without expressing my most profound gratitude and indebtedness to my parents, brother, and cousins for their blessings, love, and continued support and for having great faith in me. It is difficult for me to describe in words how much they meant to me.

Mohit Mishra

Abstract

Multiple-input multiple-output (MIMO) is an efficient technology that can meet the demands of the modern communication system, such as higher data rate and less probability of error in data transmission. However, there are issues associated with the deployment of multiple antennas on both the transmitter and receiver sides. One such major challenge is increased electromagnetic interaction between antenna elements in a compact MIMO system, leading to increased mutual coupling (MC) and antenna correlation coefficient (ACC). The increase in the MC and the ACC between closely packed antenna elements of a compact MIMO antenna degrades the performance of a MIMO communication system. Therefore, this thesis begins with an introduction emphasizing the relevance of MIMO communication systems, followed by a discussion of the cause of the MC and its impact on MIMO communications' performance. A detailed study of the existing MIMO antenna design methodologies is carried out. It includes electromagnetic band-gap (EBG) structures, defected ground structures (DGS), neutralization line (NL) technique, array decoupling surfaces (ADSs), and substrate-integrated waveguide-based MIMO antennas. Compared to NLs for MC reduction, EBGs & isolators require much more space between antennas to accommodate them. Two NL-based MIMO antenna designs are presented in this thesis. The first is a dual-band two-port MIMO antenna, while the second is a six-port MIMO antenna. The mutual coupling between antenna ports in the two-port and six-port planar MIMO antenna is reduced by connecting adjacent antennas through NLs. ADSs or superstrates employed in isolation enhancement are generally placed at a certain height above the antenna array due to the associated operating principle. Consequently, an additional layer gets added and increases the MIMO antenna profile. Furthermore, single negative (SNG) meta-grid lines (MGLs) are proposed for mutual coupling reduction. The SNG MGLs can reduce the MC in the two-port printed monopole MIMO antennas and the two-port MIMO DRAs with minor structural modifications. This technique of the MC reduction between antennas neither necessitates extra space between antenna elements, unlike the EBGs and the isolators, nor the installation of additional layers such as the ADS, enabling compact design of two-port MIMO antennas. It is noted that the proper placement of a double-side copper cladded substrate between two half-split cylindrical dielectric resonator antennas (CDRAs) can reduce the MC significantly and provide a space-efficient approach for the MC reduction in MIMO DRAs. One such two-port half-split DRA with overall size miniaturization is presented in chapter 5. The substrate-integrated waveguide (SIW) cavity-based antennas possess a noteworthy feature of size miniaturization by employing fraction mode SIWs (half-mode, quarter-mode, etc.). In addition, SIW cavities are known for their low profile, ease of integration, and self-consistent electrical shielding. Hence, SIW-based MIMO antennas do not require extra decoupling units when designed carefully and can achieve MC below -15 dB with size compactness. One such sector-shaped compact $\pi/8$ partial SIW cavity antenna from the TM_{220} diagonal mode of the SIW cavity is designed. This design technique offers 61% size miniaturization compared to the SIW rectangular cavity in its complete mode configuration. The proposed radiator is used to

design an 8-port SIW-based compact MIMO antenna in chapter 6.

Furthermore, the performance of the above-mentioned multi-port antennas for MIMO communications has been described in terms of channel capacity loss, diversity measure, and sum-rate loss. This thesis thoroughly investigated all the MIMO antenna designs with their operation and utility.

Contents

List of Figures

List of Tables

List of Acronyms

ACC	Antenna correlation coefficient
ADS	Array decoupling surface
BW	Bandwidth
CCL	Channel capacity loss
CPW	Coplanar waveguide
DG	Diversity gain
DGS	Defected Ground Structures
DM	Multiplexing gain
DO	Diversity order
DRA	Dielectric resonator antenna
EBG	Electromagnetic band-gap
ECC	Envelope correlation coefficient
EM	Electromagnetic or electromagnetism
FSS	Frequency selective surface
i.i.d.	Independent and identically distributed
LTE	Long term evolution
MIMO	Multiple-input multiple-output
MNG	Mu-negative
MS	Metasurface
MTM	Metamaterial
NL	Neutralization line
PEC	Perfect Electric Conductor
PIFA	Planar inverted F-antennas
SIW	Substrate-integrated waveguide
SRL	Sum rate loss
SNG	Single negative
SNR	Signal to noise ratio

SRR	Split-ring resonators
TM	Transverse magnetic
UAV	Unmanned aerial vehicle
WLAN	Wireless local area network
WWAN	Wireless wide area network
XPD	Cross polarization discrimination

List of Symbols

ε_r	Relative permittivity
$\tan\delta$	Loss-tangent
Q	Quality factor
Ω	Ohm
k_x	Wave number along X- axis
k_y	Wave number along Y- axis
k_z	Wave number along Z- axis
θ	Theta
ϕ	Phi
$\vec{E}_\theta$	Theta component of E-field radiation pattern
$\vec{E}_\phi$	Phi component of E-field radiation pattern
$\det(\square)$	Determinant of a matrix
$\mathrm{tr}(\square)$	Trace of a matrix
$\|\square\|_F$	Frobenius norm of a matrix
%	Percentage
λ_h	Highest operating wavelength

1

Introduction

Multiple-input multiple-output (MIMO) is an efficient technology that can fulfill the requirements of modern communication systems, such as high data-rate communication with reduced transmission error. However, there are challenges associated with the deployment of multiple antennas at the transmitter and receiver sides. One such challenge is the increased electromagnetic interaction between the elements, especially of a size-reduced MIMO antenna, which leads to high mutual coupling or low isolation. The mutual coupling mechanisms for MIMO antennas in the transmit and receive modes are explained, followed by a discussion of the adverse effects of the mutual coupling on MIMO communication systems.

1.1 Introduction

Multiple-input multiple-output (MIMO) is a communication technology that can meet the requirements of high throughput and robust connectivity in modern communication systems [1]. Systems equipped with this technology offer two main advantages: a) Diversity gain, which results in improved link reliability and less probability of error in data transmission and b) Multiplexing gain, which results in increased spectral efficiency, i.e., an increase in the channel capacity, without increasing the bandwidth [2].

Traditionally, multiple antennas have been used to increase diversity and combat channel fading. In MIMO systems, each pair of transmitting and receiving antennas can provide an independent signal path between a pair of transceivers. Hence, by sending multiple independently faded replicas of the same data through different paths, the reliability of reception at the receiver can be improved. For example, for a slow independent identically distributed (i.i.d.) Rayleigh fading channel with one transmit and multiple (n) receive antennas, the diversity gain is n, considering that links between antenna pairs fade independently. Hence, the average error probability will decay at the rate of $1/SNR^n$, in contrast to the average error probability for the single-input single-output (SISO) fading channel, which is $1/SNR$ [2]. Here, SNR stands for signal-to-noise ratio at the receiver end. Therefore, diversity is a means to combat channel fading. In a MIMO system with N_T transmit and N_R receive antennas (assuming the MIMO channel is i.i.d. Rayleigh faded), the maximal diversity gain is $N_T \times N_R$ [3].

As a different line of thought, fading is considered to be beneficial, as it increases the degrees of freedom available for communication. Independent fading of path gains and a well-conditioned channel matrix can create multiple parallel spatial channels [4]. Hence, the data rate can be increased by transmitting independent information streams in parallel. This effect is known as spatial multiplexing, and the improvement in data rate is referred to as multiplexing gain. The increase in data rate by exploiting spatial multiplexing does not require any additional spectrum or transmitted power as it can be increased by increasing the number of antenna elements in an i.i.d. Rayleigh faded MIMO channel [5, 6].

Implementation of MIMO technology requires the deployment of closely spaced multiple antennas on both the transmitter and receiver sides. However, there are challenges associated with this. One such challenge is that of increased electromagnetic interaction between the elements of a compact MIMO antenna, which leads to low isolation or high mutual coupling [7].

1.2 Mutual Coupling

The electromagnetic interaction between the antenna elements in a MIMO antenna or antenna array causes mutual coupling. The mutual coupling depends on the following factors [8]:

(i) Radiation pattern of antenna elements

(ii) Relative separation between antenna elements

(iii) Relative orientation of antenna elements

1.2.1 Mutual Coupling Mechanism in a Transmitting MIMO Antenna

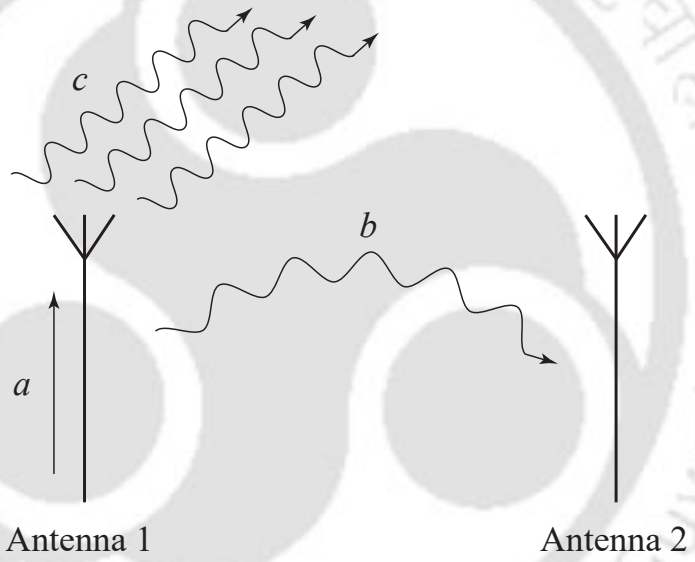

Fig. 1.1: A MIMO antenna system with two elements in the transmitting mode.

In the transmit mode, all elements of a MIMO antenna are supposed to radiate the signal only, but this does not happen under practical scenarios. While transmitting, antenna elements also receive a part of the transmitted signal from the nearby antennas. As depicted in the two-antenna system of Fig. 1.1, only Antenna 1 is excited with Antenna 2 in its proximity. The amount of power supplied to Antenna 1 is denoted by a, whereas the power radiated from it into the free space is labeled as c. The nearby Antenna 2 also receives some amount of the radiated power (labeled as b) from Antenna 1 due to the electromagnetic (EM) interactions between the closely placed antennas. The power received by Antenna 2 would get partially scattered into its vicinity. Again, Antenna 1 will receive a part of the scattered energy (from Antenna

2) because of the mutual coupling. Such a process will continue indefinitely. Thus, when both the antennas are excited, the EM radiation will be the sum of the radiated fields from the individual antennas and the re-scattered radiations from both the antenna elements [8, 9].

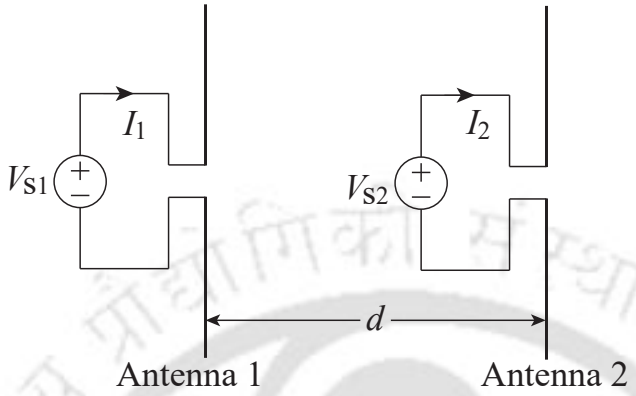

Fig. 1.2: A MIMO antenna system comprising two dipole antennas in the transmitting mode.

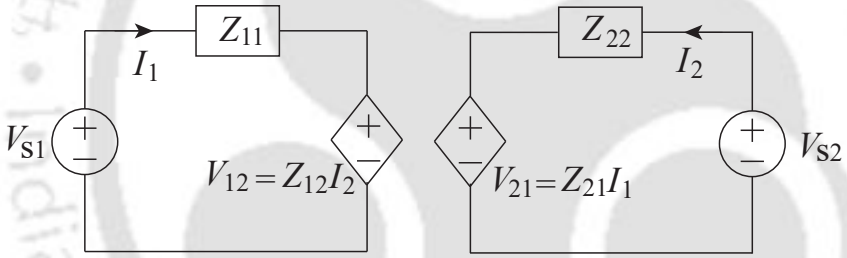

Fig. 1.3: The equivalent circuit model of a two-element MIMO antenna system considering the mutual coupling.

A two-element antenna system comprising two dipole antennas is considered for theoretical circuit modeling of the mutual coupling effect, as shown in Fig. 1.2 [9]. Antenna elements are separated by a distance d. The equivalent circuit of these antennas with the mutual coupling is shown in Fig. 1.3. Let V_{S1} and V_{S2} are the excitation voltages of Antenna 1 and Antenna 2, respectively. Z_{11} and Z_{22} are the antenna impedances of Antenna 1 and Antenna 2, respectively. The mutual coupling effect is considered in terms of coupled voltage. V_{12} is the coupled voltage on Antenna 1 due to Antenna 2, and V_{21} is the same on Antenna 2 because of Antenna 1. The coupled voltage in terms of the mutual impedance can be expressed by (1.1), as given below.

$$V_{12} = Z_{12}I_2 \qquad\qquad V_{21} = Z_{21}I_1 \tag{1.1}$$

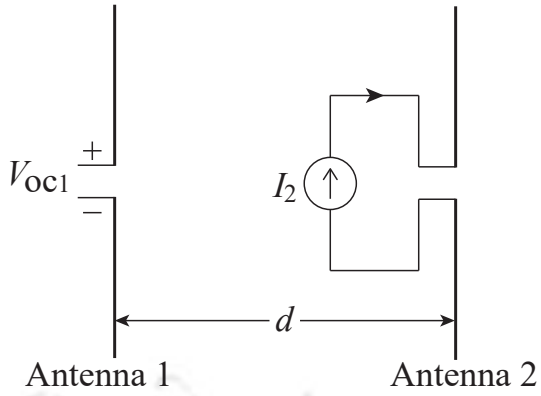

Fig. 1.4: The circuit diagram for defining the mutual impedance.

Using circuit diagrams shown in Figs. 1.3 and 1.4, mutual impedances (Z_{12} and Z_{21}) can be expressed as

$$Z_{12} = \text{the mutual impedance seen by Antenna 1 with Antenna 2 excited}$$

$$= \frac{V_{12}}{I_2} \tag{1.2}$$

$$= \frac{\text{the coupled voltage across Antenna 1's open circuit terminal}}{\text{the excitation current at Antenna 2's shorted terminal}}$$

$$= \frac{V_{\text{OC1}}}{I_2} \mid I_1 = 0, V_{\text{S1}} = 0 \tag{1.3}$$

Similarly, Z_{21} can be defined as

$$Z_{21} = \text{the mutual impedance seen by Antenna 2 with Antenna 1 excited}$$

$$= \frac{V_{21}}{I_1} \tag{1.4}$$

$$= \frac{\text{the coupled voltage across Antenna 2's open circuit terminal}}{\text{the excitation current at Antenna 1's shorted terminal}}$$

$$= \frac{V_{\text{OC2}}}{I_1} \mid I_2 = 0, V_{\text{S2}} = 0 \tag{1.5}$$

The effective voltage excitation vector due to the mutual coupling effect can be related to the uncoupled excitation vector as given below (refer to Appendix A.1):

$$[V_{total}] = [Z^t]^{-1}[Vs] \tag{1.6}$$

Here,

$$\begin{bmatrix} V_{S1} \\ V_{S1} \end{bmatrix} = V_S = \text{the uncoupled excitation voltage vector}$$

$$\begin{bmatrix} V_{total1} \\ V_{total2} \end{bmatrix} = V_{total} = \text{the coupled excitation voltage vector}$$

$$Z^t = \begin{bmatrix} 1 & \frac{Z_{12}}{Z_{22}} \\ \frac{Z_{21}}{Z_{11}} & 1 \end{bmatrix}$$

1.2.2 Mutual Coupling Mechanism in a Receiving MIMO Antenna

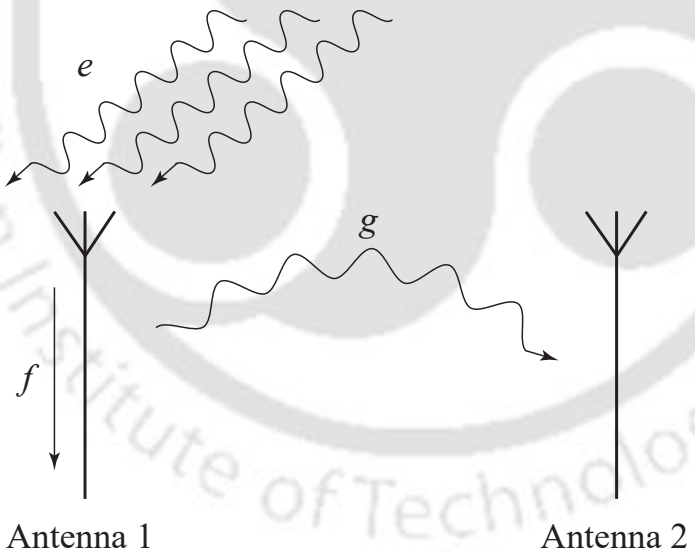

Fig. 1.5: A MIMO antenna system with two elements in the receiving mode.

Ideally, in receiving mode, all antenna elements are supposed only to receive the signal, but this is not the case in a practical scenario. As depicted in Fig. 1.5, the MIMO antenna receives the electromagnetic (EM) waves and convert them into an electrical signal. Assuming that the power of the incident EM waves on Antenna 1 is e. A significant part of this incident power gets converted to electrical power (labeled as f). However, a small part of the incident power

is scattered back by Antenna 1, labeled as g. Due to its proximity to Antenna 1, Antenna 2 partially collects this scattered power because of the mutual coupling. Similarly, Antenna 2 also re-scatters some portion of the received energy, which is subsequently received by Antenna 1. The same process is followed when EM waves are incident over Antenna 2. Now considering that both the antennas receive simultaneously, as shown in Fig. 1.6. In that case, the total signal received by the MIMO antenna will be the sum of the signal received by individual antennas and the sum of the signal received because of the mutual coupling effect between them [8, 9].

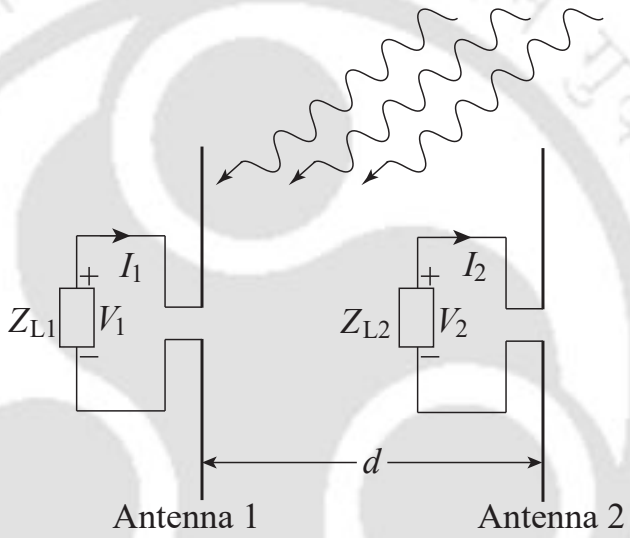

Fig. 1.6: A MIMO antenna system comprising two dipole antennas in the receiving mode.

It should be noted that the coupling paths between elements of an antenna array during the transmitting and receiving modes are different. In addition, the excitation of the transmitting and receiving antenna arrays are not the same, thus having different mechanisms that cause the mutual coupling. Therefore, the problem of mutual coupling for antenna arrays should be treated differently for the transmitting and receiving antenna modules [9].

An antenna system with two dipole antennas is considered in Fig 1.6 for analyzing and modeling the mutual coupling in receiving mode [10]. Note that Fig. 1.6 depicts the reception of the signal with both antennas, whereas Fig. 1.7 illustrates the signal reception in the standalone case for each antenna. The notations used in these figures are as follows:

Z_{L1}: is the termination load connected to Antenna 1.

Z_{L2}: is the termination load connected to Antenna 2.

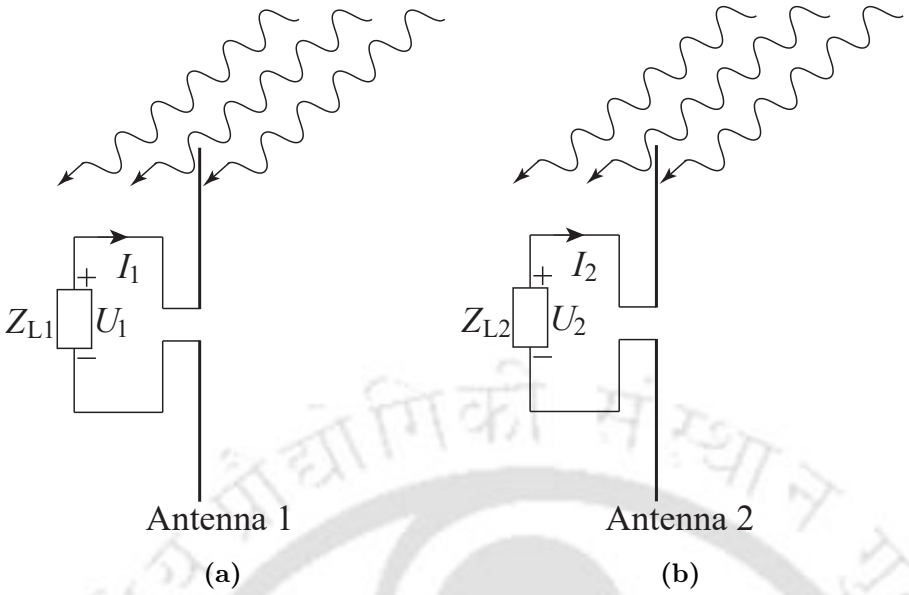

Fig. 1.7: Antennas receiving in the stand alone mode: (a) only Antenna 1, (b) only Antenna 2.

I_1: is the terminal current in Antenna 1.

I_2: is the terminal current in Antenna 2.

V_1: is the measured voltage at Antenna 1's terminal in the presence of dipole 2.

V_2: is the measured voltage at Antenna 2's terminal in the presence of dipole 1.

U_1: is the measured voltage at Antenna 1's terminal in the absence of dipole 2.

U_2: is the measured voltage at Antenna 2's terminal in the absence of dipole 2.

The received voltage vector considering the effect of mutual coupling for this two-element MIMO antenna system, can be related to the voltage received by the antennas in the stand-alone mode using (1.7) (refer to Appendix A.2).

$$[V] = [Z^r]^{-1}[U] \tag{1.7}$$

Here,

$$\begin{bmatrix} V_1 \\ V_2 \end{bmatrix} = V = \text{the coupled received voltage vector}$$

$$\begin{bmatrix} U_1 \\ U_2 \end{bmatrix} = U = \text{the uncoupled received voltage vector}$$

$$Z^r = \begin{bmatrix} 1 & \frac{Z_{12}}{Z_{L1}} \\ \frac{Z_{21}}{Z_{L1}} & 1 \end{bmatrix}$$

Mutual impedances Z_{21} and Z_{12} can be defined as given below [10].

$$Z_{21} = \frac{U_2 - V_2}{V_1} Z_{L1} \qquad Z_{12} = \frac{U_1 - V_1}{V_2} Z_{L2} \tag{1.8}$$

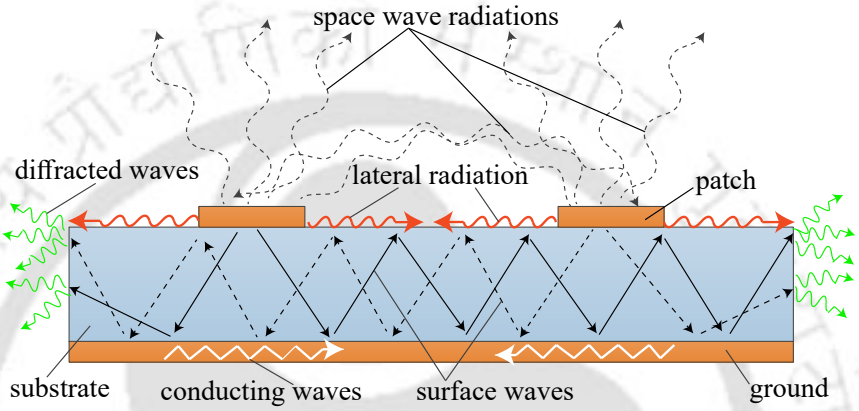

Fig. 1.8: EM coupling in printed MIMO antennas.

1.2.3 Causes of the Mutual Coupling in Printed and Dielectric Resonator-Based MIMO Antennas

The mechanism behind the mutual coupling in printed MIMO antenna is shown in Fig. 1.8. Ideally, while transmitting, all antenna elements should only transmit the signal in the form of space wave radiations. However, it does not happen practically because a part of the space wave radiation is received by the nearby antenna, as illustrated in Fig. 1.1 of subsection 1.2.1, leading to EM coupling. It is noticed that in addition to space wave radiations, microstrip antennas excite the surface wave mode. A surface wave is a guided mode that spreads out radially in the horizontal plane of the grounded substrate. Aside from unwanted surface wave excitation [11,12], microstrip antennas produce lateral radiations, i.e., the radiation propagating outward horizontally (laterally) from the antenna. The lateral radiation exists in the vicinity of the dielectric-air interface [13]. All the above-mentioned waves/radiations due to the excitation of one antenna interact with another antenna and lead to the unwanted mutual coupling between them. The surface wave and lateral radiation diffract from the edges around the discontinuity of

the ground plane and substrate, and this edge diffraction will often cause undesired radiations. Suppose, in a few antenna designs, if the substrate is discontinuous between antenna elements, then diffracted waves come into the picture at the discontinuity of substrate (similar to the diffracted waves at the edges) and contribute to the mutual coupling between antennas. For MIMO antennas, it is necessary to have a common reference/ground for all the antenna elements [14], and because of the common substrate backed with a common ground plane, conducting waves also increase the mutual coupling [15].

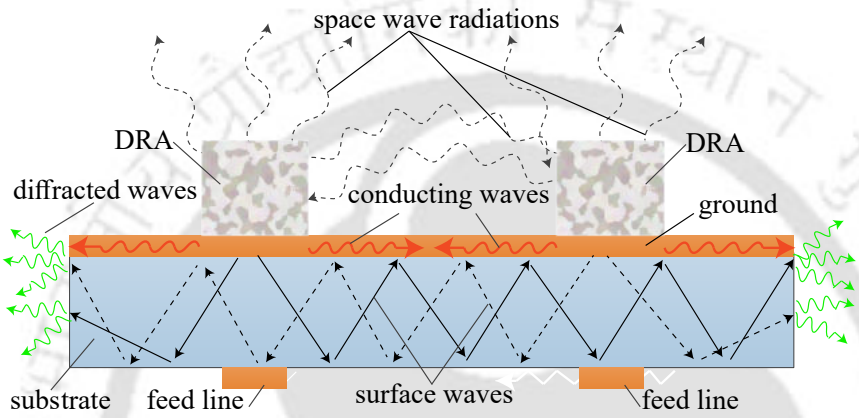

Fig. 1.9: EM coupling in dielectric resonator based MIMO antennas.

A schematic of two-element aperture-fed dielectric resonator antenna (DRA) with the mechanism behind the mutual coupling is shown in Fig. 1.9. The mutual coupling mechanism is noted to be very similar as described for the printed MIMO antennas.

Thus, the main causes of mutual coupling in a compact MIMO antenna can be summarized in the following points:

(i) Coupling due to space wave radiations or radiation pattern overlap

(ii) Signal leakage via surface current along the substrate

(iii) Coupling between feed lines through the common metallic ground

1.3 Effect of the Mutual Coupling on Antenna Characteristics

Some of the effects of the mutual coupling on antenna characteristics are given below:

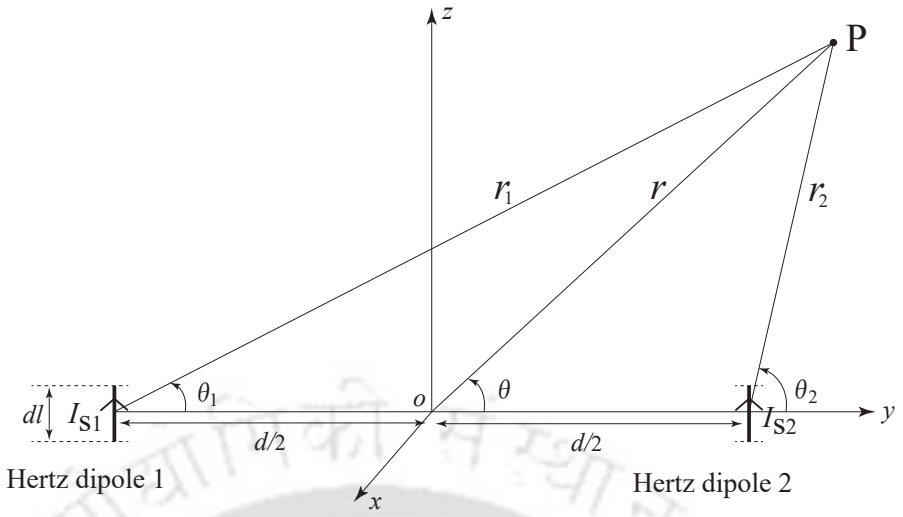

Fig. 1.10: A MIMO antenna system comprising two Hertz dipoles in the transmitting mode.

(i) **Changes the array radiation pattern:** The mutual coupling effect changes the net excitation current of the antenna element, which in turn changes its radiation pattern. Hence, the radiation pattern of a multiple antenna system would change as the individual antennas' radiation patterns change. To understand the same, an antenna system comprising two Hertz dipoles (shown in Fig. 1.10) is considered. A Hertz dipole is an infinitesimally small current element of length dl. Let I_{S1} and I_{S2} be the excitation current in the Hertz dipole 1 and Hertz dipole 2, respectively. The combined E-field radiation by both elements at a point P (in the far-field region), considering the mutual coupling, can be related to the combined E-field radiation without the mutual coupling [16]. Note that $\vec{E}_{\theta(total-mc)}$ denotes the total electric field vector considering mutual coupling, and $\vec{E}_{\theta(total)}$ denotes the total electric field vector with no mutual coupling (refer to Appendix A.3).

$$\vec{E}_{\theta(total-mc)} = \frac{\vec{E}_{\theta(total)}}{D} + Other\ terms \tag{1.9}$$

Here,

$$Other\ terms = -\frac{B}{D}\left[\left(Z'_{12}Is_2\right)\exp^{-j\frac{d}{2}cos\theta} + \left(Z'_{21}Is_1\right)\exp^{+j\frac{d}{2}cos\theta}\right]$$

where

$$B = \frac{j\exp^{-j\beta r}\sin\theta\beta^2}{4\pi\epsilon\omega r}$$

$$D = 1 - \frac{Z_{12}Z_{21}}{Z_{22}Z_{11}}$$

Similarly,

$$\vec{H}_{\phi(total-mc)} = \frac{\vec{H}_{\phi(total)}}{D} + Other\ terms \tag{1.10}$$

Here,

$$Other\ terms = -\frac{C}{D}\left[\left(Z'_{12}Is_2\right)\exp^{-j\frac{d}{2}cos\theta} + \left(Z'_{21}Is_1\right)\exp^{+j\frac{d}{2}cos\theta}\right]$$

$$C = \frac{j\exp^{-j\beta r}\sin\theta\beta}{4\pi r}$$

$$D = 1 - \frac{Z_{12}Z_{21}}{Z_{22}Z_{11}}$$

(ii) **Changes the received element voltage in a MIMO antenna:** When the antenna elements receive the incoming electromagnetic signals, the current gets induced first on the antenna elements and reradiates. The reradiated or re-scattered field distorts the incoming signals's wavefront, which other antenna elements would receive. Moreover, the received terminal voltages are the vectorial sum of the incoming signals and the reradiated or re-scattered field from the other antennas in proximity. Therefore, coupled voltage vector would be different from the uncoupled voltage vector at the receiving MIMO antenna, and they can be related by (1.7) in section 1.2.2, as given below.

$$\begin{bmatrix} U_1 \\ U_2 \end{bmatrix} = \begin{bmatrix} 1 & \frac{Z_{12}}{Z_{L1}} \\ \frac{Z_{21}}{Z_{L1}} & 1 \end{bmatrix} \begin{bmatrix} V_1 \\ V_2 \end{bmatrix} \tag{1.11}$$

(iii) **Changes the matching characteristics:** Ideally, all antennas should have radiation resistance only, but because of the mutual coupling effect, they also see mutual impedance in addition to the radiation resistance. This mutual impedance affects the matching characteristics of an antenna element. Thus, it affects efficiency, transmit or receive voltage vector, and radiation pattern.

1.4 Effect of Mutual Coupling on MIMO Performance

The adverse impact of the mutual coupling on the performance of MIMO-equipped communication systems can be quantified using the following parameters:

(i) **Antenna correlation coefficient (ACC):** The overlapping radiation patterns of closely placed antenna elements lead to a correlation that can be quantified as the antenna correlation coefficient (ACC). The ACC for a pair of antennas can be calculated using (1.12), and its value is complex.

$$ACC_{ij} = \frac{\iint_{4\pi} (A_1 + A_2)\, p_\theta(\theta,\phi)\, p_\phi(\theta,\phi)\, d\Omega}{\sqrt{\left(\iint_{4\pi} A_3 p_\theta(\theta,\phi)\, p_\phi(\theta,\phi)\, d\Omega\right)\left(\iint_{4\pi} A_4 p_\theta(\theta,\phi)\, p_\phi(\theta,\phi)\, d\Omega\right)}} \tag{1.12}$$

where

$$A_1 = XPR \cdot \vec{E}_{\theta,i}(\theta,\phi) \cdot \vec{E}^*_{\theta,j}(\theta,\phi)$$

$$A_2 = \vec{E}_{\phi,i}(\theta,\phi) \cdot \vec{E}^*_{\phi,j}(\theta,\phi)$$

$$A_3 = XPR \cdot \left|\vec{E}_{\theta,i}(\theta,\phi)\right|^2 + \left|\vec{E}_{\phi,i}(\theta,\phi)\right|^2$$

$$A_4 = XPR \cdot \left|\vec{E}_{\theta,j}(\theta,\phi)\right|^2 + \left|\vec{E}_{\phi,j}(\theta,\phi)\right|^2$$

$$d\Omega = \sin(\theta) d\theta d\phi$$

Here, $\vec{E}_{\theta,i}(\theta,\phi)$ is the theta component and $\vec{E}_{\phi,i}(\theta,\phi)$ is the phi component of the E-field radiation pattern at (θ,ϕ) point in the far-field region when the i^{th} port of a MIMO antenna is excited. In (1.12), $p_\theta(\theta,\phi)$ and $p_\phi(\theta,\phi)$ are the probability distribution function of the angle of arrivals of the incoming signal in θ and ϕ directions, respectively. The XPR factor used in (1.12) corresponds to the cross-polarization discrimination, which is the ratio of the incoming waves's vertically and horizontally polarized E-field components. It is to be noted that $ACC_{i,i}$ is the self correlation of the i^{th} antenna with itself and hence, its magnitude always equals unity.

Usually, the square of the magnitude of ACC is known as the envelope correlation coefficient (ECC), which can be calculated using (1.13) [17, 18].

$$ECC_{ij} = |ACC_{ij}|^2 \tag{1.13}$$

(ii) **Diversity order (DO) and diversity measure (DM):** The diversity gain (DG), as referred to in [19–21], is calculated using (1.14) as a measure of diversity performance for

two-port MIMO antennas.

$$\mathrm{DG} = 10\sqrt{1 - |ECC_{ij}|^2} \tag{1.14}$$

The DG calculation using (1.14) can not give a holistic way of providing proper diversity performance of MIMO antennas with more than two ports. For $M\times N$ MIMO systems with M transmit antennas and N receive antennas, $\binom{M}{2}$ and $\binom{N}{2}$ combinations of DG calculations for these many pairs of antenna elements are required. It becomes cumbersome to compare the diversity performance of MIMO antennas having more than two elements. Diversity order (DO) and diversity measure (DM) of the MIMO antenna can be calculated from the MIMO ACC matrix. Both the parameters give a holistic measure of diversity performance by providing a single value of the DO and the DM for any number of antenna elements. The DO for a MIMO antenna with N elements can be calculated from the rank of its ACC matrix using (1.15), written below.

$$\mathrm{DO} = rank(\boldsymbol{ACC}) \tag{1.15}$$

where

$$\boldsymbol{ACC} = \begin{bmatrix} ACC_{11} & \dots & ACC_{1N} \\ \vdots & \ddots & \vdots \\ ACC_{N1} & \dots & ACC_{NN} \end{bmatrix}$$

The ACC matrix for the transmitter side ($\boldsymbol{ACC_{Tx}}$) and receiver side ($\boldsymbol{ACC_{Rx}}$) can be given by (1.16) and (1.17), respectively, for a MIMO system with M transmit antennas and N receive antennas.

$$\boldsymbol{ACC_{Tx}} = \begin{bmatrix} ACC_{11}^{Tx} & \dots & ACC_{1M}^{Tx} \\ \vdots & \ddots & \vdots \\ ACC_{M1}^{Tx} & \dots & ACC_{MM}^{Tx} \end{bmatrix} \tag{1.16}$$

$$\boldsymbol{ACC_{Rx}} = \begin{bmatrix} ACC_{11}^{Rx} & \dots & ACC_{1N}^{Rx} \\ \vdots & \ddots & \vdots \\ ACC_{N1}^{Rx} & \dots & ACC_{NN}^{Tx} \end{bmatrix} \tag{1.17}$$

Considering i.i.d. Rayleigh faded channel model, the DO for such a MIMO system is

bounded by the product of the rank of the ACC matrix of the MIMO antenna at the transmitter and the rank of the ACC matrix of a MIMO antenna at the receiver side.

$$\mathrm{DO} \leq DO_{Tx} \times DO_{Rx} = rank(\boldsymbol{ACC_{Tx}}) \times rank(\boldsymbol{ACC_{Rx}}) \tag{1.18}$$

The DM for a MIMO antenna can be calculated from the trace and the Frobenius norm of its ACC matrix [22]. For a MIMO system employing correlated MIMO antennas at the transmitter and receiver end, the DM can be found using (1.19).

$$\mathrm{DM} = DM_{Tx} \times DM_{Rx} \tag{1.19}$$

In (1.19), DM_{Tx} and DM_{Rx} represent the DM values on the transmitter and receiver sides, respectively, and can be calculated using (1.20).

$$DM_{Tx} = \left(\frac{\mathrm{tr}(\boldsymbol{ACC_{Tx}})}{\|\boldsymbol{ACC_{Tx}}\|_F}\right)^2, \quad DM_{Rx} = \left(\frac{\mathrm{tr}(\boldsymbol{ACC_{Rx}})}{\|\boldsymbol{ACC_{Rx}}\|_F}\right)^2 \tag{1.20}$$

Here, $\mathrm{tr}(\square)$ and $\|\square\|_F$ denote the trace and the Frobenius norm of the matrix. The DM properly considers the antenna correlation in DG performance of the MIMO antenna and it is bounded by the DO. It is also noted that there is a significant reduction in the diversity performance of a MIMO antenna. This loss can be measured in terms of percentage diversity gain reduction (PDGR) and can be calculated using (1.21).

$$\mathrm{PDGR} = \frac{\mathrm{DO} - \mathrm{DM}}{\mathrm{DO}} \times 100\% \tag{1.21}$$

(iii) **Channel capacity loss:** The channel capacity loss (CCL) is considered a significant parameter in the channel performance analysis of MIMO antennas. In the ideal case, the CCL should be equal to zero. However, in practical cases, the CCL is not zero due to the correlation between antenna elements. The value of CCL due to receiver side correlation (CCL_{Rx}) can be calculated using (1.22) [23].

$$CCL_{Rx} = -\log_2(\det(\boldsymbol{ACC_{Rx}})) \tag{1.22}$$

Here, $\det(\square)$ denotes the determinant of a matrix. Similarly, the CCL due to the corre-

lation between antennas on the transmitter side (CCL_{Tx}) can be calculated using (1.23).

$$CCL_{Tx} = -\log_2(\det(\boldsymbol{ACC_{Tx}})) \tag{1.23}$$

The total channel capacity loss considering the correlation between antennas on both the transmitter and receiver sides (CCL) can be calculated using (1.24).

$$\text{CCL} = CCL_{Rx} + CCL_{Tx} = -\log_2(\det(\boldsymbol{ACC_{Rx}})) - \log_2(\det(\boldsymbol{ACC_{Tx}})) \tag{1.24}$$

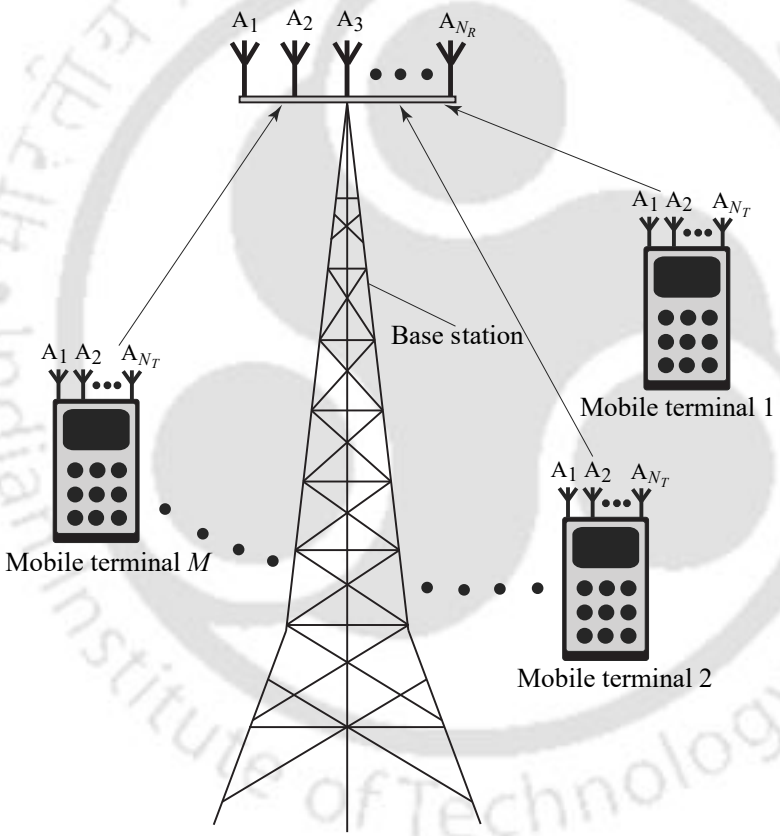

Fig. 1.11: Multi-user MIMO uplink system of M mobile terminals, each fitted with N_T antennas and the base station with N_R antennas.

(iv) **Sum rate loss:** In Fig. 1.11, a multi-user MIMO uplink system is depicted. Here, a base station (BS) with N_R antennas serves M mobile terminals that are geographically separated. Each mobile terminal in this setup is equipped with N_T transmit antennas such that $N_R \geq M \times N_T$. With an assumption that the BS's antenna elements are placed

sufficiently apart, the antenna correlation between them can be neglected. Since each mobile terminal is much smaller than the BS, its N_T antennas are closely packed. Further, assuming that mobile terminals have employed identical antenna elements, they would have the same correlation matrix. Considering the BS's MIMO antenna as the receive antenna and all mobile terminals' MIMO antennas collectively as a transmit antenna, the overall transmit antenna correlation matrix for all mobile terminals is denoted by $\boldsymbol{ACC_T}$. For this uplink scenario, the overall channel capacity loss due to correlation is expressed using sum-rate loss (SRL). The SRL due to the correlations of the antennas employed at the mobile terminals can be expressed as (1.25) [24].

$$\text{SRL} = -MN_T \log_2 \left(\frac{MN_T}{\text{tr}(\boldsymbol{ACC_T^{-1}})} \right) - \sum_{m=1}^{MN_T} \log_2(\boldsymbol{ACC_T^{-1}})_{mm} \tag{1.25}$$

Here, tr(□) denotes the trace of a matrix and $(\square)_{mm}$ denotes m^{th} diagonal element of a matrix. In order to get the best performance from a MIMO antenna in a multi-user MIMO scenario, its SRL should be zero. A high value of SRL would mean more loss in the sum rate, which is undesirable. Therefore, the mobile terminal's antennas should be designed appropriately to attain the minimum SRL.

1.5 Mutual Coupling Reduction

The mutual coupling between the elements of a MIMO antenna is highly undesirable as it degrades the performance of a MIMO communication system. Hence, the following techniques can be used to mitigate the effects of mutual coupling:

(a) **Increasing the distance between antenna elements:** The simplest way to reduce the mutual coupling is to increase the distance between antenna elements [8]. But, due to the trend of miniaturization of radio transceivers, the distance between antenna elements is being reduced day-by-day. Therefore, increasing the distance between antenna elements is not a viable option.

(b) **Decoupling the effect of the mutual coupling:** In literature, many decoupling methods have been proposed to assuage the effect of mutual coupling in antenna arrays. In this regard, a mutual coupling compensating approach has been used to

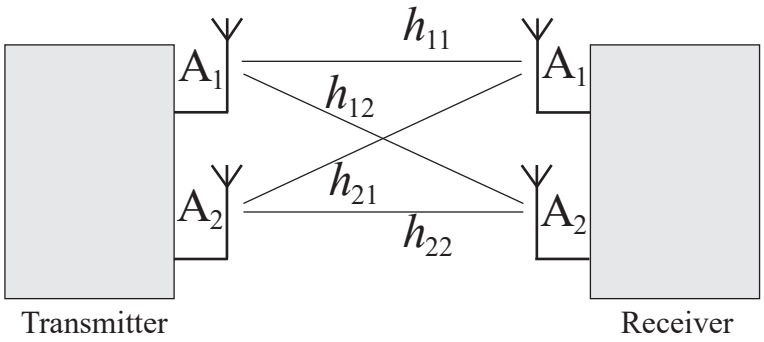

Fig. 1.12: A 2×2 MIMO communication channel model.

estimate the direction of arrival [25]. The mutual coupling effect can be compensated by considering the modified channel matrix. To illustrate the same, let us consider a 2×2 MIMO system, as shown in Fig. 1.12 where channel matrix H can be expressed by (1.26).

$$H = \begin{bmatrix} h_{11} & h_{12} \\ h_{21} & h_{22} \end{bmatrix} \tag{1.26}$$

For compensating the mutual coupling effect, a modified channel matrix ($H_{mutual-coupling}$) should be considered in place of the channel matrix (H), as given below (refer to Appendix A.4).

$$H_{mutual-coupling} = [Z^r][H][Z^t]^{-1} \tag{1.27}$$

Here, $[Z^t]$ and $[Z^r]$ are the same as given in (1.6) and (1.7), respectively.

In this way, the effect of mutual coupling can be compensated by using the circuit theoretic approach.

(c) **Other techniques:** In literature, several techniques have been suggested to reduce the mutual coupling between antenna elements and improve their isolation. Some of these proposed methods utilize the defected ground structure (DGS), electromagnetic bandgap structures (EBG), parallel-coupled line resonators, metamaterial, polarization converters, and neutralization lines [7]. In the next chapter, a detailed discussion has been carried out on the state-of-the-art mutual coupling reduction techniques.

2

Mutual Coupling Reduction Techniques

The motivation for designing low mutual coupling MIMO antennas for modern wireless communication systems is discussed in-depth in the first chapter. This chapter describes various state-of-the-art techniques for reducing the mutual coupling between antenna elements, such as electromagnetic band-gap (EBG) structures, defected ground structures (DGS), neutralization line technique, decoupling surfaces, orthogonal modes, and other techniques-based MIMO dielectric resonator antennas, and SIW-based fraction mode strategy.

2.1 Introduction

In this section, various state-of-the-art techniques for MC reduction among antenna elements have been discussed, along with their salient features. The following points enlist some of the prominent ones:

(i) Electromagnetic band-gap structures and isolators

(ii) Defected ground structures

(iii) Neutralization line technique

(iv) Decoupling surfaces

(v) Orthogonal mode-based MIMO dielectric resonator antennas

(vi) Other dielectric resonator-based MIMO antennas

(vii) Substrate integrated waveguide cavity-based MIMO antennas, etc.

2.2 MIMO Antenna with Electromagnetic Band-Gap Structures

The electromagnetic band gap (EBG) structures are artificial periodic (or sometimes non-periodic) structures created by arranging metallic conductors and dielectric materials in periodic patterns. The EBG can prevent or assist electromagnetic waves from propagating in a specified frequency band for all incident angles and polarization states. They exhibit a frequency band gap for the incident surface wave ($k_x^2 + k_y^2 \leq k_0^2$, k_z is purely imaginary) [26]. This feature enables the EBG structures to facilitate MC reduction between antenna elements. Therefore, various EBG structures [27–30] and isolators [31–33] have been developed to reduce the MC in planar antennas. An EBG structure composed of mushroom-like unit cells spread over 13.5 mm $\times$ 48.5 mm lateral space has been used for MC reduction in [27]. An EBG surface composed of short-circuited microstrips through inter-locked branch stubs is used in [28] for MC reduction, as shown in Fig. 2.1(a). It occupies two times more area than the surface area of a single radiating patch. A uniplanar compact EBG structure of dimensions 13.2 mm $\times$ 72.6 mm is

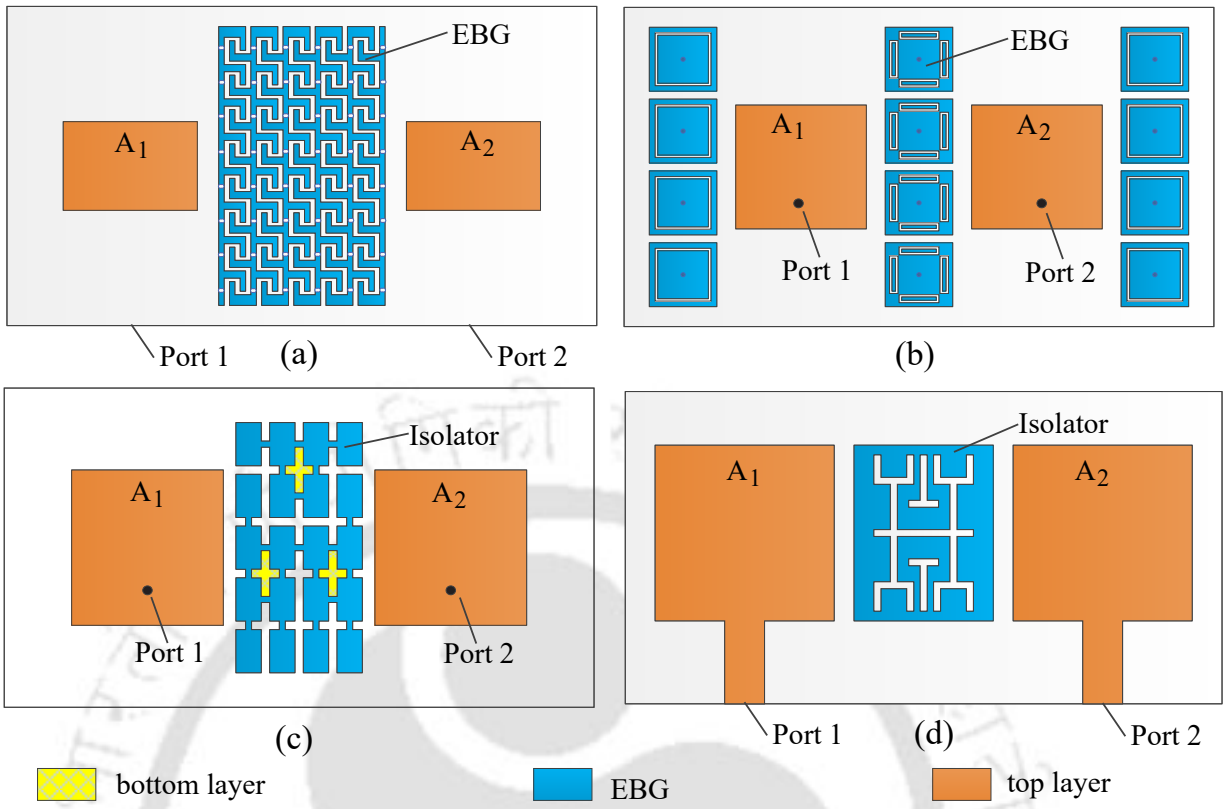

Fig. 2.1: MIMO antennas with EBG and isolators: (a) aperture coupled microstrip patch antenna with EBG (from [28]), (b) coaxial fed microstrip patch antenna (from [30]), (c) coaxial fed microstrip patch antenna with polarization converter-based isolator (from [31]), and (d) microstrip line fed patch antenna with EBG-based isolator (from [32]).

placed in the next immediate layer for MC reduction [29]. However, this increases the vertical profile of the antenna by 1.27 mm. In [30], Liu et *al.* used EBG unit cells, which occupy 33.3% of the total antenna area, as shown in Fig. 2.1(b). A polarization converter-based isolator has been used in [31], as illustrated in Fig. 2.1(c), which occupies 17% more area than the surface area of a single patch. An EBG-based fractal isolator is used for MC reduction in [32] (refer to Fig. 2.1(d)), which takes a size of 16 mm $\times$ 23 mm, while the single radiating patch occupies a space of 23 mm $\times$ 23 mm. In [33], Alibakhshikenari et *al.* used an EBG structure of dimensions 15.1 mm $\times$ 50 mm with metallic walls for MC reduction. As reported in [34], a double-layer crossed mushroom wall structure (operating in the EBG region) has been used to mitigate the MC between four SIW cavity-backed antennas. Some of the above MIMO antennas have been depicted in Fig. 2.1. A general observation indicates that EBGs and isolators can reduce the mutual coupling but always at the expense of large spacing between the antenna elements.

2.3 MIMO Antenna with Defected Ground Structures

The defected ground structure (DGS), as the name implies, refers to some peculiar geometries, commonly known as a "unit cell" etched out as a single defect or in periodic configuration, usually with a small period number on the ground plane of a microwave printed circuit board (MPCB). It has the attribute of stopping wave propagation through the substrate over a frequency range. Therefore, the DGS can be described as a unit cell EBG or an EBG with a limited number of cells. The DGS slots are generally resonant in nature. The presence of a DGS under a printed transmission line perturbs the current distribution in the ground plane and thus modifies the equivalent line parameters over the defected region. Thus it influences the guided wave characteristics and exhibits (1) bandgap properties and (2) a slow wave effect, which helps in the size reduction of the printed circuits. As mentioned earlier, the study of DGS can be classified into two categories depending on their configurations: (1) single unit cell DGS; and (2) uniform or non-uniform periodic arrangement of unit cells [35].

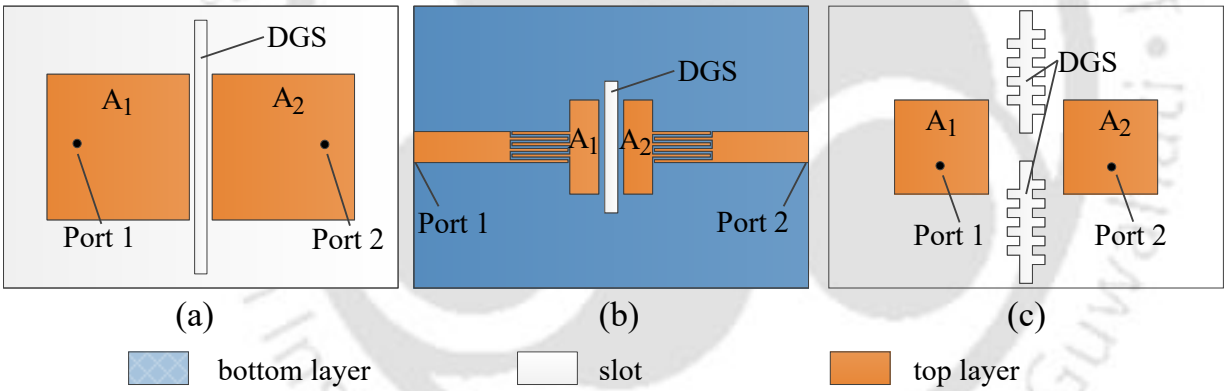

Fig. 2.2: MIMO antennas with DGS: (a) two-port microstrip patch antenna with coaxial feed (from [36]), (b) two-port metamaterial-based patch antenna with microstrip feed line (from [37]), and (c) two-port microstrip patch antenna with coaxial feed (from [38]).

Various antenna configurations, which use DGS for MC reduction, are shown in Fig. 2.2 [36–38]. A rectangular slot (of a length comparable to the guided wavelength) is etched in the ground plane to decouple the microstrip antennas [36] and meta-material antennas [37], as shown in Figs. 2.2(a) and 2.2(b), respectively. Two modified rectangular slots (of a length comparable to half of the guided wavelength) are used to enhance the isolation between rectangular microstrip antennas in [38], as depicted in Fig. 2.2(c).

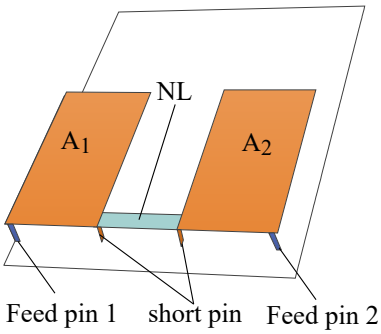

Fig. 2.3: Suspended NL between two PIFAs (from [39]).

2.4 MIMO Antenna with Neutralization Lines

In the neutralization line (NL) isolation enhancement technique, a microstrip line links the current from one antenna to another. The current fed from one antenna interferes out-of-phase with the coupled current in another antenna (because of mutual coupling). The out-of-phase neutralization of the coupled current's effect happens for an appropriate length of the microstrip feed line connecting two antennas. This microstrip line is known as the neutralization line. In this manner, the NL cancels the coupled current's effect in the nearby antenna and helps to achieve low mutual coupling between two closely placed antennas.

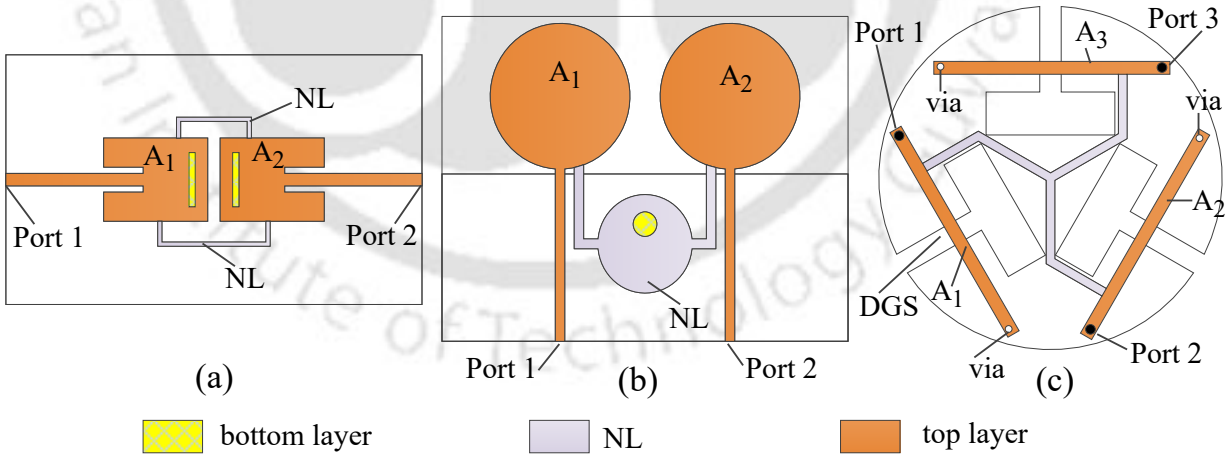

Fig. 2.4: NL based MIMO antennas: (a) two-port microstrip antenna with microstrip feed (from [44]), (b) two-element circular printed monopole antenna (from [45]), and (c) three-port slot antenna with coaxial feed (from [46]).

In [39], the authors present a two-port planar inverted F-antenna (PIFA) where one antenna operates in the digital cellular system (DCS) frequency band while the other antenna functions

in the universal mobile telecommunication (UMTS) band. The isolation between these two antennas is enhanced by using a suspended NL that joins both antennas, as shown in Fig. 2.3. Antenna researchers have widely used the NL technique to decouple the antennas operating within the same frequency bands for MIMO applications [40–46]. The NL with a grounded branch has been used to reduce the mutual coupling between two F-shaped monopoles in [40]. In a similar approach, three NLs are used for isolation enhancement in the MIMO antenna for a mobile terminal [41]. In [42], Cihangir et *al.* achieved low mutual coupling in a two-port MIMO antenna using NLs. In all of these approaches ([40–42]), the NLs were employed in the ground plane layer. The authors in [43] proposed a decoupled dual-antenna system for LTE/WWAN smartphone applications. Under the approach, the NL structure was constructed through four vias, which resulted in a complex antenna structure. In [44], Yu et *al.* used two NLs to decouple two microstrip patch antennas, as shown in Fig. 2.4(a). A wideband neutralization line was used to decouple two ultra-wideband (UWB) monopole antennas [45], as depicted in Fig. 2.4(b). Likewise, in another work [46], Zhang et *al.* connected NLs between feed lines and shorted vias at the other end of the feed lines to reduce the MC between three slot antennas (refer to Fig. 2.4(c)).

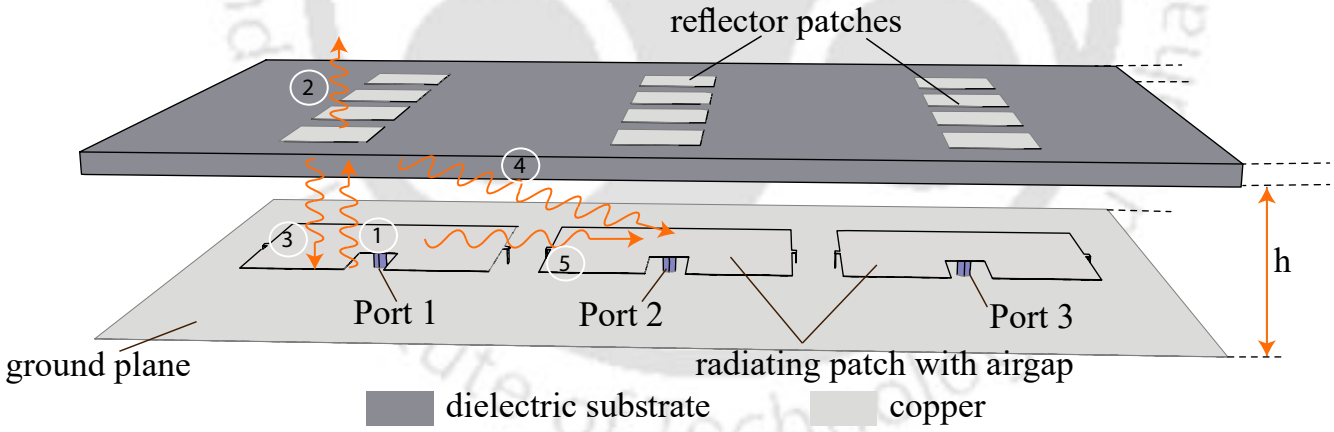

Fig. 2.5: Working principle of array decoupling surfaces [47].

2.5 MIMO Antenna with Decoupling Surfaces

The primary objective of placing an array decoupling surface (ADS) above the MIMO antenna is to reduce the mutual coupling between two adjacent antenna elements. The ADSs or superstrates enable the partially reflected signal to interact out-of-phase with the coupled

signal and mitigate the latter's effect. Intuitively, the height of the ADS above the antenna and the size of the metal reflection patches determine the phase and the intensity of the partially reflected wave, respectively [47]. It is thus necessary to put ADSs or superstrates above the antenna array, which increases the height of the antenna. As depicted in Fig. 2.5, it can be perceived that the energy radiated by one antenna element (1) of a MIMO antenna with a decoupling surface propagates further in four forms: the wave being radiated outward into free space (2); the reflected wave received by the transmitting antenna (3); the reflected wave from the primary reflector patches (4) and the coupled wave linked with adjacent antenna element (5). Out-of-phase interaction of the partially reflected wave (4) with the coupled wave (5) results in low mutual coupling.

The authors in [48] used a metasurface-based decoupling method (MDM) that employed a superstrate at a level of 11 mm above the MIMO antenna. A ceramic superstrate is placed at a height of 7 mm above the antenna elements in [49]. Two layers of metasurface superstrate are used above the patch antennas for MC reduction [50]. By doing so, the height of the antenna gets increased by 5.5 mm. The capacitively loaded loop-based MTM superstrate and metasurface (MS)-based decoupling techniques were used to enhance the isolation in [51] and [52], respectively. These techniques increase the overall size of the MIMO antennas.

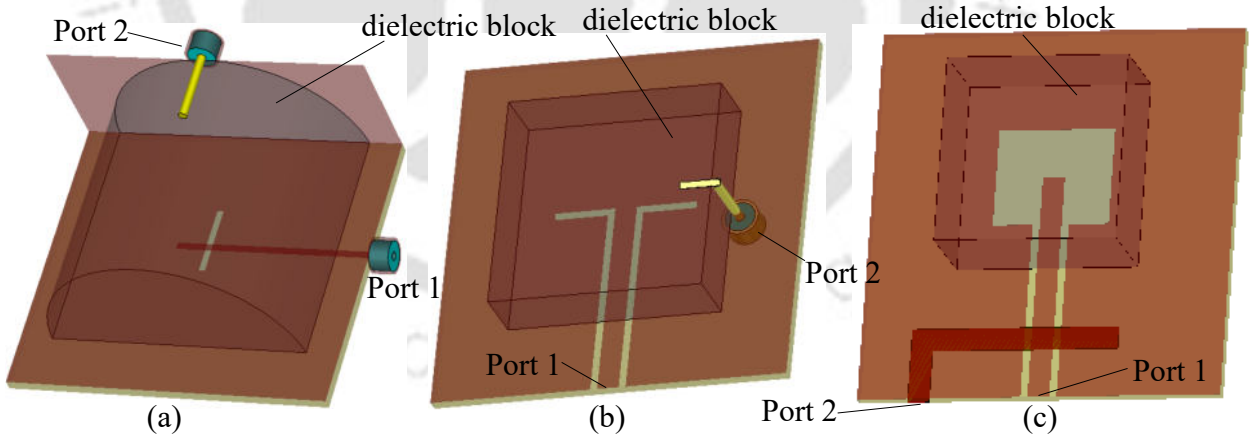

Fig. 2.6: Orthogonal mode-based 2-port MIMO DRA: (a) a semi cylindrical DRA with aperture coupled and coaxial probe feed (from [54]), (b) CPW-based aperture coupled and coaxial probe fed rectangular DRA (from [55]), and (c) CPW-based aperture and aperture coupled rectangular DRA (from [56]).

2.6 Orthogonal Mode-Based MIMO Dielectric Resonator Antennas

Dielectric resonator antennas (DRAs) have emerged as a new and viable alternative to printed antennas in MIMO applications because of its attractive features [53]. Excitation of orthogonal modes using multiple ports in a dielectric resonator antenna (DRA) provides low inter-port coupling. Therefore, several hybrid feeding techniques were used to exploit the same in MIMO DRAs [54–57]. In [54], two orthogonal modes are excited in a semi-cylindrical DRA by using aperture-coupled feed and probe feed, respectively, as shown in Fig. 2.6(a). Two orthogonal modes are excited in a cuboid-shaped DRA by using CPW-based aperture feed and probe feed, respectively, in [55] and depicted in Fig. 2.6(b). Authors in [56] have used CPW-based aperture-coupled and aperture-coupled feed for exciting two orthogonal modes in a cuboid-shaped DRA (refer to Fig. 2.6(c)). Two orthogonal modes are excited for low mutual coupling in an annular ring-shaped DRA in [57].

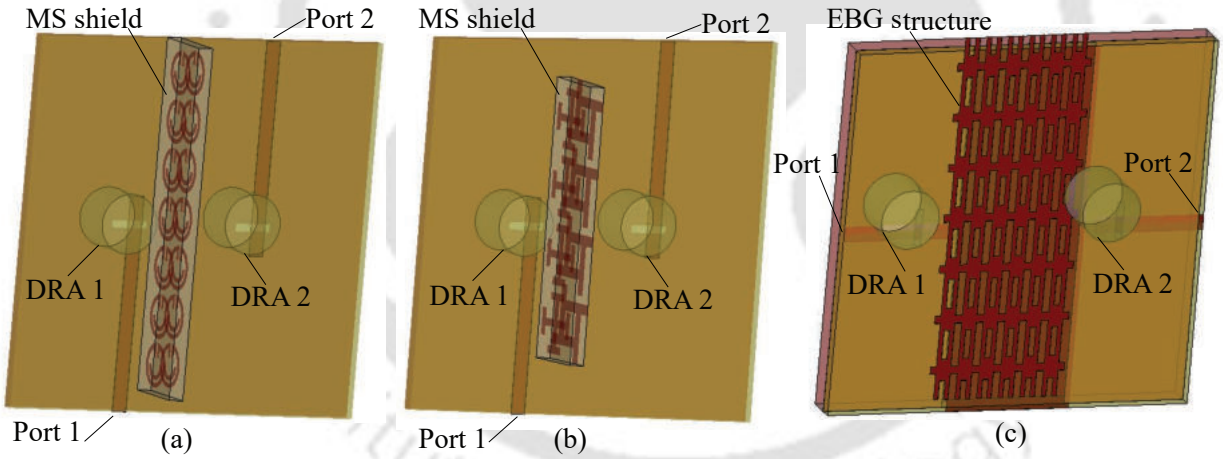

Fig. 2.7: Two-port MIMO DRAs: (a) two elements CDRAs with a metasurface wall (from [58]), (b) two elements CDRAs with a FSS wall (from [59]), and (c) two element MIMO CDRA with EBG-based decoupler (from [60]).

2.7 Other Dielectric Resonator-Based MIMO Antennas

Isolating walls made up of metasurface and frequency selective surface (FSS) were used to decouple two cylindrical DRAs (CDRAs) in [58] and [59], as shown in figures viz. Figs. 2.7(a) and 2.7(b), respectively. These shielding structures are taller than the dielectric blocks and

thus increase the antenna's size. The surface-wave propagation was suppressed to decouple two cylindrical DRAs by employing an EBG structure that occupies a larger space, thus increasing the inter-element spacing in [60], as shown in Fig. 2.7(c). In a wireless access point, the EM isolation between the DRAs is enhanced by placing a metallic cylinder [61]. However, the antenna profile increases due to the excess height of the cylinder. Reduction in mutual coupling was demonstrated by employing an engineered partially reflecting surface [62] or a dielectric sheet [63] as a superstrate, as described in section 2.5. However, this increases the antenna height due to the placement of a superstrate. In [64], 4-quarters of a DRA are arranged for MIMO application with circular polarization. A ring-shaped DGS is demonstrated to suppress the MC between two cylindrical DRAs (CDRAs) in [65]. In [66], mushroom-shaped DRAs are arranged orthogonally to reduce the MC between them. Triple-port, two-element CDRA with orthogonal modes for MIMO applications is presented in [67]. Two-port low MC antenna array comprising two A-shaped DRAs are excited by means of the conformal strip for wideband applications in [68]. Three decoupled modes in a single rectangular DRA are excited using three separate ports to achieve low inter-port coupling in [69]. The EM field coupling between two rectangular DRAs (RDRAs) was suppressed by using printed metal strips on the DRA surface in [70] and inserting metallic vias through the RDRAs in [71]. The literature review suggests that the mutual coupling can be suppressed by mitigating the coupling paths between antennas through surface waves and free-space radiations. Achieving low mutual coupling is particularly challenging, especially when the inter-element spacing is $0.1\lambda_0$ or less while the antenna size is simultaneously reduced [71].

2.8 Substrate Integrated Waveguide-Based MIMO Antenna Designs

Few substrate-integrated waveguide (SIW)-based multi-port antennas (2-port, 4-port) for MIMO application are presented in [34], [72–77]. In [34] and [72], four full-mode SIW cavity-backed slot antennas are employed to realize a 4-port MIMO antenna design. Kumar et *al.* have proposed a similar 4-port MIMO antenna comprising four full-mode rectangular cavity-based antennas [73]. In [74], Sung et *al.* present a 4-port triangular-shaped SIW MIMO antenna. Quarter-mode (QM) sub-cavities-based 4-port MIMO antenna is reported in [75]. In [76], Nandi

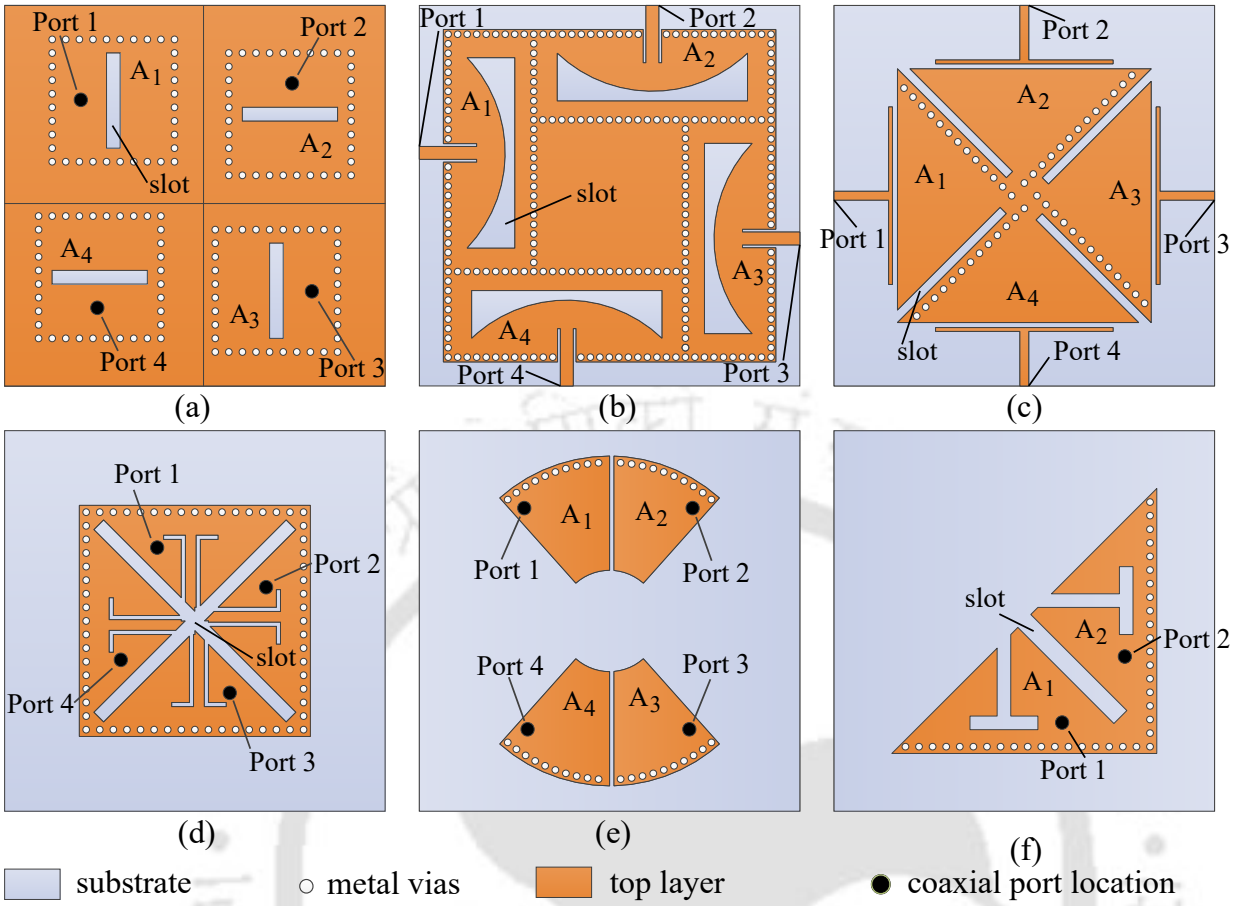

Fig. 2.8: SIW based MIMO antenna designs: (a) coaxial fed full-mode cavity-based 4-port antenna (from [34] and [72]), (b) microstrip fed full-mode cavity-based 4-port antenna (from [73]), (c) gap coupled triangular SIW cavity based 4-port antenna (from [74]), (d) coaxial fed quarter-mode cavity-based 4-port antenna (from [75]), (e) coaxial fed eighth-mode cavity-based 4-port antenna (from [76]), and (f) coaxial fed SIW cavity-based 2-port antenna (from [77]).

et *al.* present TM^{z}_{101} mode-based eighth-mode (EM) 2-port and 4-port MIMO antennas. A 2-port eighth mode SIW cavity-based MIMO antenna is presented in [77]. To the best of the author's knowledge, most of the SIW cavity-based MIMO antennas reported so far have only two or 4-ports because of various limitations in the half mode (HM), QM, and EM designs.

3

Neutralization Line Based Low Mutual Coupling MIMO Antenna

The neutralization line (NL) offers an easy and effective option for MC reduction among various MC reduction techniques outlined in the previous chapter. This chapter presents two NL-based MIMO antennas. The first part of the chapter reports a 2-port dual-band printed MIMO antenna, while the second part presents a 6-port printed MIMO antenna.

3.1 Introduction

Among the different MC reduction techniques illustrated in chapter 2, the NL offers an easy way in comparison to EBGs, ADSs, and superstrates. In literature, some of the articles utilizing the NL technique are discussed in [39–46]. From this literature survey, it can be inferred that the NL technique has not been used much for multiple-band MIMO antenna designs. Hence, the first part of this chapter presents a dual-port dual-band MIMO antenna. Since NLs have been used so far only in 2-port and 3-port MIMO antenna configurations, the second part of the chapter reports a 6-port MIMO antenna.

3.2 Low Mutual Coupling Dual-port Dual-band MIMO Antenna for Mobile Terminal

3.2.1 Introduction

With the advancement in communication technology, mobile terminal with multi-standard compatibility is the need of the hour. Therefore, designing a low-mutual coupling multi-band MIMO antenna with a small footprint is a popular research topic among antenna engineers. In this part of the chapter, a dual-port dual-band MIMO antenna is presented, it comprises two printed circular monopole antennas. The -10 dB impedance bandwidth of the antenna is noted from 2.3 to 2.8 GHz and 3.37 to 3.72 GHz. The isolation between antenna elements is enhanced in both frequency bands by connecting them through a microstrip NL and extending a stub in the ground plane. The mutual coupling is found to be below -15 dB with an inter-element spacing of 0.092 times the free-space wavelength at 2.3 GHz. The maximum gain of this antenna is noted to be 3.66 dBi with an ECC $\leq$ 0.0465 in the entire operating bandwidth.

3.2.2 Antenna Geometry

A geometric layout of the two-element MIMO antenna is shown in Fig. 3.1. This antenna design uses RT-Duroid 5870 substrate with a dielectric constant of 2.33 and thickness of 1.57 mm. The top layer consists of two circular-shaped monopole patches with split ring-shaped slots. A separate microstrip line feeds each antenna element. The antenna elements are connected using a neutralization line AB with an additional rectangular loop PQRS in the top

layer. A stub LM is extended in the ground plane between the radiators and is referred to as the grounded stub (GS). The values of various design parameters and dimensions are as follows: $L_s = 80$, $W_s = 45$, $L_f = 17$, $W_f = 3.8$, $L_{LM} = 11$, $W = 2.5$, $R_1 = 6.5$, $R_2 = 12$, $G = 1.2$, $S_1 = 1$, $L_{PS} = L_{QR} = 6$, $L_{PQ} = L_{SR} = 10$. All dimensions are in mm.

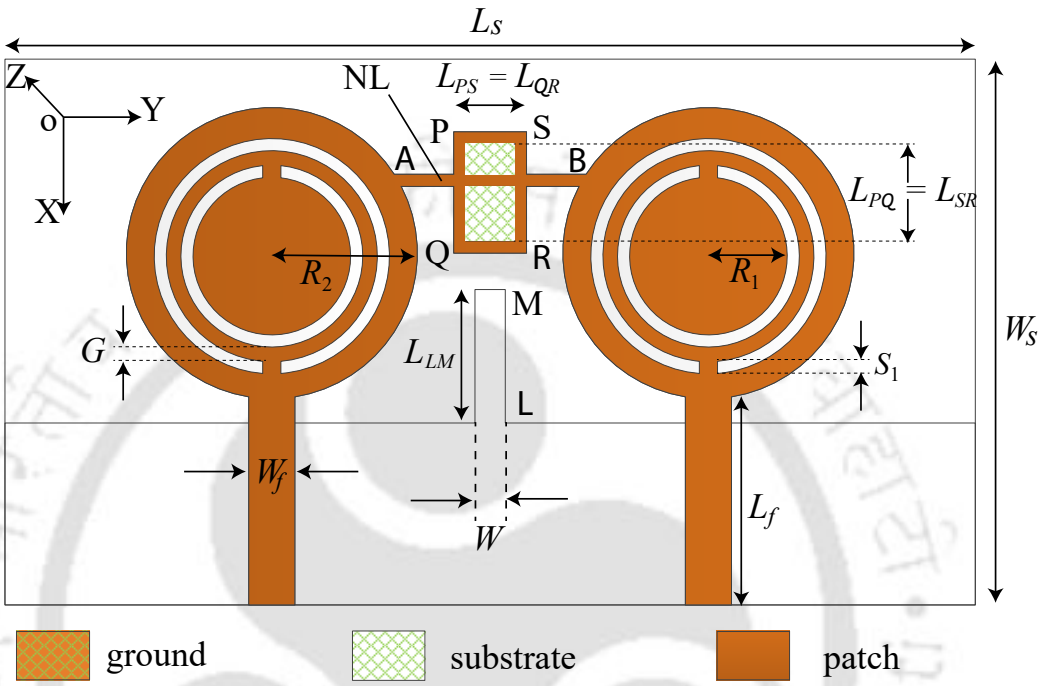

Fig. 3.1: Antenna geometry and design.

3.2.3 Working Mechanism

The two-element MIMO antenna, depicted in Fig. 3.1, uses circular patches loaded with split-ring-shaped slots as radiating elements. The design evolution is explained through various stages, as shown in Fig. 3.2. For analysis of this 2-port antenna, Antenna 1 is excited, and Antenna 2 is terminated with a matched load. When this MIMO antenna is simulated without decoupling units, i.e., stage 1, the corresponding S-parameters and current distributions are shown in Fig. 3.3(a) and Fig. 3.4(a), respectively. $|S_{11}|$ are found to be good. It is noted that the lower frequency band resonance is due to the current vectors in the outer ring. However, the higher frequency band is due to the surface currents in the middle ring and the circular patch. The MC between antenna elements is observed to be $\geq$ -10 dB in the lower band and $\geq$ -15 dB in the upper band, which needs to be reduced further for better MIMO performance. For doing so, the antennas are connected with a neutralization line (AB), as shown in stage 2.

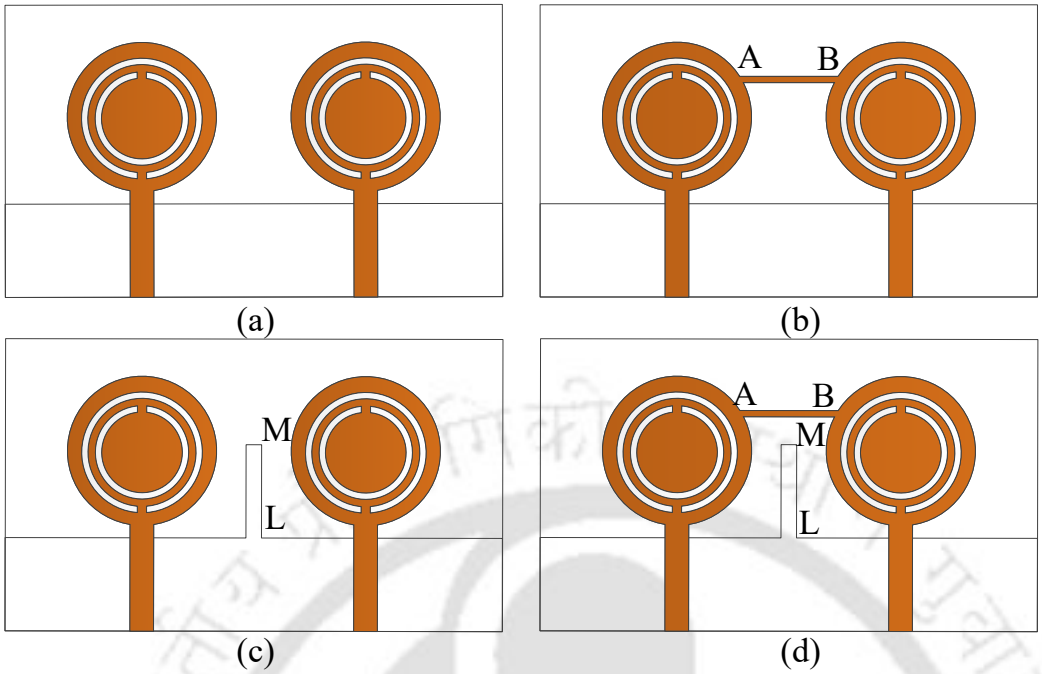

Fig. 3.2: Intermediate design stages before the final design: (a) stage 1, (b) stage 2, (c) stage 3, and (d) stage 4.

The surface current plot for this stage reveals that currents in Antenna 2 reduce significantly in the regions responsible for the lower frequency band. However, surface currents in the middle ring and circular patch do not weaken at the higher frequency band. Hence, neutralization line AB is capable of enhancing the isolation in the 2.5 GHz band only and unable to reduce the MC in the 3.5 GHz band. Stage 3 examines the capability of the grounded stub LM, which is $\lambda_g/4$ in length at 3.5 GHz. The S-parameters of stage 3 indicate that the MC in the 3.5 GHz band can be reduced by extending a $\lambda_g/4$ long grounded stub. Surface current plot corresponding to stage 3 indicate that the grounded stub is unable to reduce the surface current in the outer ring at the lower frequency band. However, at the higher frequency band, it reduces the surface currents effectively in the parts of Antenna 2, accountable for the higher frequency band. Therefore, the grounded stub can reduce the MC below -15 dB in the 3.5 GHz band, but not in case of the 2.5 GHz band. Next, an attempt has been made to reduce the MC in both frequency bands, resulting in stage 4, which is a combination of stages 2 and 3. It can be seen in Fig. 3.3(d) that the NL and the GS together cannot reduce the MC below -15 dB in both frequency bands. When Antenna 1 is excited at the higher frequency band, the current distribution in the interior part of Antenna 2 diminishes. Still, significant currents is seen in

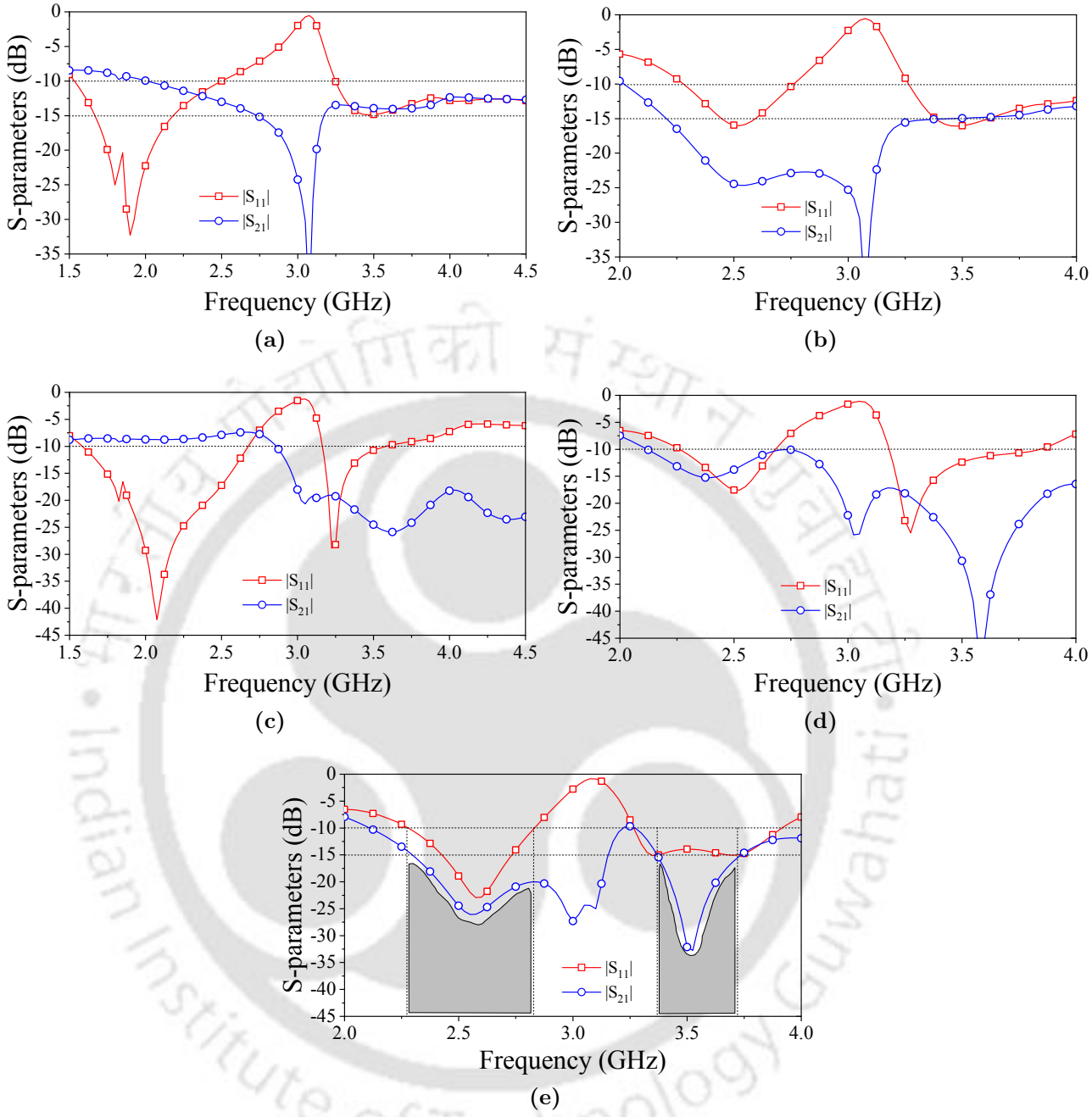

Fig. 3.3: S-parameters: (a) stage 1, (b) stage 2, (c) stage 3, (d) stage 4, and (e) final stage (Fig. 3.1).

its outer ring (refer to Fig. 3.4(d)). By observing the direction of current vectors, it is found that they are very similar to Stage 1 in the lower frequency band but tilted because Antenna 2 is excited by the neutralization line link. Hence, these currents can not increase the coupling at the higher frequency band. Therefore, with both the NL and the GS, the isolation is high enough only in the 3.5 GHz band, while both $|S_{11}|$ and $|S_{21}|$ become poorer in the 2.5 GHz band compared to the second stage. For achieving high isolation in both frequency bands, the

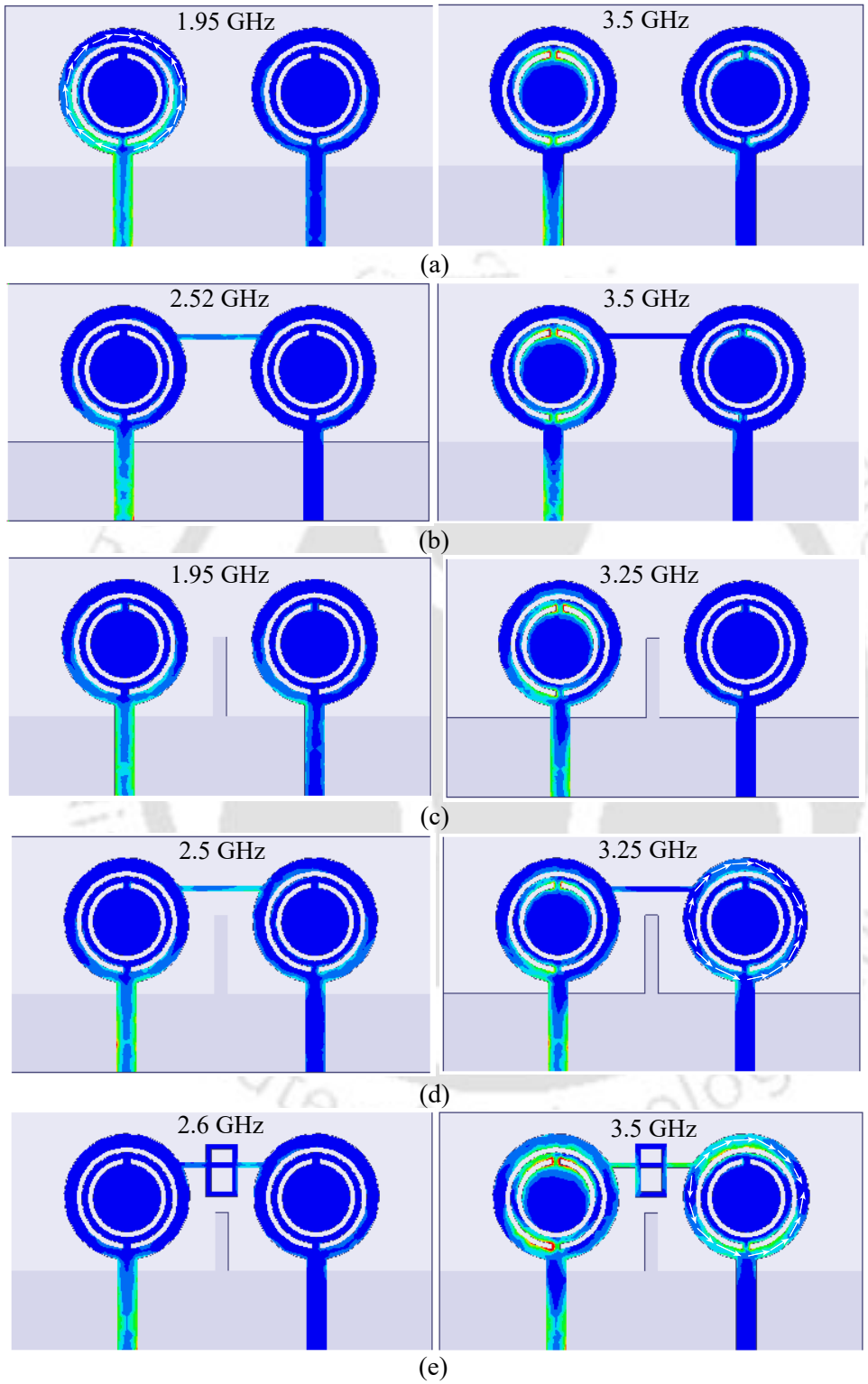

Fig. 3.4: Current distribution: (a) stage 1, (b) stage 2, (c) stage 3 (d) stage 4, and (e) final stage.

final design is obtained by connecting an additional rectangular loop PQRS to the NL of stage 4. This loop provides two more NL paths (A-P-S-B, A-Q-R-B) in addition to the path AB. It is observed that with a slight reduction in the length of the grounded stub LM and placement of the rectangular loop with the neutralization line AB, the MC in both the bands falls below -15 dB with a minimum of -25 dB in the 2.5 GHz band and -32 dB in the 3.5 GHz band. The surface current plots for the final stage are given in Fig. 3.4(e). Note that the magnitude of the surface currents in Antenna 2 because of Antenna 1 excitation does not reduce efficaciously in the outer ring part. However, this surface current does not contribute to the mutual coupling at the higher frequency band because of a reason similar to that explained for stage 3. The frequency range where $|S_{11}|$ is $\leq$ -10 dB and $|S_{21}| \leq$ -15 dB, is shaded with the grey colour in Fig. 3.3(e).

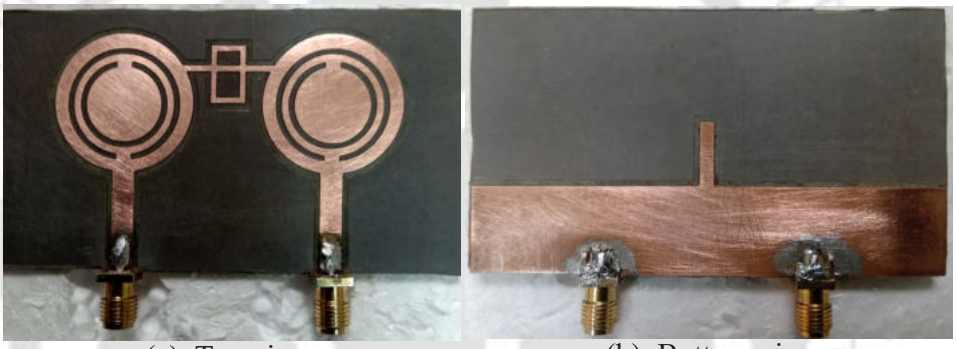

(a) Top view (b) Bottom view

Fig. 3.5: Fabricated prototype.

3.2.4 Antenna Performance

A prototype of the proposed MIMO antenna is fabricated and shown in Fig. 3.5. The measured and simulated $|S_{11}|$ and $|S_{21}|$ values are plotted against frequency in Fig. 3.6. The -10 dB simulated impedance bandwidth of the antenna lies between 2.3 to 2.825 GHz and 3.375 to 3.725 GHz. The isolation between antenna elements is found to be more than 15 dB. However, the -10 dB measured impedance bandwidth of the fabricated prototype is noted from 2.4 to 2.84 GHz and 3.5 to 3.95 GHz. The measured isolation is higher than 10 dB from 2.55-2.84 GHz and 3.5-3.95 GHz, and for the frequency range from 2.55-2.84 GHz and 3.5-3.65 GHz, the isolation is noted to be more than 15 dB with the maximum isolation of 23.98 dB in the 2.6 GHz band and 20 dB in the 3.5 GHz band. The slight mismatch in the simulated

and measured S-parameters is because of the tolerances in the fabrication and measurement process.

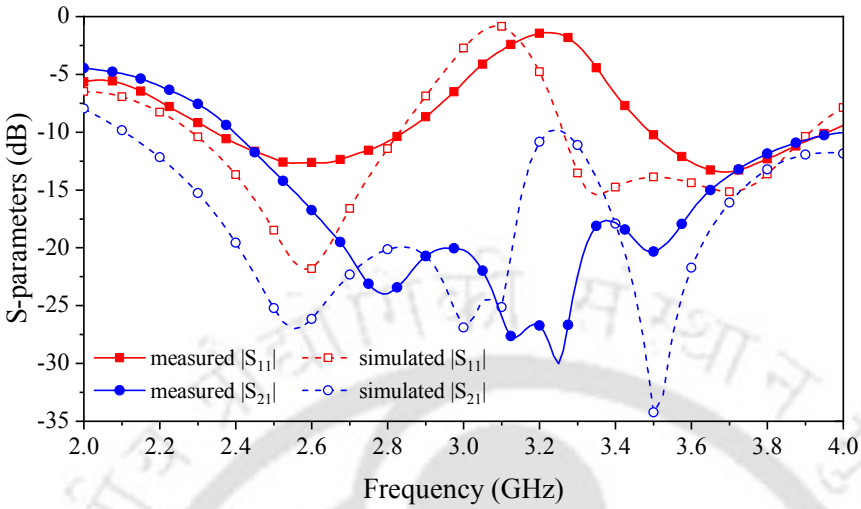

Fig. 3.6: Simulated and measured S-parameters.

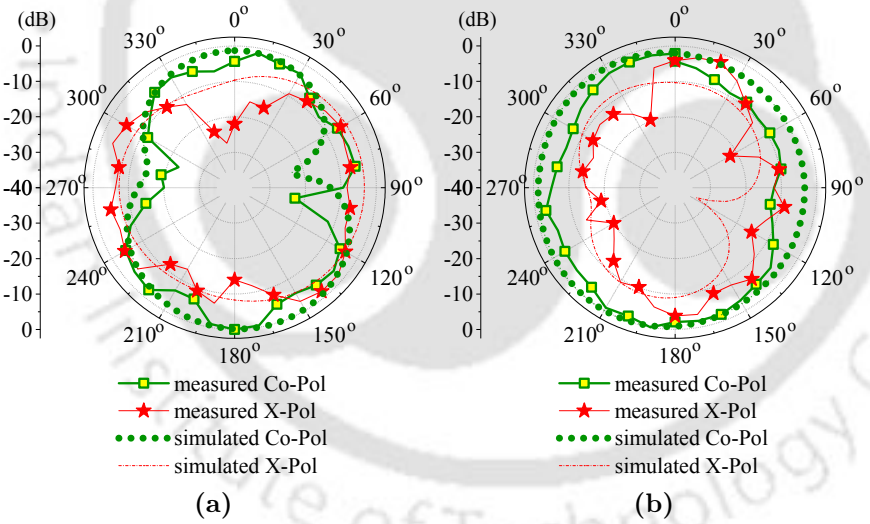

Fig. 3.7: Radiation patterns at 2.6 GHz: (a) $\phi = 0^0$ plane and (b) $\phi = 90^0$ plane.

The simulated and measured radiation patterns for $\phi = 0^0$ and $\phi = 90^0$ planes at 2.6 GHz and 3.5 GHz are plotted in Figs. 3.7 and 3.8, respectively. Only the concerned port is excited during the pattern measurements, while the other is terminated with a 50 Ω matched load. It is observed that the radiation patterns corresponding to port A are the mirror image of the radiation pattern corresponding to port B, thus exhibiting pattern diversity. Therefore, the radiation patterns corresponding to only port B are shown. The measured gain versus

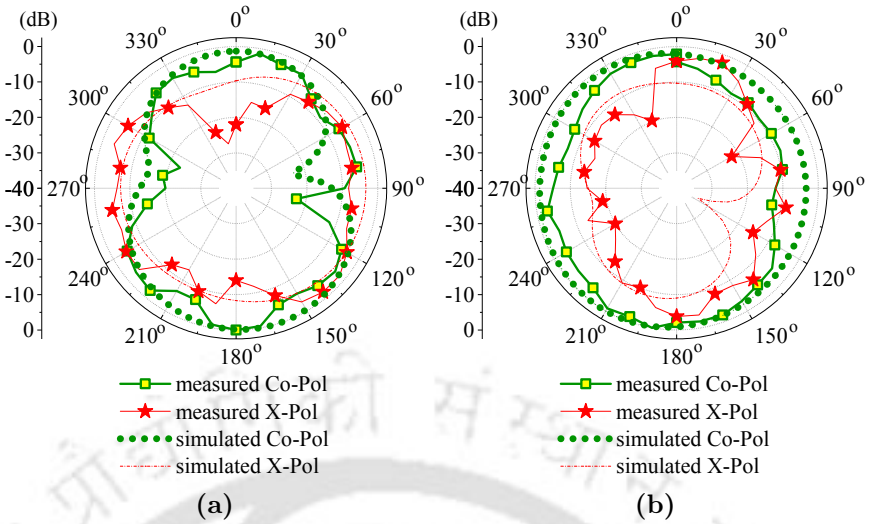

Fig. 3.8: Radiation patterns at 3.5 GHz: (a) $\phi = 0^0$ plane and (b) $\phi = 90^0$ plane.

frequency plot is shown in Fig. 3.9. It can be observed that the simulated gain ranges from 1.77 to 3.77 dBi, while the measured gain lies between 1 to 3.66 dBi.

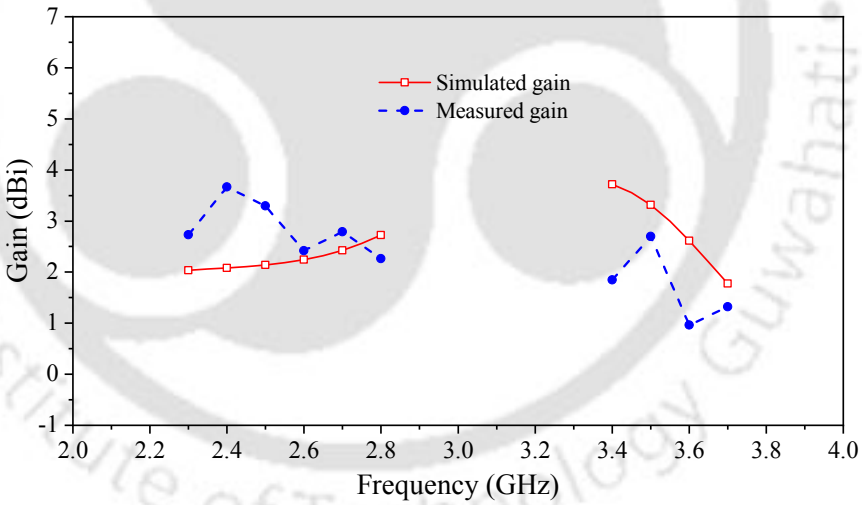

Fig. 3.9: Simulated and measured gain versus frequency.

The value of ECC is calculated using (1.12) and (1.13) from chapter 1 and is plotted in Fig. 3.10. The ECC for this dual-port MIMO antenna is noted to be less than 0.0465. The correlation among antennas causes a loss in the channel capacity of a MIMO system. Based on the assumption that this MIMO antenna is used at both transmitter and receiver sides to realize a 2×2 MIMO communication system. The CCL for such a MIMO system due to the correlation is calculated using (1.24) from chapter 1 and plotted in Fig. 3.10. The CCL for this

MIMO system is noted to be less than 0.137 bits/s/Hz.

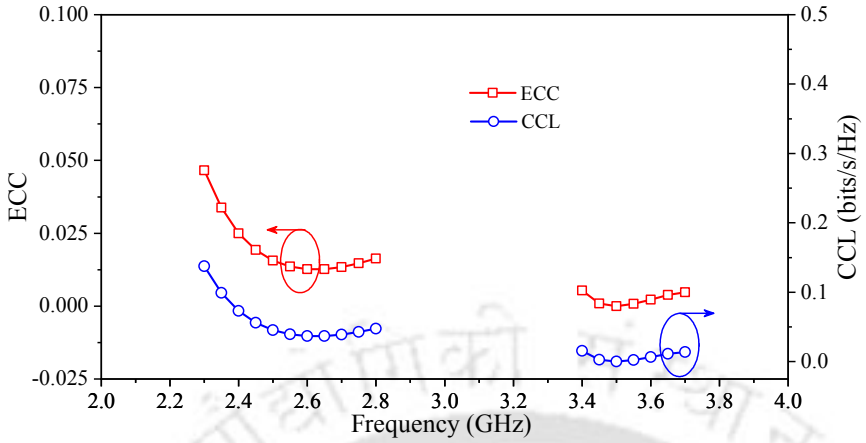

Fig. 3.10: ECC and CCL versus frequency.

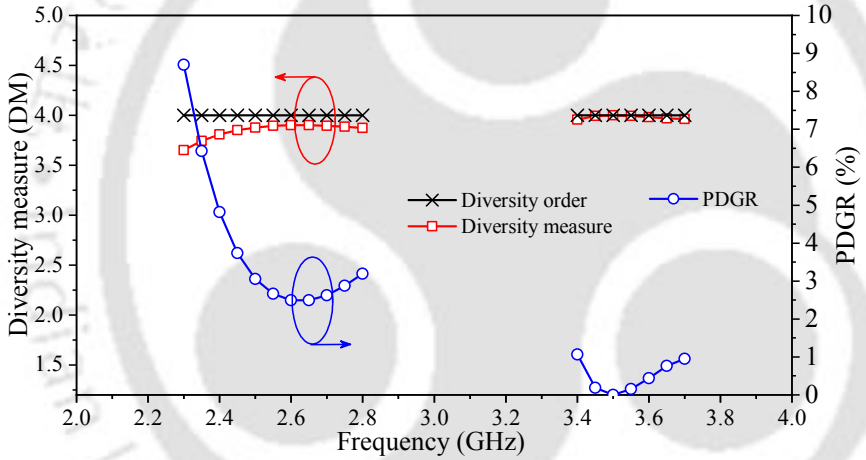

Fig. 3.11: DM and PDGR versus frequency.

Using (1.18), the DO for the above-described 2×2 MIMO system is four across the antenna bandwidth. The DM is calculated using (1.19) and plotted along with the DO in Fig. 3.11. The percentage diversity gain reduction (PDGR) is a parameter that measures the reduction in the diversity performance of a MIMO antenna due to the correlation between antennas. The PDGR versus frequency curve is plotted in Fig 3.11 and is noted to be less than 8.7 %.

In a multi-user MIMO scenario, the channel capacity loss is measured as sum rate loss (SRL). Three mobile terminals (each having this two-port MIMO antenna) are considered for the SRL analysis in accordance with Fig. 1.11 of chapter 1. The SRL is calculated using (1.25) and plotted in Fig. 3.12. It is noted below 1×10^{-7} bits/s/Hz.

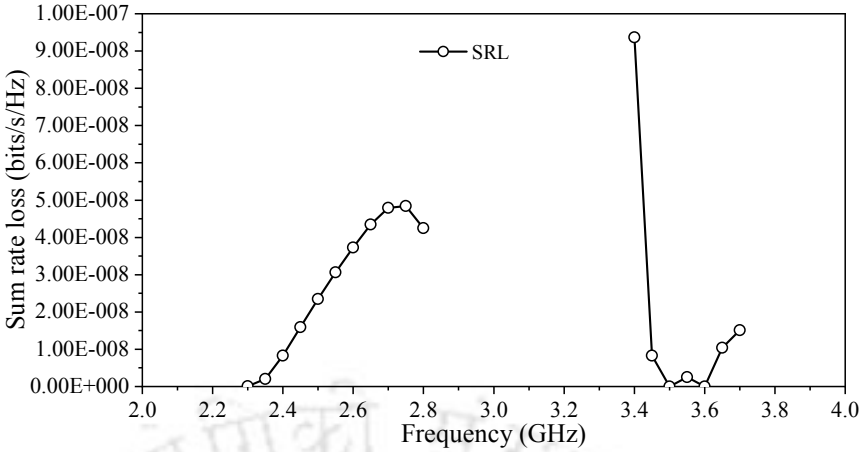

Fig. 3.12: SRL versus frequency.

3.3 Low Mutual Coupling Six-Port Planar Antenna for the MIMO Applications

3.3.1 Introduction

The channel capacity of the i.i.d. Rayleigh faded MIMO channel varies linearly with the minimum number of antennas on the transmitter and receiver sides. Therefore, using multiple antenna elements in MIMO communication systems enables us to achieve higher data rates. Various 6-port MIMO antennas are discussed in [78–81], and it has been noted that all of them have non-planar geometry. An orthogonal arrangement of three two-port antennas reduces the MC in a six-port antenna design with the drawback of its 3-D structure [78]. In [79], a 6-port antenna is created by placing six antennas on a bulky hollow pyramidal-shaped metal frame with grooves between antenna elements for MC reduction. Six 3-D planar inverted F-antennas fixed on six dielectric cubes are presented in [80] and have an isolation of only 10 dB among the antenna elements. In [81], four leaf-shaped notch antennas and two leaf-shaped monopole antennas are used to realize a 6-port MIMO antenna with an isolation of 12 dB. This design uses a reflector that increases the antenna profile. The above-discussed six-port MIMO antennas have non-planar geometry. Note that when the number of antenna ports exceeds three or four, it becomes difficult to control the coupling between antenna elements in planar configurations. In this part of the chapter, mutual coupling in a six-port antenna is reduced using the NL technique. Note that the NL technique is not new. However, the proposed six-port antenna

design using NLs provides a novel configuration that can achieve an inter-element spacing of 0.076 λ_h (λ_h = highest operating wavelength) with reduced MC in the planar structure. Six NLs are inserted between the six antenna elements to reduce the MC using self-cancellation of the induced near-field surface currents. The isolation between all the antenna elements is more than 15 dB in the operating frequency range. Among the 6-port MIMO antennas reported recently, the proposed MIMO antenna has a simple and planar structure with satisfactory performance.

3.3.2 Antenna Geometry

The structure of the proposed six-port planar MIMO antenna is shown in Fig. 3.13. A hexagonal-shaped substrate of Rogers RT-Duroid 5870 (ϵ_r=2.33, tan δ=0.0012) is used to design this MIMO antenna. This antenna uses six circular-shaped monopole patches as radiators in its top layer. The bottom layer is printed below the 1.57 mm thick substrate and serves as the ground plane. A separate microstrip line feeds the signal to every monopole antenna. Note that six ports are placed at the center of each side of the hexagonal substrate. The adjacent antenna elements are connected with the neutralization lines AB, CD, EF, GH, IJ, and KL. The values of various design parameters are as follows: $L_f = 18$, $W_f = 18$, $a = 12$, $d = 6.6$, $g = 0.87$, $L_{PQ} = 70$. All dimensions are in mm.

3.3.3 Working Mechanism

The proposed MIMO antenna uses circular monopole patches as radiating elements. To understand its working mechanism, antenna A_1 is excited through Port 1, and the remaining ports are terminated with a 50 Ω matched load. The S-parameters without the NLs are plotted in Fig. 3.14. It is observed that circular monopole patches resonate at two different frequencies, 1.7 GHz, the lower resonating frequency (LRF), and a higher-order resonance at 4.2 GHz, as seen from the S-parameters plot. The LRF can be calculated using (3.1) from [82].

$$\mathrm{LRF(GHz)} = \frac{7.2}{(2.25a + g)\sqrt{\epsilon_\mathrm{r}}} \tag{3.1}$$

Here, a (cm) is the diameter of the circular patch, g (cm) is the lateral gap between the ground plane (bottom layer) and patch, and ϵ_r is the dielectric constant of the substrate. Note that the above equation is valid only for an isolated patch, which is not inter-connected to its

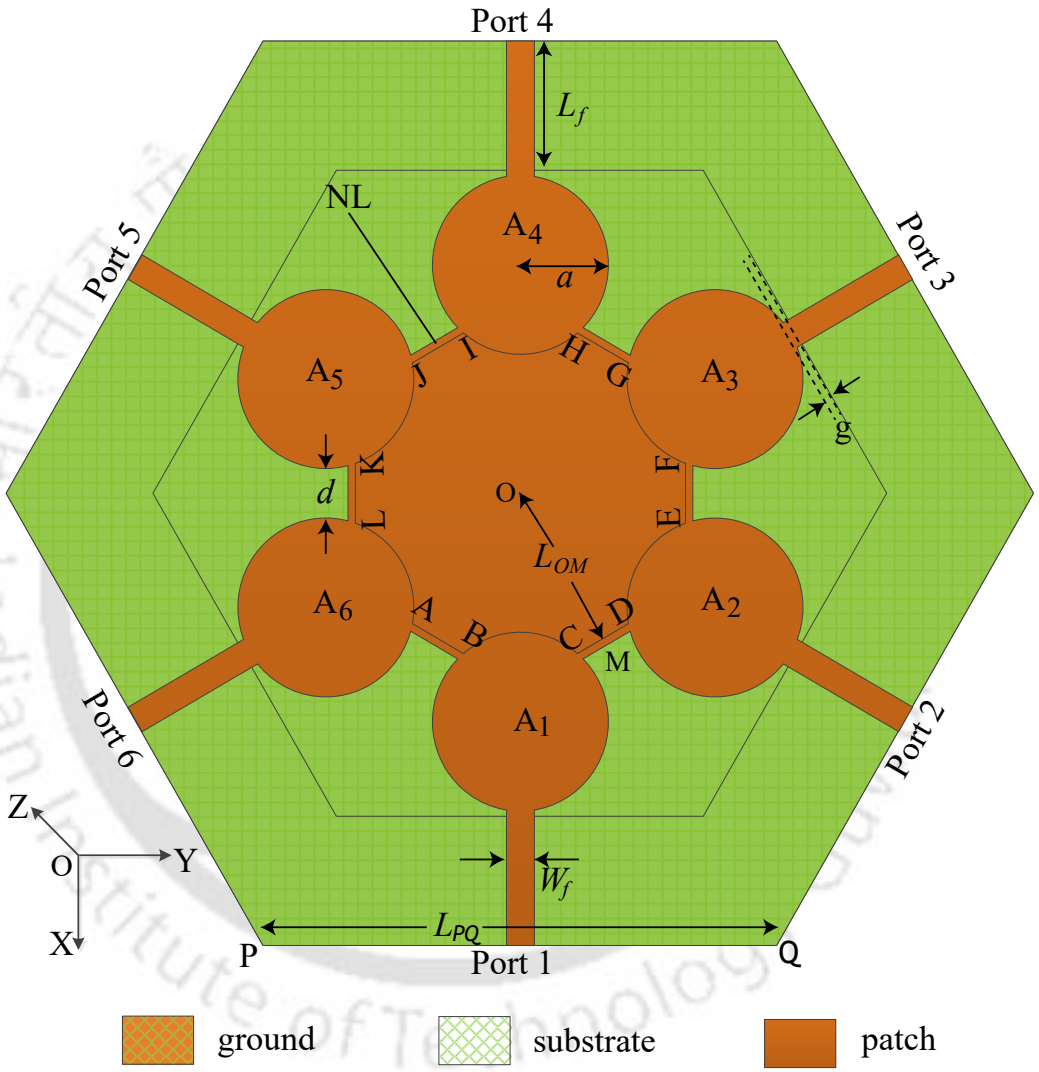

Fig. 3.13: Antenna geometry and design.

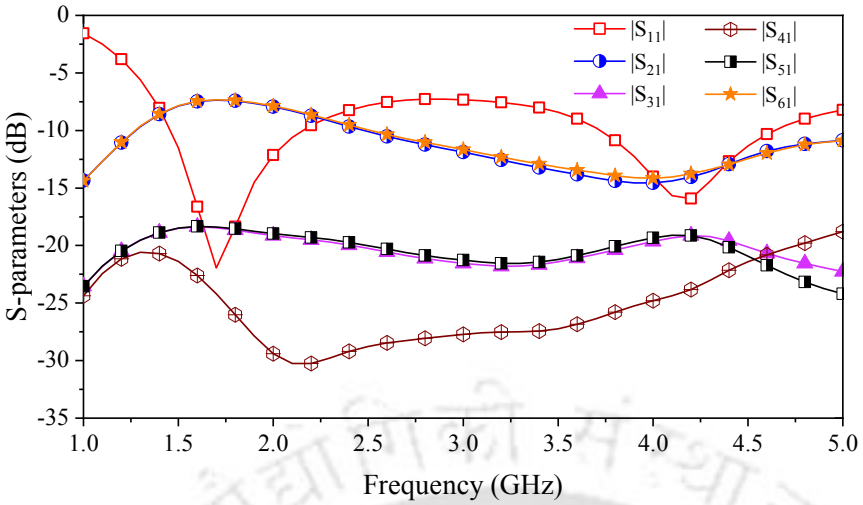

Fig. 3.14: Simulated S-parameters without the NLs.

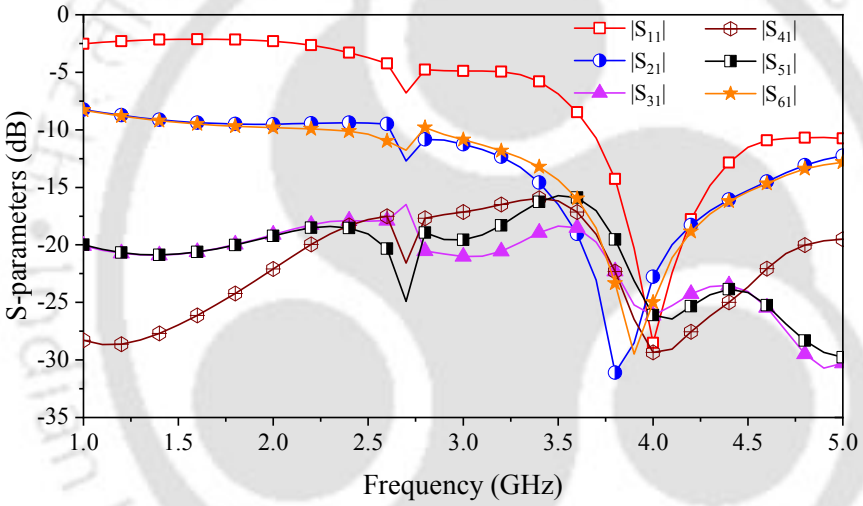

Fig. 3.15: Simulated S-parameters with the NLs.

neighbouring patches through the NLs.

In the following step, the circular monopoles are connected using the NLs for MC reduction. Again during the analysis, only antenna A_1 is excited, and the remaining ports are terminated with a 50 Ω matched load. The S-parameters for this configuration are shown in Fig. 3.15. Note that the lower resonant frequency band is not observed. It is because the NLs alter the current distribution in the circular monopole and reduce the effective resonating length of antenna A_1. To explain this further, the surface current vector plots of antenna A_1 are shown in Fig. 3.16. It can be inferred that the decrease in effective resonating path length is responsible for the upward shift in the LRF of the circular monopole antenna from 1.7 to 4 GHz. It can

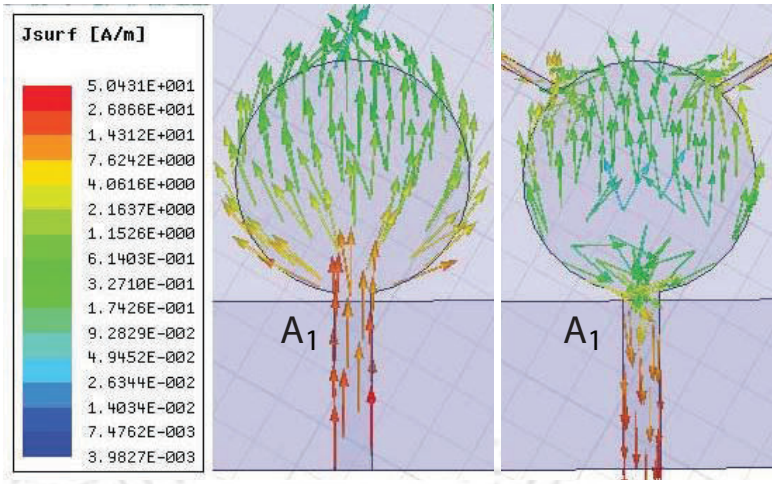

Fig. 3.16: Surface current vectors in antenna A_1 at 1.7 GHz: (a) without the NLs (b) with the NLs.

be also noted that the antenna with the NLs has a wide bandwidth (from 3.44 to 4.68 GHz) as compared to the configuration without the NLs at higher frequency band.

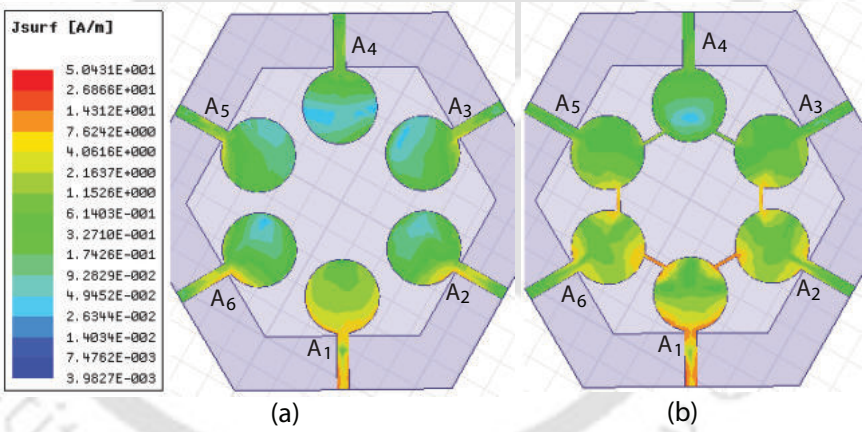

Fig. 3.17: Surface current plot at 4 GHz: (a) without the NLs (b) with the NLs.

The scalar current distributions for the above-discussed configurations (at 4 GHz) are shown in Figs. 3.17(a) and 3.17(b), respectively. With the NLs, the magnitude of the induced surface currents in feed lines of neighbouring antennas (A_2 and A_6) reduces compared to the antenna configuration without the NLs. However, it is observed that the magnitude of the surface currents induced in the circular patches of the neighbouring antennas (A_2 and A_6) increases, but a part of the induced currents also oppose the exciting current vectors, thus helping in MC reduction. The same is illustrated in Figs. 3.18 and 3.19, which show vector current distributions at 4 GHz without and with the NLs, respectively. The current induced in the

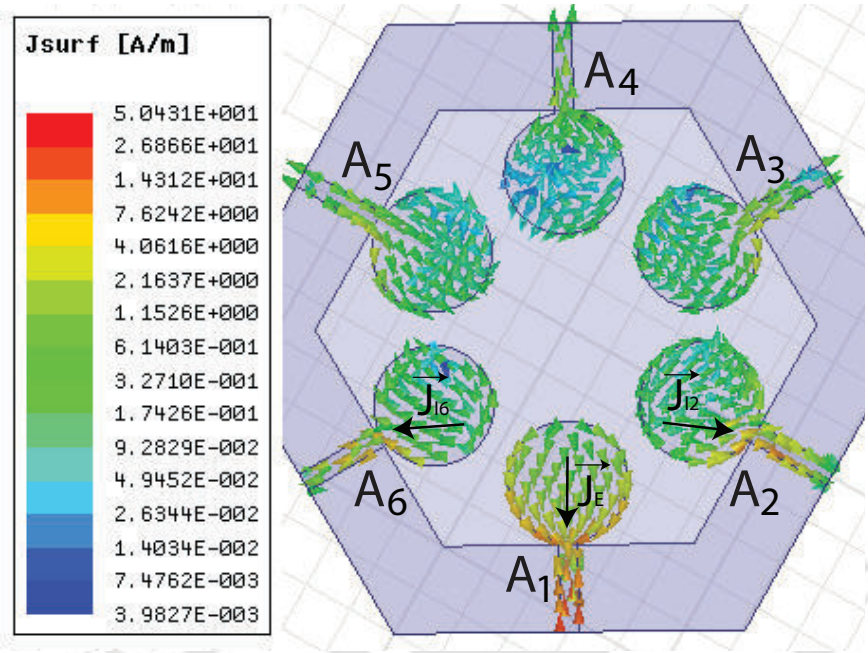

Fig. 3.18: Surface current vectors without the NLs at 4 GHz.

antenna A_1 because of the excitation signal is referred to as the exciting current. The excitation current vectors of antenna A_1 induce currents in antennas A_2 and A_6 because of the near-field interaction. It is observed in Fig. 3.18 that without NLs, the induced current vectors ($\vec{J}_{I2}$ and $\vec{J}_{I6}$) are not opposing the excitation current vectors ($\vec{J}_E$) in antenna A_1 and the mutual coupling is relatively higher at the 4 GHz frequency band. When the adjacent antenna elements are connected through NLs, the current distributions in antennas A_1, A_2, and A_6 change. It is found that the induced current vectors ($\vec{J}_{I2}$ and $\vec{J}_{I6}$) in antenna A_2 and antenna A_6 oppose the excitation current vectors in antenna A_1 ($\vec{J}_{Ea}$ and $\vec{J}_{Eb}$), as shown in Fig. 3.19, thus contributing to the isolation enhancement.

It can be also seen that the current vectors in the NLs ($\vec{J}_{N2}$ and $\vec{J}_{N6}$) oppose the excitation current vector ($\vec{J}_{Ea}$ and $\vec{J}_{Eb}$) in antenna A_1 as depicted in Fig. 3.19. It is also noticed that when the NLs are shifted away from the center of the hexagon (point O) towards the edge of the substrate by a distance L_{OM} (refer to Fig. 3.13), the isolation among neighbouring antennas becomes more than 15 dB. An optimal performance is obtained when length $L_{OM} = 23$ mm. It can be seen from antenna geometry (in Fig. 3.13) that the inter-element spacing (d) between the radiating patches is directly proportional to the side length (L_{PQ}) of the hexagonal substrate. Therefore, the effect of the inter-element spacing on antenna performance can be understood by

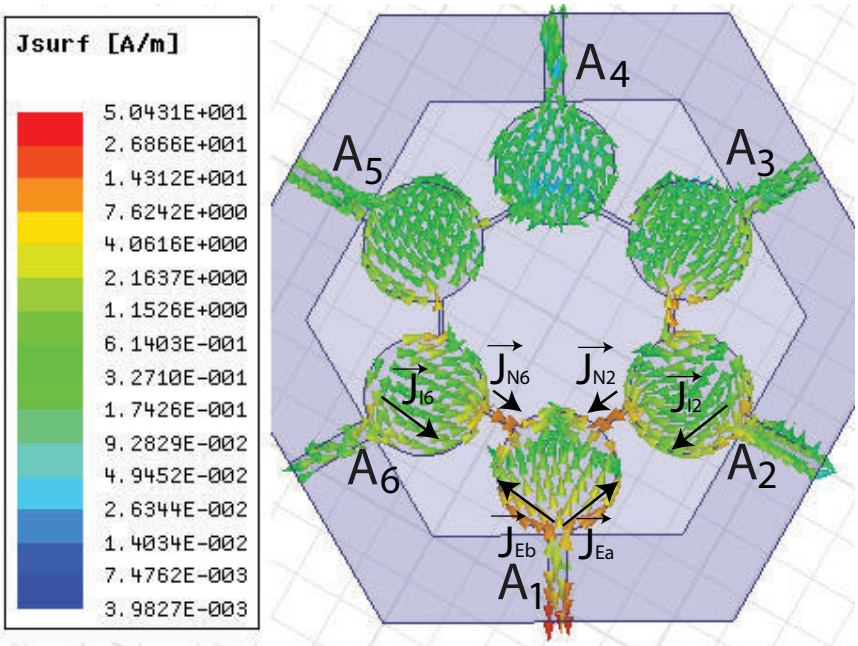

Fig. 3.19: Surface current vectors with NLs at 4 GHz.

varying L_{PQ}. The S-parameters for different values of L_{PQ} with the corresponding inter-element spacing (d) are shown in Fig. 3.20. For L_{PQ} = 65 mm, at the resonating frequency of 4.7 GHz, the MC between all the antennas is below -13.23 dB. For L_{PQ} = 67.5 mm, at the resonating frequency of 4.3 GHz, the MC between all the antennas is below -20.7 dB. For L_{PQ} = 70 mm, at the resonating frequency of 4 GHz, the MC between all the antennas is below -22.76 dB. For L_{PQ} = 72.5 mm, at the resonating frequency of 3.8 GHz, the MC between all the antennas is below -20.7 dB. For L_{PQ} = 75 mm, at the resonating frequency of 3.4 GHz, the MC between all the antennas is below -20.9 dB. Therefore, from Fig. 3.20, it is concluded that the MC deteriorates when L_{PQ} is reduced below 70 mm. Also, the resonance shifts rightward towards the higher frequencies. When L_{PQ} is increased above 70 mm, d increases, and resonance shifts to the left towards the lower frequencies. However, as the primary design goal is to obtain the minimum MC among all antenna elements at the resonating frequency, the 70 mm side length is our choice for this parameter while considering both the optimal antenna performance and size.

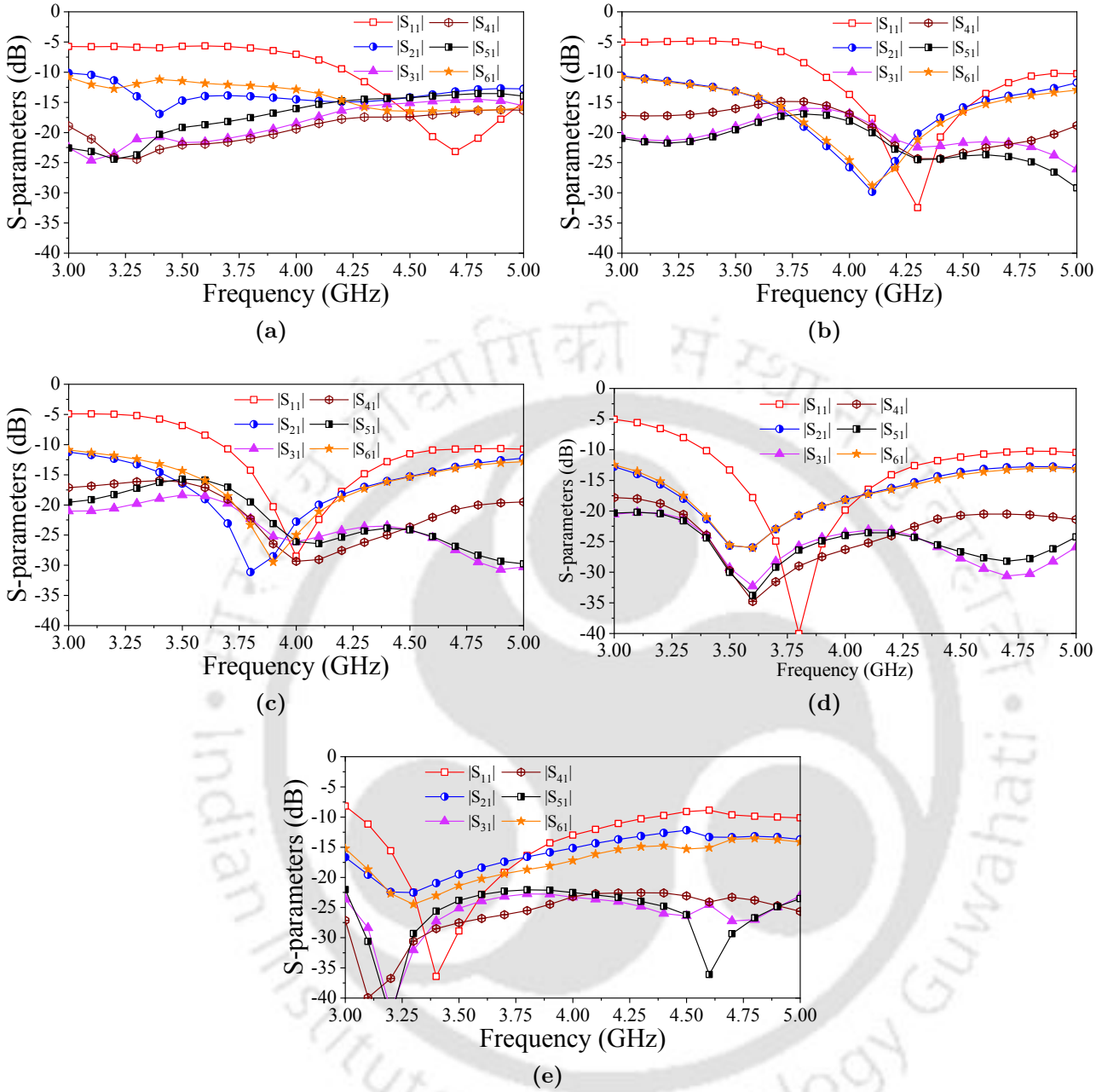

Fig. 3.20: S-parameters for varied side length (L_{PQ}) and corresponding inter-element spacing (d): (a) L_{PQ} = 65 mm, d = 2.29 mm, (b) L_{PQ} = 67.5 mm, d = 4.46 mm, (c) L_{PQ} = 70 mm, d = 6.62 mm, (d) L_{PQ} = 72.5 mm, d = 8.79 mm, (e) L_{PQ} = 75 mm, d = 10.95 mm.

3.3.4 Antenna Performance

The antenna prototype is fabricated and experiments are performed inside an anechoic chamber to validate the simulated results, as shown in Fig. 3.21.

The measured $|S_{1j}|$ for j = 1, 2,..., 6, are plotted as functions of frequency in Fig. 3.22

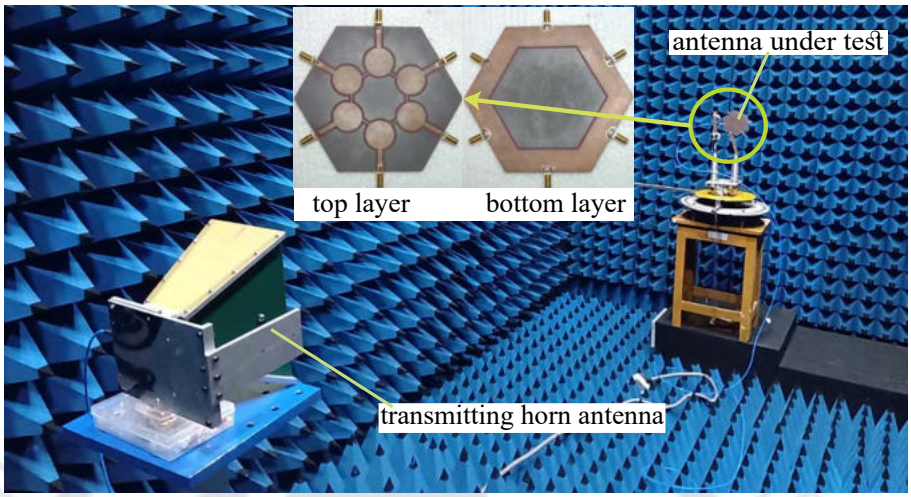

Fig. 3.21: Measurement set-up (Inset: top and bottom views of fabricated antenna prototype).

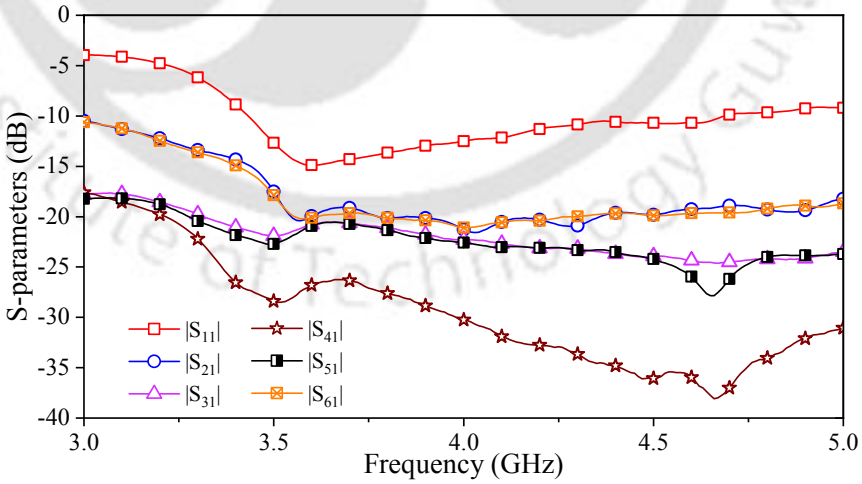

Fig. 3.22: Measured S-parameters of the fabricated prototype.

and the simulated S-parameters are plotted in Fig. 3.15. The -10 dB simulated impedance bandwidth of this MIMO antenna lies between 3.67 and 4.53 GHz, and the isolation among all the antenna elements is found to be more than 15 dB. The -10 dB measured impedance bandwidth of the fabricated prototype is noted from 3.44 to 4.68 GHz. The measured isolation among all the ports is greater than 15 dB from 3.44 to 3.56 GHz and more than 20 dB beyond 3.56 GHz. Moreover, it is also noted that $|S_{21}|$, $|S_{61}|$ and $|S_{31}|$, $|S_{51}|$ are coinciding because of the symmetric location of Port 2 & Port 6 and Port 3 & Port 5 with respect to Port 1. The slight mismatch in the simulated and measured S-parameters is because of the tolerances in the fabrication and measurement process.

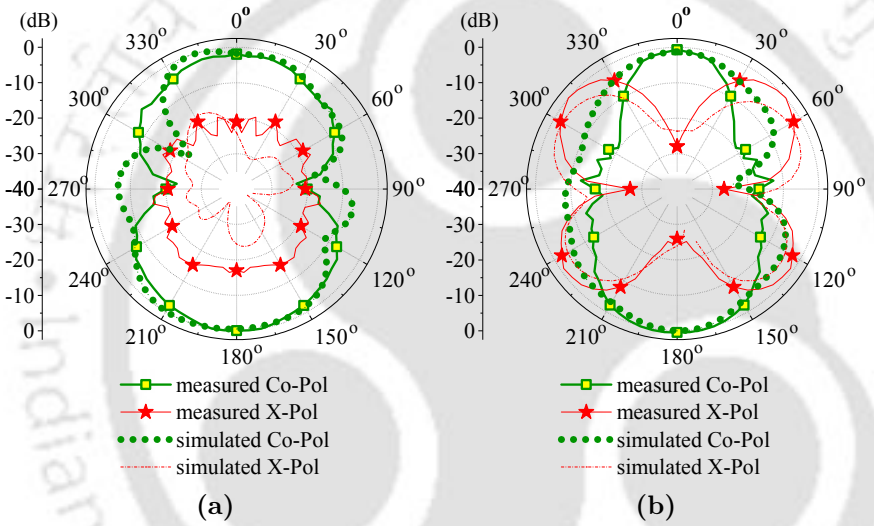

Fig. 3.23: Radiation patterns at 4 GHz: (a) $\phi = 0^0$ plane and (b) $\phi = 90^0$ plane.

The simulated and measured radiation patterns of the proposed antenna in $\phi = 0^0$ and $\phi = 90^0$ planes for port 1 are plotted in Fig. 3.23, while the remaining antenna ports are terminated with a 50 Ω matched load. It is noted that the maximum of the main beam is in the direction $\theta = 0^0$ in both planes. The radiation patterns for only port 1 is plotted as all other ports are symmetrical in the antenna design. Cross-polar discrimination (XPD) of 19 dB in $\phi = 0^0$ and 27 dB in $\phi = 90^0$ planes are observed in the broadside direction of the radiation pattern at 4 GHz.

The simulated, measured gain, and antenna efficiency versus frequency curves are plotted in Fig. 3.24. The measured peak gain is 5.1 dBi, and the antenna efficiency is found to be lying between 83% to 88 %.

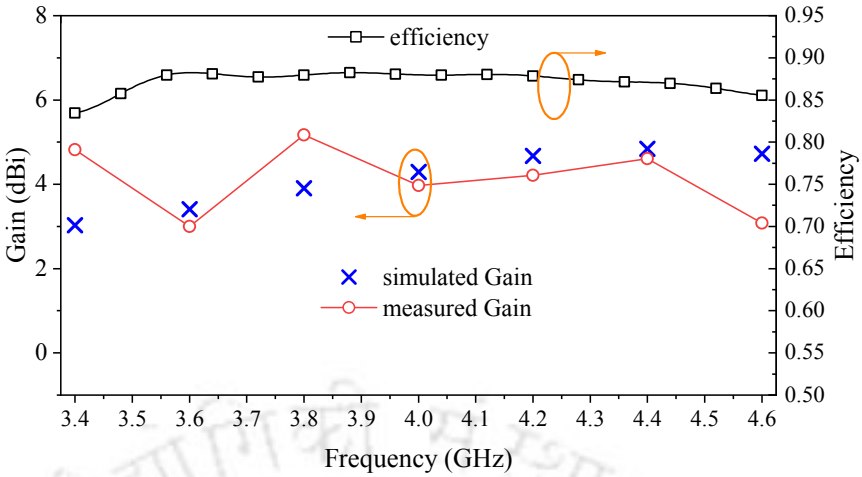

Fig. 3.24: Measured, simulated gain, and simulated radiation efficiency.

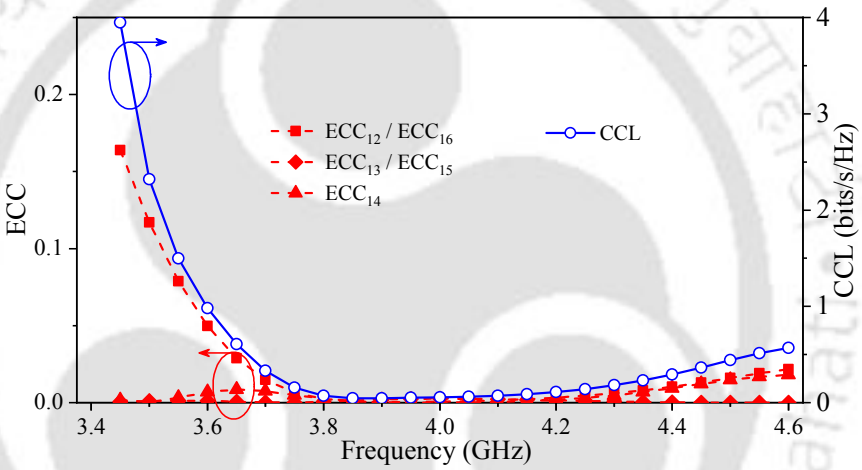

Fig. 3.25: ECC and CCL versus frequency.

The ECC is calculated using (1.12) and (1.13) from chapter 1 and is plotted in Fig. 3.25. The ECC for this six-port MIMO antenna is noted to be less than 0.049 from 3.6 to 4.6 GHz. The correlation among antennas causes a loss in the channel capacity of a MIMO system. Based on the assumption that this MIMO antenna is used at both transmitter and receiver sides to realize a 6×6 MIMO communication system. The CCL for such a MIMO system due to the correlation is calculated using (1.24) from chapter 1 and plotted in Fig. 3.25. The CCL for this MIMO system is noted to be less than 0.98 bits/s/Hz from 3.6 to 4.6 GHz.

Using (1.18), the DO for the above-described 6×6 MIMO system is six across the antenna bandwidth. The DM is calculated using (1.19) and plotted along with the DO in Fig. 3.26. The PDGR, a measure of reduction in the diversity performance, is plotted in Fig. 3.26 and is

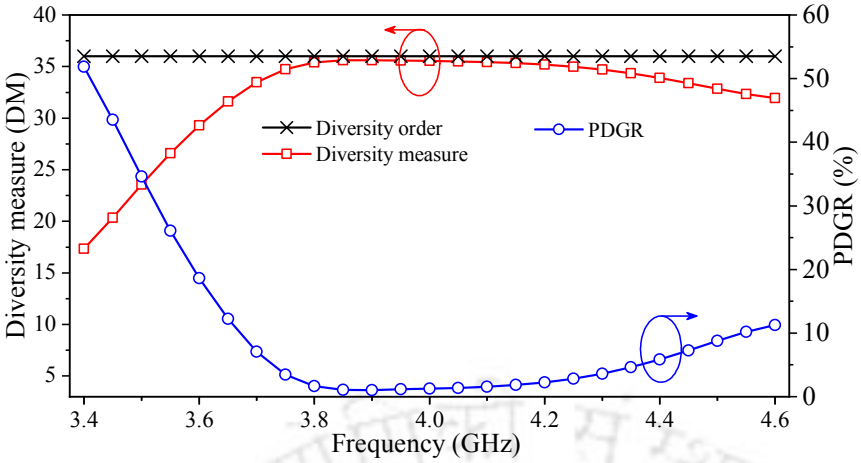

Fig. 3.26: DM and PDGR versus frequency.

noted to be less than 18.6 % from 3.6 to 4.6 GHz.

Table 3.1: Comparison of the proposed work with other 6-port MIMO antennas.

Refs.	BW	A_S	I_S	MC	G_P	S_T
[78]	2.45	0.43×0.43×0.43	NA	≤ -9	1.8-3.7	Non-planar
[79]	5.15-5.825	2.45×2.14×0.48	NA	≤ -45	6-7	Non-planar
[80]	1.88-1.9, 2.3-2.6	0.85×0.43×0.037	0.306	≤ -10	1	Non-planar
[81]	7-10	1.16×1.86×0.28	0.38	≤ -12	3-7	Non-planar
Prop.	3.44-4.68	1.6×1.37×0.018	0.076	≤ -15	3-5.1	Planar

Abbreviations: Refs.: references, BW: impedance bandwidth (GHz), λ_h: highest operating wavelength, A_S: antenna size (in λ_h^3), I_S: inter-element spacing (edge-to-edge in λ_h), MC: mutual coupling in dB, G_P: peak gain in dBi, S_T: structure type, Prop.: proposed work, NA: information not available.

The comparison of the proposed work with other contemporary works is listed in Table 3.1. It indicates that the proposed MIMO antenna has overall better performance than other works. The proposed six-port MIMO antenna has higher isolation than the other reported antennas except for the one in [79]. However, the latter occupies approximately 64 times more volume (λ_h^3) than our antenna. It is also noted that the antenna presented here has a lower size (λ_h^3) than the rest, except for the antenna in [80]. However, the proposed six-port antenna

has a higher isolation, better gain, and much lower inter-element spacing than the antenna in [80]. Our proposed antenna has higher gain than others except for antennas in [79] and [81]. Our proposed antenna has a broader bandwidth (fractional bandwidth) than all other antennas except for the one in [81]. But the antenna in [81] occupies approximately 15 times more volume than our antenna. Moreover, the antenna presented here has less fabrication complexity than the rest because of its planar and simple geometry.

3.4 Conclusions

In this chapter, two MIMO antennas (dual-port and 6-port) utilizing the NL technique for MC reduction are designed, fabricated, and tested. For the dual-port antenna, the MC in both the frequency bands (2.3-2.8 GHz and 3.3-3.7 GHz) is reduced with a modified neutralization line and a grounded stub together. This antenna has a bandwidth from 2.3 to 2.8 GHz and 3.37 to 3.72 GHz. It covers 2.4 GHz-WLAN, LTE 38, LTE 40, LTE 41, 3.5 GHz-WiMAX, and 3.3 to 3.7 GHz for 5G applications. The radiation patterns are plotted, and a maximum gain of 3.66 dBi is noted in the operating frequency range of the antenna. Isolation is found to be greater than 15 dB. The ECC is noted to be less than 0.0465, and CCL is found below 0.137 bits/s/Hz. The PDGR is found below 8.7 %. The SRL for this MIMO antenna is below 1×10^{-7} bits/s/Hz. Therefore, this dual-port antenna is suitable for use in multiple-band MIMO applications. For the 6-port MIMO antenna, simulated and measured results are found to be in good agreement with each other. From 3.6 to 4.6 GHz, the isolation is found to be greater than 15 dB, the ECC is noted to be less than 0.049, and the CCL is noted below 0.98 bits/s/Hz. The PDGR is noted below 18.6%, thus making this antenna a suitable candidate for application in MIMO communication systems. Moreover, this 6-port antenna can also be used for altimetry (4.2-4.4 GHz) in unmanned aerial vehicles (UAVs) as a 6-port MIMO antenna for better performance.

4

Space Efficient Meta-grid Lines for Mutual Coupling Reduction

It is understood in chapter 2 that EBGs, isolators, and NLs for MC reduction require extra space between antennas to accommodate them. The ADS for isolation enhancement requires additional layer/layers above the MIMO antenna. Therefore, these techniques increase the antenna profile. In this chapter, meta-grid lines (MGLs) are proposed and designed for MC reduction in printed monopole MIMO antennas and MIMO DRAs. This technique utilizing MGLs neither requires extra space between antenna elements nor involves the arrangement of additional layers like the ADS. Hence, it helps in designing compact two-port MIMO antennas.

4.1 Introduction

It is noted in chapter 2 that EBGs, isolators, and NLs for MC reduction require extra space between antennas to accommodate them. Besides, ADSs or superstrates are placed above the MIMO antenna to reduce the MC between ports. The height of the ADS above the antenna determines the phase of the partially reflected wave, which nullify the effect of the coupled wave. Therefore, these techniques require either extra space or additional layers.

This chapter presents a novel single negative (SNG: μ and ϵ are of opposite signs) meta-grid line (MGL) structure. This MGL structure is used to design the following low MC MIMO antenna configurations:

1. Two-port coplanar waveguide (CPW)-fed monopole MIMO antenna (TPCFMMA)
2. Two-port MIMO DRA (TPMDRA)

Unlike EBGs, isolators, and NLs for MC reduction, this approach obviates the need for any extra space between antennas to accommodate the decoupling unit. Integrating these MGLs in the ground plane for MC reduction does not require any additional layers, unlike ADSs or superstrates that increase the height of the antenna. Therefore, this technique helps to realize the compact design of TPCFMMA with minimal edge-to-edge spacing between the antenna elements ($0.015\lambda_h$).

It is noted that for the TPCFMMA, the unit cell periodicity (p) of the MGL structure is 6.35 mm, and guided wavelength (λ_g) is 57.7 mm whereas, for the TPDRAA, p is 6 mm and λ_g is 34.85 mm at 5.8 GHz. Hence, p is much smaller than the λ_g of the propagating wave (i.e., $p \ll \lambda_g$) [83, 84], so that fields are averaged across the unit cells and see the structure as a homogenous medium at a macroscopic scale. Also, from the extracted permittivity and permeability curves of MGLs for the TPCFMMA and the TPMDRA, it is noted that the MGL structure shows wideband SNG behaviour. Even though the presented structure resembles a DGS (both are etched copper patterns on the ground plane), the former differs significantly from a DGS (which uses a slot of a length comparable to the guided wavelength [36, 37] or half of the guided wavelength [38]) due to its characteristic properties discussed above.

In addition, most MC reduction techniques involving EBG structures and superstrates generally lack portability or interoperability among different types of radiators (patch antenna↔DRA). In other words, EBG structures and superstrates used to reduce the MC in MIMO patch antennas are seldom employed in MIMO DRAs without major structural modifications. However,

this is not the case with the presented technique because, in the TPMDRA, the dielectric blocks are excited by means of microstrip patch feed printed over an MGL (with wideband SNG characteristics) backed substrate. Therefore, MGLs effectively deal with the MC in both printed and dielectric resonator antennas. A notable feature of this decoupling structure is that the antenna's resonating frequency can be adjusted over a wide frequency range (2.6 to 4.4 GHz) by varying MGL's geometric parameters in the case of the TPCFMMA. With changing resonating frequencies, minimal offsets between the resonance and minimal mutual coupling are observed, i.e., the MC performance at resonance remains almost undisturbed. In the TPMDRA design, the resonating frequency can be made to lie at any value between 5.78 and 6.55 GHz by changing the dimensions of annular ring slots in the patch, which excites the DRA. Even in the TPMDRA, the MC performance is preserved while varying antenna resonating frequencies.

This chapter is divided into three sections: Section 4.2 presents the unit cell analysis of the proposed MGL structure. The TPCFMMA is discussed in Section 4.3, whereas the TPMDRA is discussed in Section 4.4.

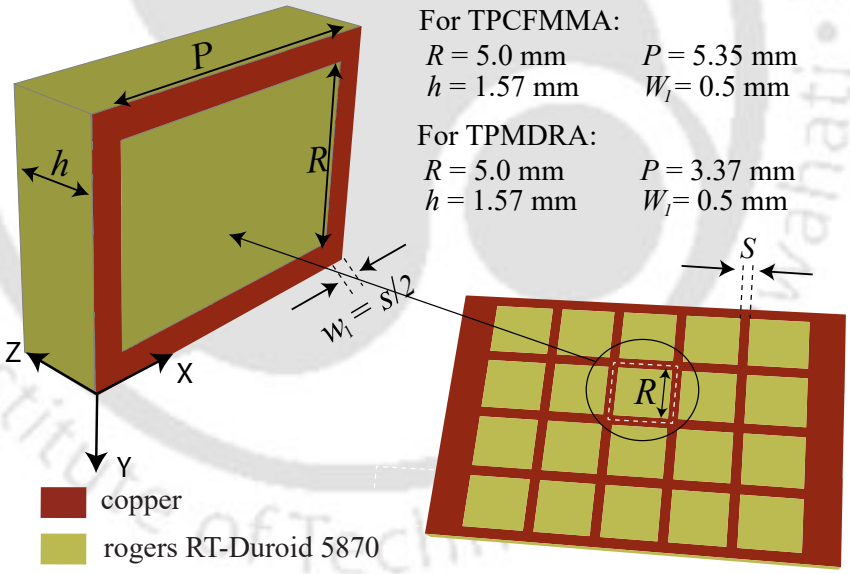

Fig. 4.1: Meta-grid lines unit cell.

4.2 Unit cell analysis

An isolated unit cell (single unit cell) of MGLs to be integrated with the ground plane of MIMO antennas is shown in Fig. 4.1. The MGLs are printed on the back of Rogers RT-Duroid

5870 with $\epsilon_r = 2.33$ and $\tan(\delta) = 0.0012$. The simulation set-up for extracting the real parts of the complex permeability and permittivity of such a unit cell is shown in Fig. 4.2. Using the parameter retrieval option in CST Microwave Studio Suite 2018, the permeability and permittivity curves are plotted in Figs. 4.3(a) and 4.3(b), respectively.

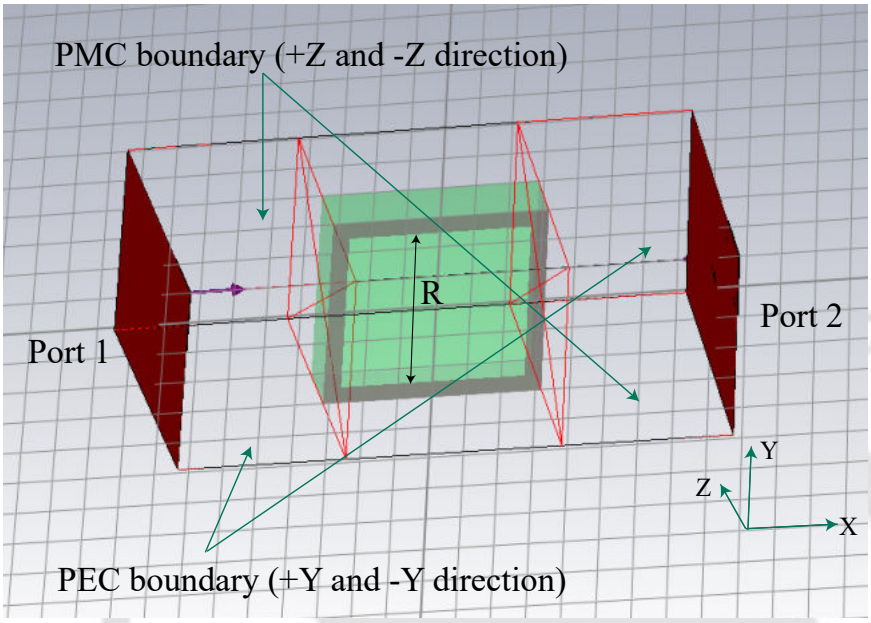

Fig. 4.2: Simulation set-up for effective material parameter extraction.

From Figs. 4.3(a) and 4.3(b), it can be seen that the unit cell exhibits the behavior of SNG metamaterial (ϵ-negative). The refractive index ($n = \sqrt{\mu\epsilon}$) becomes imaginary as μ and ϵ are of opposite signs. Electromagnetic waves can not propagate in such mediums and, thus, can be used for isolation enhancement in multi-port MIMO antennas by suppressing the propagation of the surface waves from one antenna to another. Gray-shaded regions in Figs. 4.3(a) and 4.3(b) indicate the operating frequency ranges of the TPCFMMA and the TPMDRA, respectively.

4.3 2-port CPW-Fed Planar Monopole MIMO Antenna Using SNG Meta-Grid Lines

4.3.1 Introduction

This part of the chapter presents a two-port CPW-fed monopole MIMO antenna (TPCFMMA). It has been observed that the TPCFMAA has mutual coupling below -20 dB for frequencies

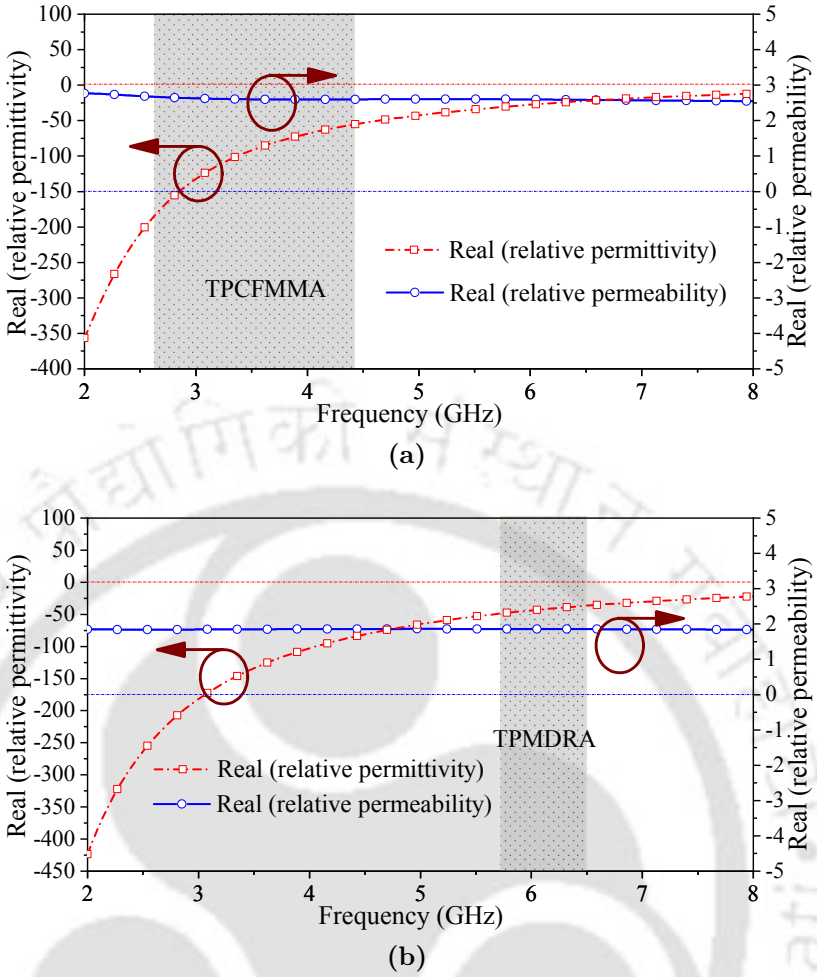

Fig. 4.3: Extracted effective permittivity and permeability of the unit cell: (a) for the TPCFMMA and (b) for the TPMDRA.

between 2.6 to 4.4 GHz. At 3.5 GHz, the inter-element distance between the antennas is noted to be $0.015\lambda_h$ (λ_h = highest operating wavelength). The TPCFMMA can be used in 3.5 GHz internet of vehicles (IoV) multi-user MIMO communication.

4.3.2 Antenna Geometry and Working Mechanism

This subsection discusses the TPCFMMA employing the SNG MGLs integrated with the ground plane for MC reduction (shown in Fig. 4.4). The top layer consists of two CPW-fed elliptical printed monopole patches, which are used as radiators, whereas the bottom layer consists of an MGL structure (5×4 unit cells). The values of all the geometrical dimensions corresponding to Fig. 4.4 are given below: $L_1 = 38.75$, $L_2 = 25$, $P = 5.35$, $R = 5$, $w = 1$, $G = 5$, $a = 4.8$, $b = 4.32$, $W_1 = 1.6$, $W_2 = 0.7$, $L_g = 4.5$, $L_3 = 3.5$, $r = a/b$. Note that all

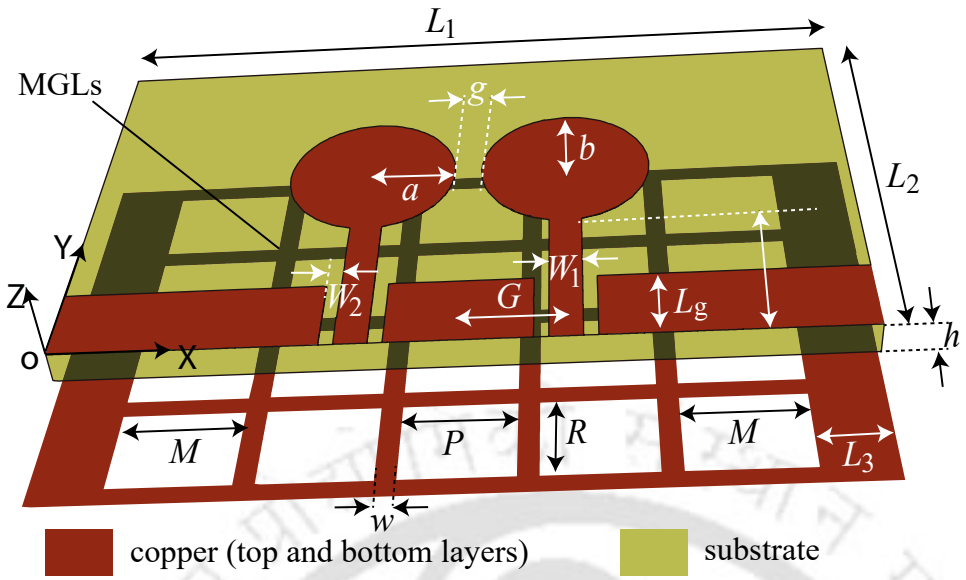

Fig. 4.4: Geometry of the 2-port CPW-fed monopole MIMO antenna.

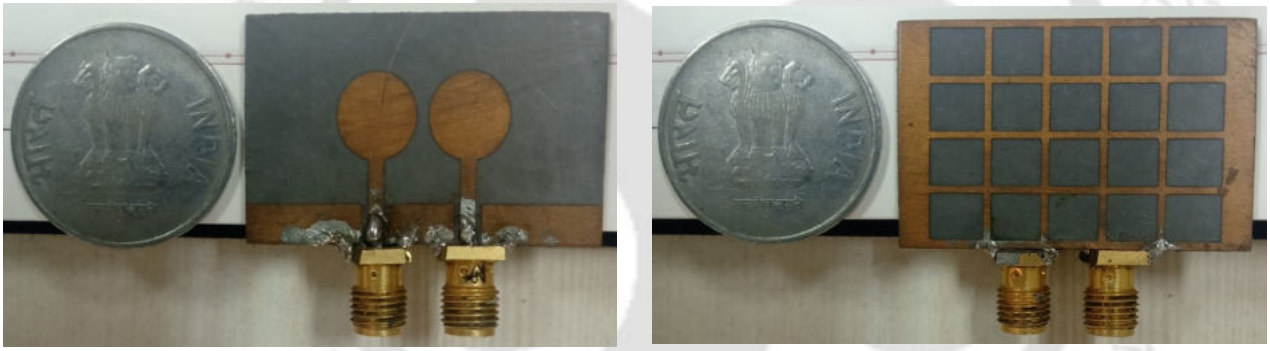

(a) **(b)**

Fig. 4.5: Fabricated prototype of 2-port CPW-fed monopole MIMO antenna: (a) top view and (b) bottom view.

values are in mm.

The photographs of the top and bottom views of the fabricated prototype of the TPCFMMA are shown in Figs. 4.5(a) and 4.5(b), respectively. All simulation results are generated using the High-frequency structure simulator (HFSS) version 14.0. To understand the contribution of the proposed MGL structure in MC reduction, the S-parameters without and with this structure are plotted in Fig. 4.6. It is apparent from these plots that the integration of the MGLs in the ground plane reduces the MC by 20 dB at 3.5 GHz. Two important design parameters

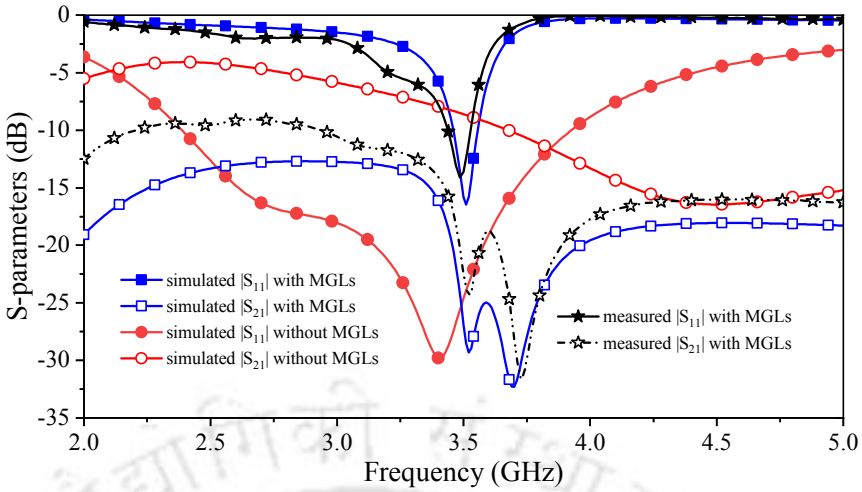

Fig. 4.6: S-parameters with and without MGLs integration in ground plane.

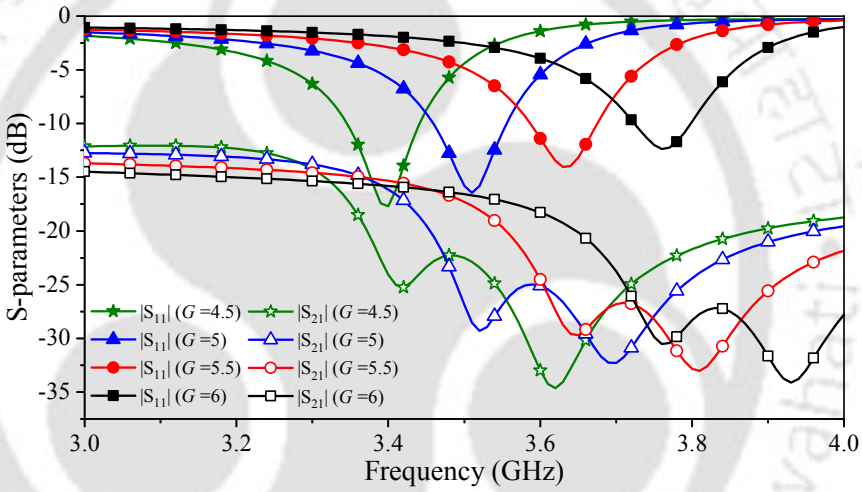

Fig. 4.7: S-parameters for different values of G.

(M and G, as shown in Fig. 4.4) are found to be vital in positioning the antenna's resonating frequency. In the case of G, as shown in Fig. 4.7, increasing or decreasing the values of G shifts the frequency upward or downward, respectively. However, in the case of M, as shown in Fig. 4.8, it is reversed, i.e., increasing or decreasing the values of M shifts the frequency downward or upward, respectively. In both cases, the MC performance remains intact. Retaining the MC performance with varied resonating frequencies is one of the novel aspects of the proposed two-port MIMO antenna. For $M = 6.85$ mm and $G = 5$ mm, the antenna can be designed for the 3.5 GHz WiMAX application. At 3.5 GHz design frequency, the electrical size of the antenna is noted to be $0.45\ \lambda_0 \times 0.30\lambda_0$.

Fig 4.9 shows the S-parameter for several combinations of M, G, and r. These combinations

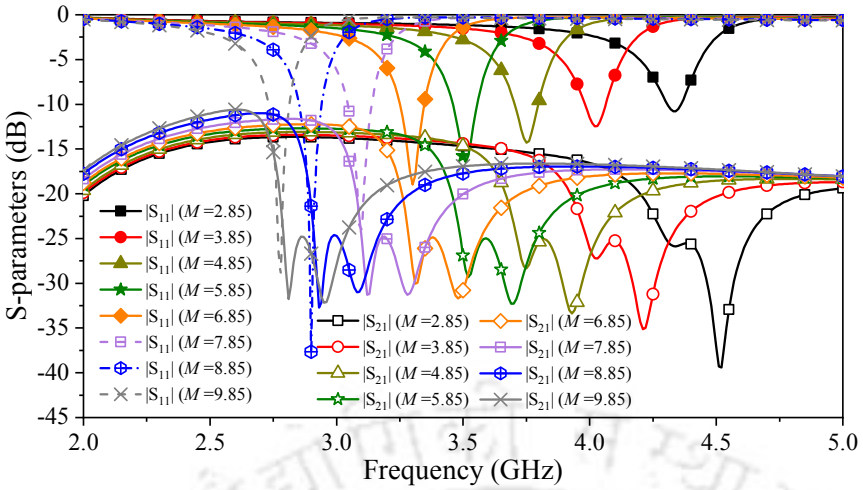

Fig. 4.8: S-parameters for different values of M.

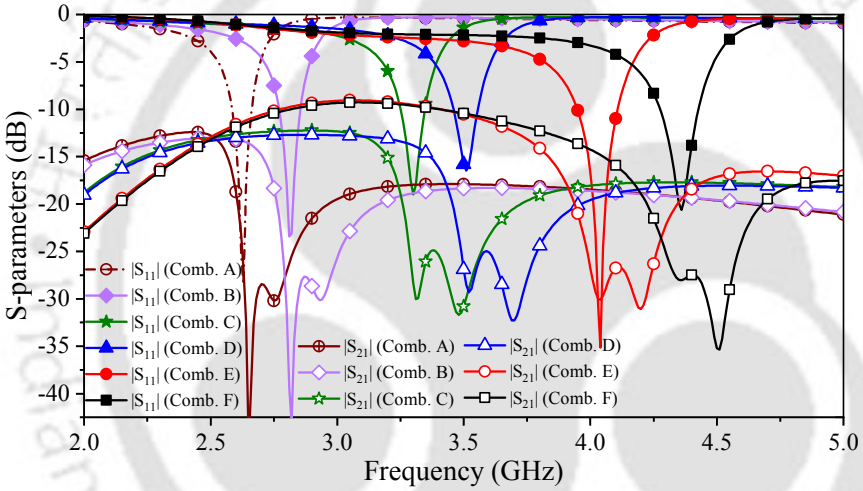

Fig. 4.9: S-parameters for several combinations of M, G, and r.

include Combination A (M = 12.85, G = 7, r = 0.9), Combination B (M = 11.85, G = 7, r = 0.9), Combination C (M = 9.85, G = 5, r = 0.9), Combination D (M = 5.85, G = 5, r = 0.9), Combination E (M = 3.85, G = 5, r = 0.3), and Combination F (M = 2.85, G = 5, r = 0.3). Note that all values are in mm. By selecting the proper combination of these parameters, an optimal mutual coupling performance can be obtained, and the antenna can be designed to resonate at any frequency between 2.6 and 4.4 GHz. For example, a mutual coupling of close to -45 dB can be achieved using Combination B. For Combination A, the MC is below -17.27 dB, while for the rest of the combinations, the MC is noted to be below -20 dB.

The performance comparison of the TPCFMMA with other works is shown in Table 4.1. It is noticed that the proposed TPCFMMA has the minimum inter-element spacing (in terms

Table 4.1: Comparison of the proposed TPCFMMA with other EBG, MTM, MS and DB based two-port antenna designs.

Refs.	BW	A_S	ML	EH	I_S
[29]	5.75 center frequency, bandwidth not mentioned	1.50×1.50×0.049	Yes	1.27 mm	$0.5\lambda_h$
[30]	4.85-5.08	0.87×0.43×0.024	No	0.00 mm	$0.13\lambda_h$
[32]	8.7-11.7, 11.9-14.6, 15.6-17.1, 22-26, 29-34.2	1.07×2.03×0.046	No	0.00 mm	$0.58\lambda_h$
[48]	2.5-2.7, 3.4-3.6	0.83×1.25×0.14	Yes	11 mm	$0.008\lambda_h$
[49]	3.3-3.7	1.1×1.1×0.385	Yes	35 mm	$0.264\lambda_h$
[51]	3.3 to 3.34	1.6×0.9×0.16	Yes	14.3 mm	$0.12\lambda_h$
[52]	4.6-5.29	1.53×0.92×0.38	Yes	16.5 mm	$0.092\lambda_h$
Prop.	3.46-3.56	0.28×0.45×0.018	No	No extra height	$0.015\lambda_h$

Abbreviations: Refs.: references, BW: impedance bandwidth (GHz), λ_h: highest operating wavelength, A_S: antenna size (in λ_h^3), ML: multi-layer arrangement, EH: excess height, I_S: inter-element spacing (edge-to-edge in λ_h), Prop.: proposed work.

of λ_h) except for the MIMO antenna in [48]. But, the antenna in [48] occupies 64 times more volume (in λ_h^3) than the TPCFMMA. The TPCFMMA has broader percentage bandwidth than the antenna of [51] and comparable percentage bandwidth with the antenna in [29] but lesser percentage bandwidth than the antennas in [30], [32], [48], [49], and [52]. However, excellent bandwidth improvement is seen in the TPMDRA employing meta-grid lines in the ground plane for MC reduction, and it will be covered in the next section. The TPCFMMA is a very low profile antenna that occupies 48.6, 3.95, 44, 64, 205, 101.6, and 236 times lower volume than the antennas of [29], [30], [32], [48], [49], [51], and [52], respectively. The elements of this highly compact MIMO antenna satisfy the criterion ($ka < 1$) for electrically small antennas [85]. Furthermore, the TPCFMMA design is simple, compact, and especially does not have a multi-layer arrangement contrary to the antennas of [29], [48], [49], [51], and [52] that add extra heights to these antennas.

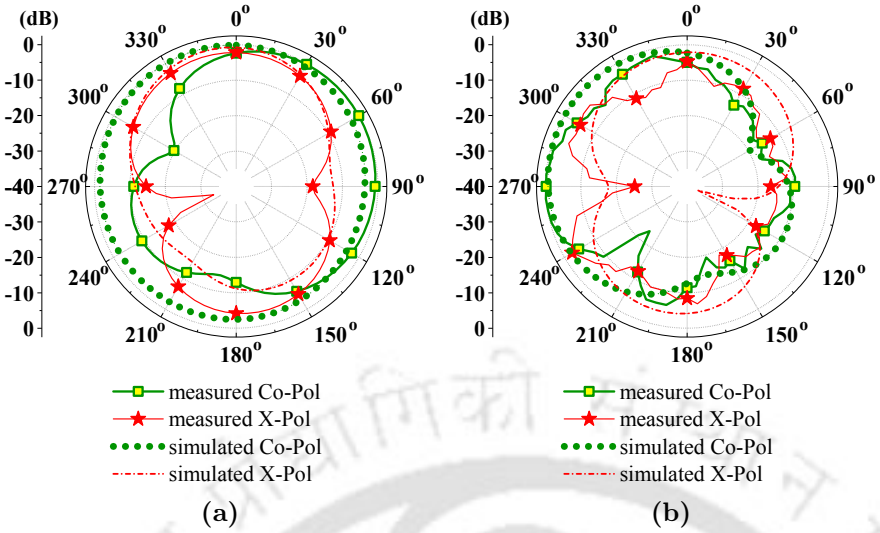

Fig. 4.10: Radiation patterns at 3.5 GHz: (a) $\phi = 0^0$ plane and (b) $\phi = 90^0$ plane.

4.3.3 Antenna Performance

The measured S-parameters with their simulated values are shown in Fig. 4.6. A good agreement has been seen between the simulated and the measured S-parameters.

Normalized radiation patterns at 3.5 GHz (for Combination D) in $\phi = 0^0$ and $\phi = 90^0$ planes are plotted in Fig. 4.10. The peak gain is noted to be lying from 1.53 to 1.68 dBi within the antenna bandwidth from 3.46 to 3.56 GHz (Fig. 4.11). It can be observed that the measured gain slightly deviates from the simulated gain, which may be due to fabrication tolerances.

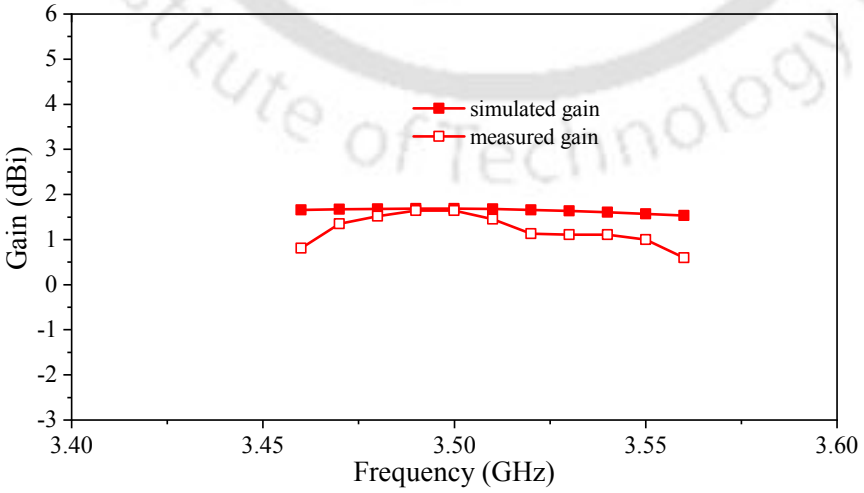

Fig. 4.11: Measured and simulated gain of the TPCFMMA.

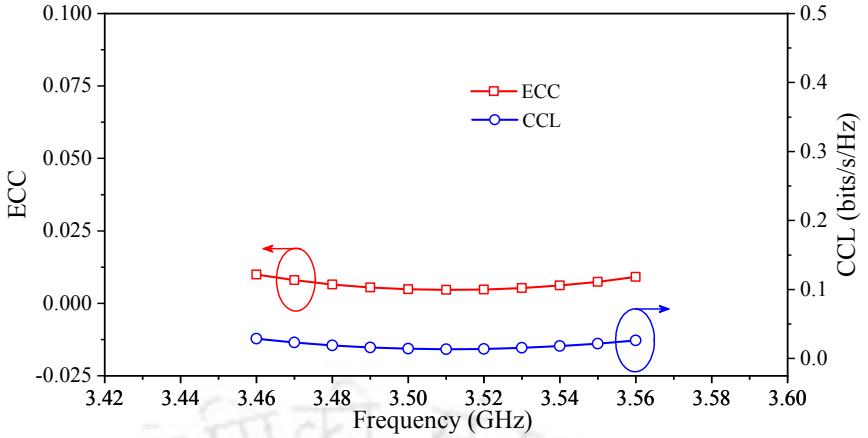

Fig. 4.12: ECC and CCL versus frequency.

The ECC is calculated using (1.12) and (1.13) from chapter 1 and is plotted in Fig. 4.12. The ECC for this dual-port MIMO antenna is noted to be less than 0.0099. The correlation among antennas causes a loss in the channel capacity of a MIMO system. Based on the assumption that this MIMO antenna is used at both transmitter and receiver sides to realize a 2×2 MIMO communication system. The CCL for such a MIMO system due to the correlation is calculated using (1.24) from chapter 1 and plotted in Fig. 4.12. The CCL for this MIMO system is noted to be less than 0.028 bits/s/Hz.

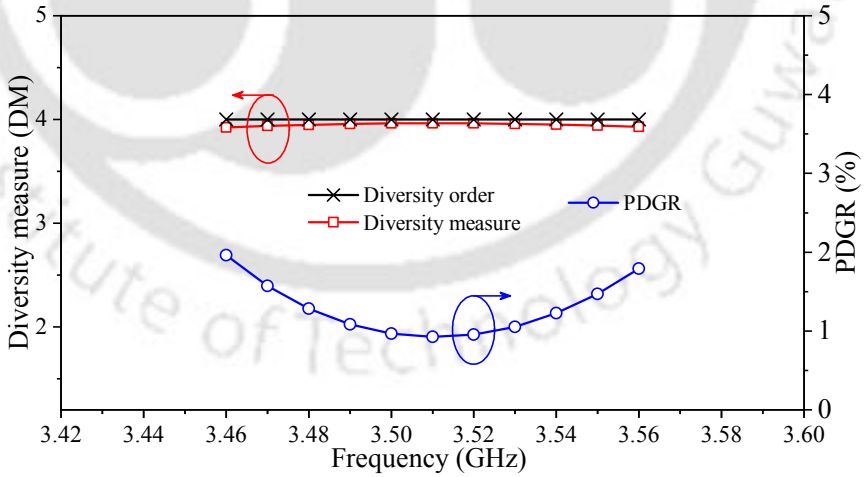

Fig. 4.13: DM and PDGR versus frequency.

Using (1.18), the DO for the above-described 2×2 MIMO system is four across the antenna bandwidth. The DM is calculated using (1.19) and plotted along with the DO in Fig. 4.13. The percentage diversity gain reduction (PDGR) is a parameter that measures the reduction

in the diversity performance of a MIMO antenna due to the correlation between antennas. The PDGR versus frequency curve is plotted in Fig 4.13 and is noted to be less than 1.96 %.

In a multi-user MIMO scenario, the channel capacity loss is measured as sum rate loss (SRL) and calculated using (1.25). Three mobile terminals (each having this two-port antenna) are considered for the SRL analysis in accordance with Fig. 1.11 of chapter 1. The SRL for this MIMO antenna at the center frequency (3.51 GHz) is 0.0160×10^{-14} bits/s/Hz.

Considering the practical deployment of this antenna, the effect of the large ground plane on antenna performance is analyzed. The simulation with an extended ground plane (50 mm in the +Y axis, +X axis and -X axis directions as per Fig. 4.4) in the plane containing the bottom layer of the antenna is carried out. It is noted that the cross-polarization discrimination (XPD) performance and antenna gain both improve with the usage of the extended ground plane. Another simulation is carried out with a large ground plane (50 mm in the +Y axis, +X axis and -X axis directions as per Fig. 4.4), which is placed 10 mm below the plane containing the bottom layer of the TPCFMMA. It is seen that the gain improves from 1.65 dBi to 2.91 dBi. However, the XPD does not improve. In both cases, impedance matching and isolation performances remain almost unaffected.

The TPCFMMA can be mounted over a vehicle's roof-top, utilizing the large metallic roof layer of the vehicle as an extended large ground plane or as a reflector below the antenna. Therefore, this antenna can be used for the 3.5 GHz internet of vehicles (IoV) multi-user MIMO service.

4.4 2-Port MIMO DRA using SNG Meta-Grid Lines

4.4.1 Introduction

This section of the chapter presents a two-port MIMO DRA (TPMDRA). A patch with annular ring-shaped slots is used for exciting each DRA. It is noted that the TPMDRA's operating frequency can be tuned by changing the parameters of the annular ring slot in the excitation patch. For low MC, MGLs, as explained in section 4.2 of this chapter, are integrated into the ground plane. The bandwidth of the TPDRAA can be further increased by merging the two resonances. For the TPDRAA, the measured -10 dB impedance bandwidth is from 5.65 to 6.55 GHz. The mutual coupling between the antenna elements is seen to be below -16 dB for an

inter-element spacing of 4.8 mm, which is $0.090\lambda_h$. The measured gain of the TPMDRA within the bandwidth is from 4.17 to 5.2 dBi. The TPMDRA can be used for satellite communication in the 5.925 to 6.425 GHz frequency band, WiMAX in the 5.7 to 5.85 GHz band, ISM in the 5.725 to 5.85 GHz band, and WLAN in the 5.8 GHz band.

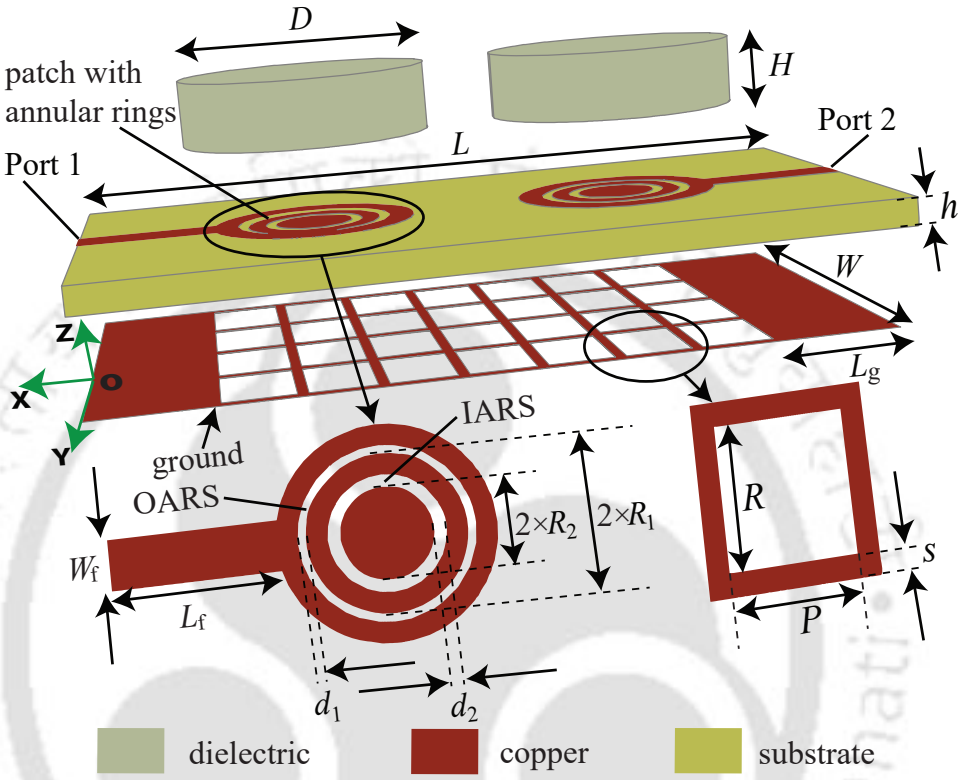

Fig. 4.14: Antenna geometry of the 2-port MIMO DRA.

4.4.2 Antenna Geometry and Working Mechanism

The isometric view of the antenna is shown in Fig. 4.14. It uses two CDRA blocks of $\epsilon_r = 25$ as radiating elements. These dielectric blocks are excited by means of two concentric annular rings in the circular patches placed above the substrate (Rogers RT-Duroid 5870 with $\epsilon_r = 2.33$ and $\tan(\delta) = 0.0012$). These circular patches are connected to the microstrip line that feeds signals to the antenna elements. The ground plane (in maroon) has an MGL structure (7×4 unit cells) integrated between two uniform rectangular sections of dimensions $L_g \times W$ at its two ends. The values of all the geometrical parameters are as follows: $D = 14.4$, $H = 3.8$, $L = 45$, $W = 25$, $L_g = 7.2$, $W_f = 2.4$, $L_f = 7.7$, $R_1 = 3.8$, $R_2 = 2.2$, $P = 3.37$, $R = 5$, $d_1 = 0.4$, $d_2 = 0.6$, $s = 1$, $h = 1.57$. All dimensions are in mm.

Using (4.1) and (4.2) from [8], the resonating frequency of the circular patch of radius a = 5.2 mm is calculated to be 9.8 GHz which is much higher than the frequency range of the proposed antenna. Therefore, it is concluded that the non-radiating patches with annular ring slots are used for exciting the $HEM_{12\delta}$ mode in the cylindrical dielectric blocks.

$$F = \frac{8.791 \times 10^9}{f_r \times \sqrt{\epsilon_r}} \tag{4.1}$$

$$a = \frac{F}{\sqrt{1 + \frac{2h}{\epsilon_r \pi F}(\log_e(\frac{\pi F}{2h} + 1.7726))}} \tag{4.2}$$

Here, h and a are in cm and f_r is the resonant frequency of the circular patch.

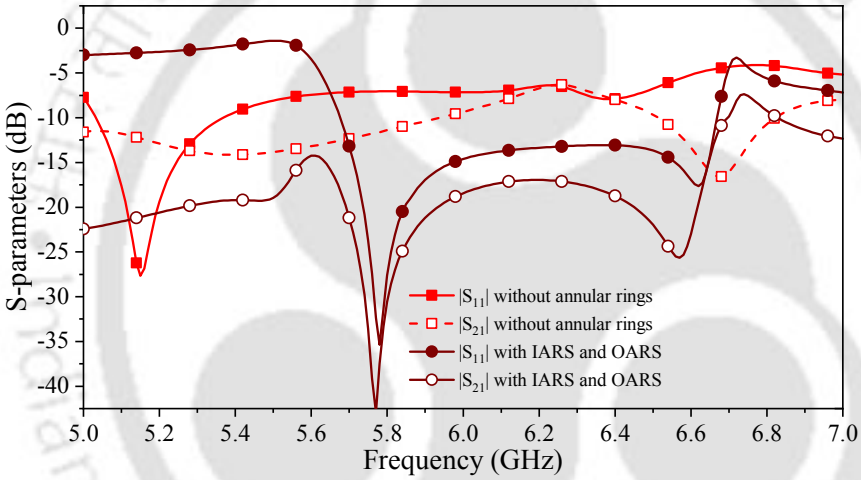

Fig. 4.15: S-parameters without and with both annular rings.

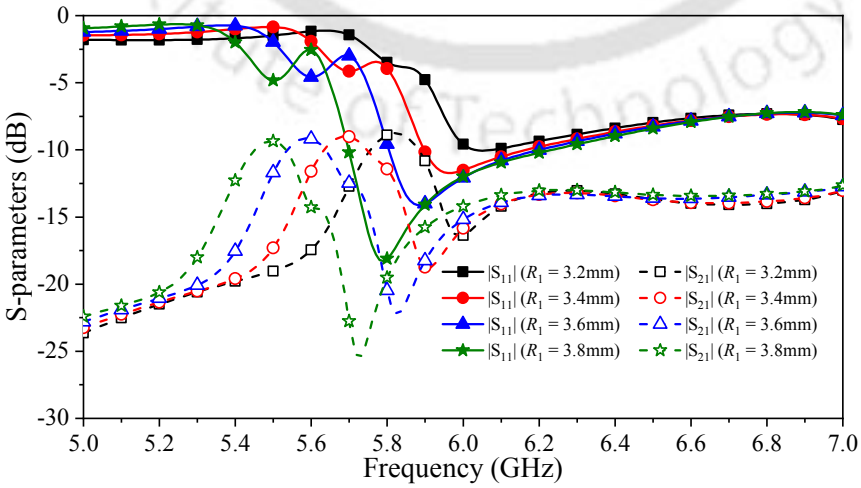

Fig. 4.16: S-parameters for different radii of the OARS.

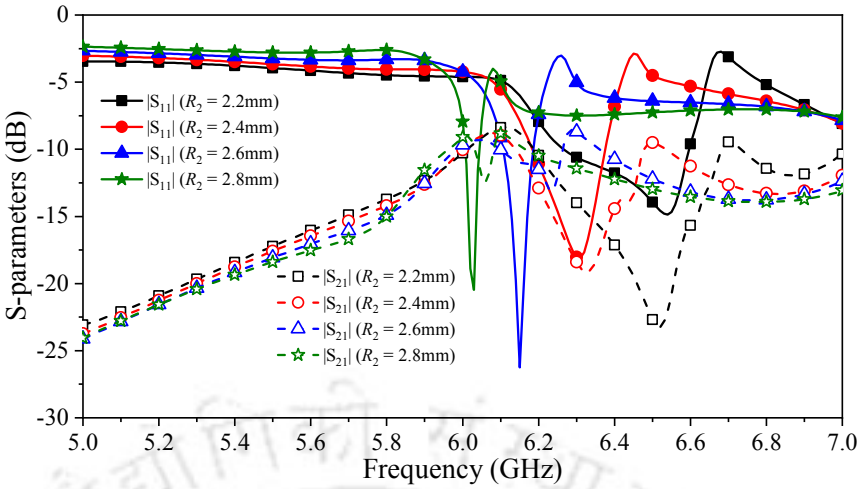

Fig. 4.17: S-parameters for different radii of the IARS.

The antenna configuration without the annular ring-shaped slots has small bandwidth (refer to Fig. 4.15). Therefore, attempts are made to increase the bandwidth by employing the annular slots in the circular patches, which excite the DRA blocks. Note that the initial radius of the slot is chosen such that the annular ring slot length (perimeter) = $\lambda_0/2$. For 6 GHz frequency, $\lambda_0/2 = 50$ mm and $\lambda_g = 32.75$ mm. Hence, $(\lambda_g/2) = 16.37$ mm. The radius for the circular annular ring slot with a perimeter of 16.37 mm comes out to be 2.6 mm. Hence, variations have been made around this initially calculated dimension to chose the radii of annular ring slots for bandwidth enhancement. Here, λ_0 and λ_g are the free space and guided wavelengths, respectively.

It is shown in [86] that increasing the radius of the feeding slot decreases the resonating frequency and vice-versa. A similar trend can be observed in the S-parameters of the antenna, with only the outer annular ring slot (OARS) and only the inner annular ring slot (IARS). The same can be seen in Figs. 4.16 and 4.17, which show the S-parameters for different radius values of the OARS and IARS, respectively. It has been observed that by varying the radius of the OARS and the IARS, the resonance can be adjusted in the lower and higher frequency regions, respectively. The above discussion implies that the lower resonance at 5.78 GHz and the higher resonance at 6.5 GHz in Fig. 4.15 are due to the OARS and IARS, respectively. These two resonances merge when the IARS ($R_2 = 2.2$ mm) and the OARS ($R_1 = 3.8$ mm) are used together, leading to a broader bandwidth from 5.68 GHz to 6.7 GHz.

The dimensions of the circular dielectric block to excite the $HEM_{12\delta}$ mode at 5.8 GHz are

calculated using (4.3) from [87] and turn out to be $H = 3.8$ mm and $D = 14.4$ mm.

$$f(GHz) = \frac{30\mathrm{k}_0 a}{2\pi a(cm)} \tag{4.3}$$

where,

$$\mathrm{k}_0 a = \frac{3.72 + 0.4464x + 0.2232x^2 + 0.0521x^3 - 2.65\exp^{-N}}{\sqrt{\epsilon_r}},$$

$a = \frac{D}{2}$, $x = \frac{a}{2H}$ and $N = 1.25x(1 + 4.7x)$, f is the resonating frequency and ϵ_r is the relative permittivity of the dielectric material.

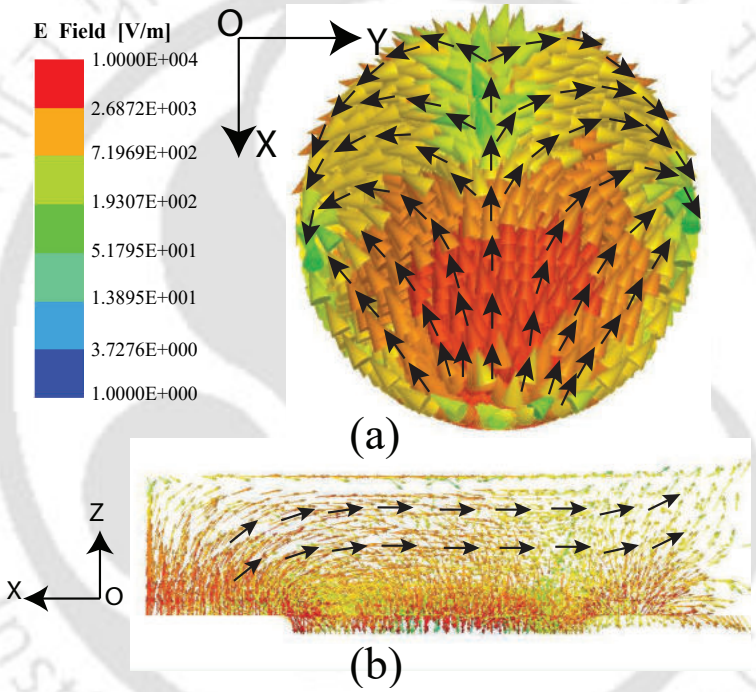

Fig. 4.18: Electric field distribution at 5.78 GHz: (a) top and (b) side view.

Fig. 4.16 shows that the mutual coupling curves have valleys just below the resonance for the OARS, and the same is observed for the IARS in Fig. 4.17. It is mainly because of the integration of the MGLs in the ground plane.

Electric field patterns at 5.78 GHz are shown in Fig. 4.18 and confirm the excitation of $\mathrm{HEM}_{12\delta}$ mode [88].

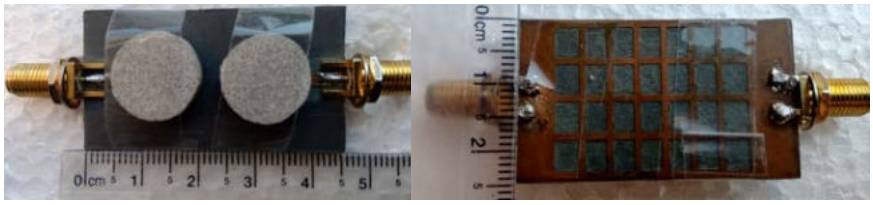

Fig. 4.19: Fabricated antenna prototype (top and bottom views).

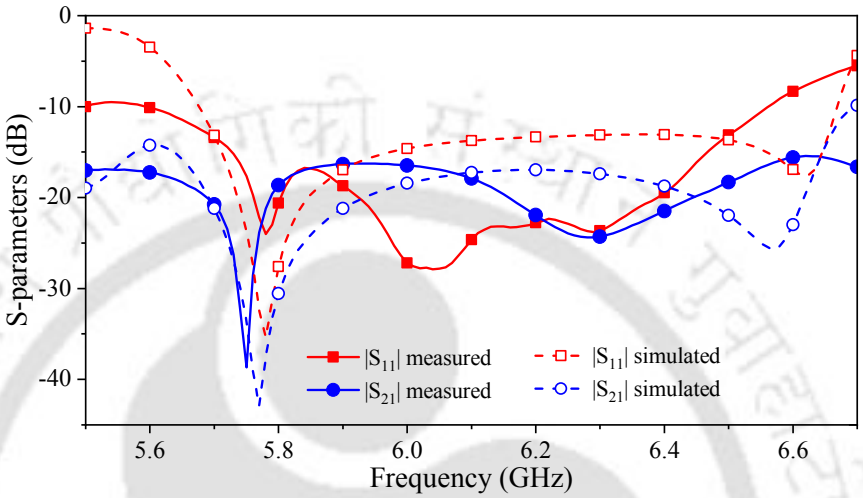

Fig. 4.20: Measured and simulated S-parameters.

4.4.3 Antenna Performance

The simulated and measured S-parameters of the fabricated prototype (as depicted in Fig. 4.19) are plotted in Fig. 4.20. The measured -10 dB impedance bandwidth of the antenna is observed from 5.65 to 6.55 GHz, and the simulated bandwidth is from 5.68 to 6.7 GHz. The slight difference in the measured and simulated bandwidth is because of various tolerances, such as imperfections in cutting the DRA block and PCB fabrication. The measured isolation between the antenna elements is found to be more than 16 dB for the entire bandwidth, with a maximum value of 38.6 dB.

The measured and simulated co-polar and cross-polar radiation patterns for $\phi = 0^0$ and $\phi = 90^0$ planes at 5.8 GHz are plotted in Fig. 4.21. During pattern measurements, port 1 is excited, whereas port 2 is terminated with a matched load. The measured cross-polarization discrimination (XPD) value in the broadside direction is more than 11.5 dB in both planes. The difference in the XPD value between the simulated and measured data could be due to the detector sensitivity. The measured and the simulated peak gain with respect to frequency

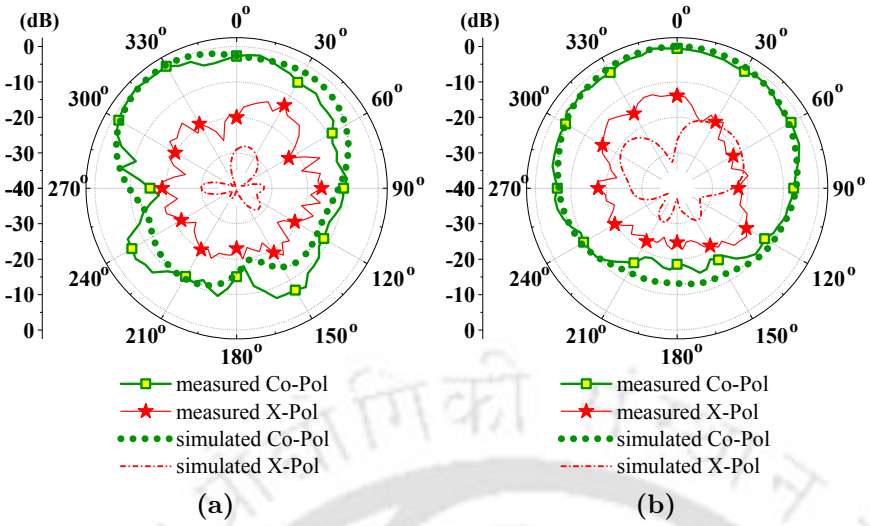

Fig. 4.21: Radiation patterns: (a) $\phi = 0^0$ plane and (b) $\phi = 90^0$ plane.

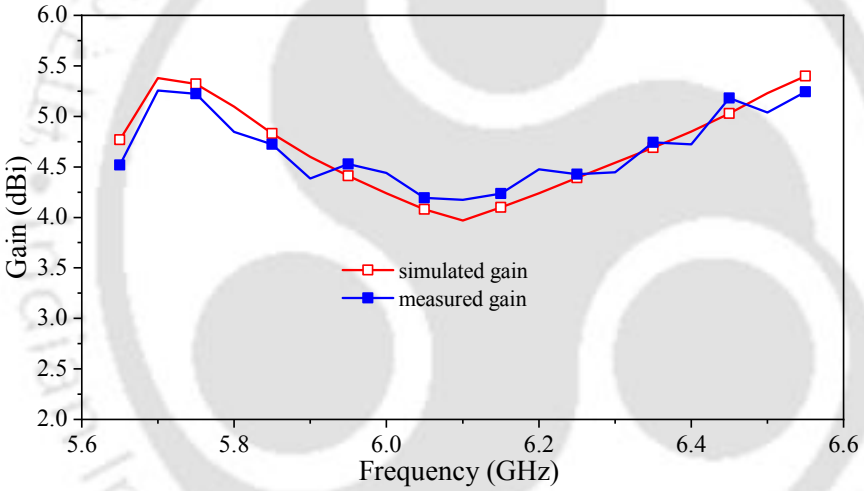

Fig. 4.22: Measured and simulated gain.

are plotted in Fig. 4.22. The measured antenna gain ranges from 4.17 to 5.2 dBi, while the simulated gain lies between 3.97 to 5.4 dBi.

The ECC is calculated using (1.12) and (1.13) from chapter 1 and is plotted in Fig. 4.23. The ECC for the TPMDRA is noted to be less than 0.04 from 5.78 to 6.58 GHz. The correlation among antennas causes the loss in the channel capacity. Considering this MIMO antenna deployed on the transmitter and receiver sides of a 2×2 MIMO system, the channel capacity loss due to the correlation can be calculated using (1.24) from chapter 1 and is plotted in Fig. 4.23. The CCL for this MIMO system is noted to be less than 0.118 bits/s/Hz from 5.78 to 6.58 GHz.

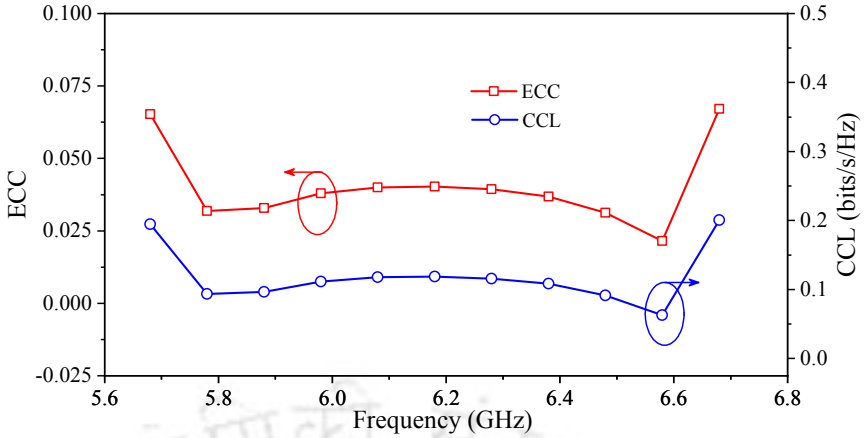

Fig. 4.23: ECC and CCL versus frequency.

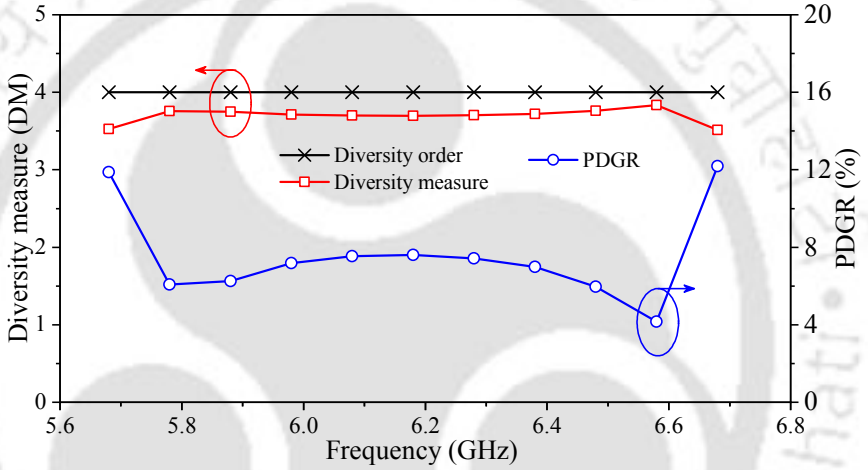

Fig. 4.24: DM and PDGR versus frequency.

Using (1.18), the DO for the above-described 2×2 MIMO system is four across the antenna bandwidth. The DM is calculated using (1.19) and plotted along with the DO in Fig. 4.24. The PDGR is a measure of the reduction in the diversity performance of a MIMO antenna due to antenna correlation and is plotted in Fig 4.24. The PDGR value is noted to be less than 6.18 % from 5.78 to 6.58 GHz.

The comparison of the proposed work (TPMDRA) with other contemporary works is listed in Table 4.2. It has been observed that MIMO antennas in [67], [69], [70], and [71] occupy 3.1, 34.8, 23, and 6.1 times more volumes than the TPMDRA, respectively. Moreover, the TPMDRA has the highest percentage bandwidth and the lowest inter-element spacing (in terms of λ_h).

Table 4.2: Comparison of the proposed work with other works.

Refs.	BW	A_S	N_P	I_S
[67]	5.25-5.92	1.05×0.7×0.15	3	$0.298\lambda_h$
[69]	9.04-9.92	1.7×1.7×0.424	3	Not applicable
[70]	27.25-28.35	1.8×1.8×0.25	2	$0.117\lambda_h$
[71]	25.2-27.1	1.8×0.92×0.13	2	$0.11\lambda_h$
Prop.	5.65- 6.55	0.84×0.46×0.091	2	$0.091\lambda_h$

Abbreviations: Refs.: references, BW: impedance bandwidth (GHz), λ_h: highest operating wavelength, A_S: antenna size (in λ_h^3), N_P: number of ports, I_S: inter-element spacing (edge-to-edge in λ_h), Prop.: proposed work.

4.5 Conclusions

In this chapter, meta-grid lines are integrated into the ground plane to reduce the MC in a TPCFMMA. This technique is further extended for the same objective in the case of a TPMDRA as well. The proposed MC reduction approach does not add any extra footprint to the presented MIMO antennas. The TPCFMMA and TPMDRA are fabricated and tested as proofs-of-concept. For the TPCFMMA, at 3.51 GHz center frequency (bandwidth from 3.46 to 3.56 GHz), the MC is -28 dB. The ECC is noted to be less than 0.0099, and the CCL is found below 0.028 bits/s/Hz within the operating bandwidth. The PDGR is found below 1.96%. The SRL for this MIMO antenna at the center frequency (3.51 GHz) is 0.0160×10^{-14} bits/s/Hz. Therefore, the TPCFMMA is a suitable candidate for the 2-port MIMO WiMAX application. The MC in the TPMDRA is noted to be less than -16 dB within the operating frequency range. The ECC is noted to be less than 0.04, and the CCL is found below 0.118 bits/s/Hz from 5.78 to 6.58 GHz. The PDGR is found below 6.18%. Thus, making this compact TPMDRA a suitable candidate for MIMO application in the operating frequency range (5.78 to 6.58 GHz) that covers 5.925 to 6.425 GHz frequency band for satellite communication, 5.7 to 5.85 GHz for WiMAX, 5.725 to 5.85 GHz for ISM band, and 5.8 GHz for WLAN application.

5

Double-Side Copper Cladded Substrate for Mutual Coupling Reduction in Miniaturized DRAs

This chapter presents a technique that uses a double-side copper cladded substrate for reducing the mutual coupling between two half-split cylindrical DRAs. This approach helps to realize a closely packed MIMO antenna with small edge-to-edge inter-element spacing and low electromagnetic interaction between antenna elements with simultaneous miniaturization of the DRA with an overall reduction of MIMO antenna size.

5.1 Introduction

This chapter presents a method for reducing the mutual coupling in the E-plane between two tightly-spaced and reduced-size DRA elements. E-plane coupling within closely spaced antennas introduces strong mutual coupling and has been rarely addressed in the literature. The proposed design is presented with a four-fold objective: (i) small inter-element spacing, (ii) good isolation, (iii) miniaturized DRAs, and (vi) reduced overall antenna size. A double-side copper-cladded substrate is inserted between two half-split cylindrical DRAs (CDRAs), offering a close to 50% reduction in the DRA's size. It also helps to reduce the mutual coupling by reducing the mutual impedance between the ports. The mutual impedance is tuned to a minimal value, precisely at resonance, by varying the substrate thickness. This approach has been analyzed and verified further by demonstrating an equivalent circuit model of this two-port DRA. The proposed concept is a simple and efficient way of reducing the mutual coupling. This approach fulfills the requirements of modern MIMO communication by realizing a compact antenna system. All results are systematically presented based on simulation studies and validated experimentally using a fabricated prototype.

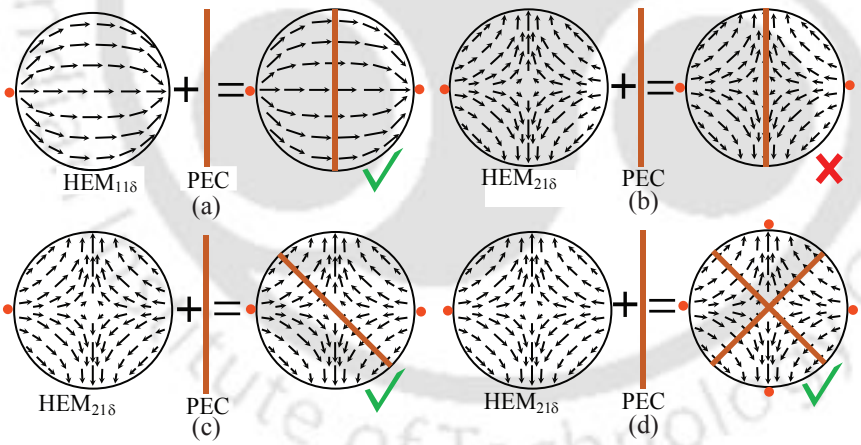

Fig. 5.1: E-field distribution of the first two radiating modes of a CDRA with the possibility of splitting into halves or quarters using the PEC boundary: (a) possible for $HEM_{11\delta}$ mode with straight PEC boundary, (b) not possible for $HEM_{21\delta}$ mode with straight PEC boundary, (c) possible for $HEM_{21\delta}$ mode with 45^0 titled PEC boundary, and (d) possible for $HEM_{21\delta}$ mode to break into 4-quarters with two tilted PEC boundaries at 45^0 and 135^0.

5.2 Proposed Concept and Antenna Design

This section presents a systematic design strategy for reducing the mutual coupling between two half-split CDRAs. It begins with a coaxial-fed CDRA of radius (r_d) = height (h_d) = 10 mm with ϵ_{dra} = 10. Its resonating frequency for the dominant HEM$_{11\delta}$ mode is estimated as 3.96 GHz using (5.1) [53].

$$f_r = \frac{4.7713 \times k_0 a}{a} \tag{5.1}$$

where

$$k_0 a = \frac{6.324}{\sqrt{2+\epsilon_r}}(0.27 + 0.36(\frac{a}{2h}) + 0.02(\frac{a}{2h})^2)$$

Here, h and a are in cm, and f_r is the resonant frequency in GHz.

Fig. 5.1 depicts the E-field distributions for the first two radiating modes of CDRA with the possibility of splitting into halves or quarters by inserting vertical PEC boundary without affecting the E-field distribution. As evident from Fig. 5.1(a), splitting into two halves is possible in the case of HEM$_{11\delta}$ mode. In contrast, with the same location of the PEC wall, this is not the case with the higher-order HEM$_{21\delta}$ mode, as shown in Fig. 5.1(b). This higher-order mode is expected to be suppressed due to the placement of a vertical metal sheet. However, if the metal sheet becomes tilted by 45^0, the HEM$_{21\delta}$ mode is supported (as shown in Fig. 5.1(c)), and the HEM$_{11\delta}$ mode is suppressed. Also, if another metal sheet tilted by 135^0 is inserted, the CDRA can be split into 4-quarters, as shown in Fig. 5.1(d).

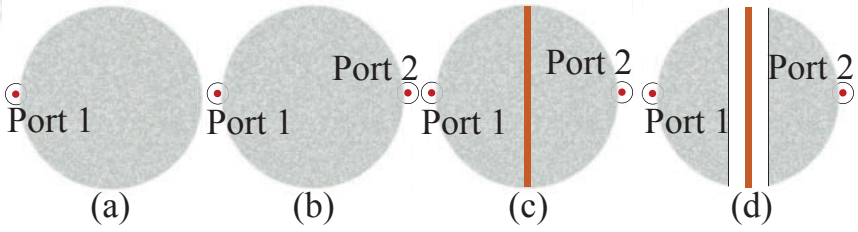

Fig. 5.2: Evolution of various antenna configurations: (a) A_1: conventional CDRA with single port, (b) A_2: CDRA with two ports, (c) A_3: two-port half-split CDRAs with inserted metal sheet, and (d) A_4: two-port half-split CDRAs with metal sheet and air gaps.

Fig. 5.2 illustrates various excitation options of a CDRA — antenna configurations using a single probe (A_1) and its design evolution using dual probes (A_2, A_3, and A_4). The conventional configuration A_1 excites HEM$_{11\delta}$ mode dominantly. A_2 excites better HEM$_{11\delta}$ mode when the

two ports are out of phase. However, when the two ports are in phase, the $HEM_{21\delta}$ mode is excited, and the $HEM_{11\delta}$ mode is suppressed. Let us concentrate on the $HEM_{11\delta}$ mode case.

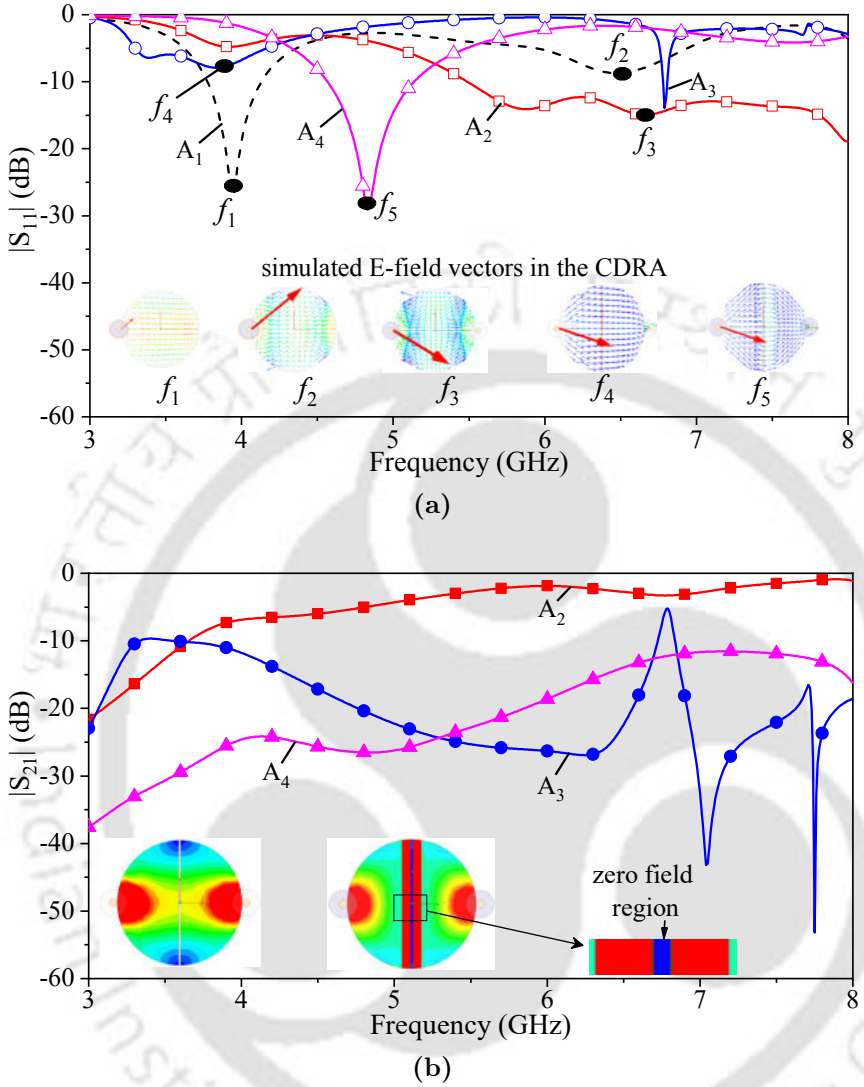

Fig. 5.3: S-parameters for various antenna stages: (a) $|S_{11}|$ and (b) $|S_{21}|$.

In the dual port configuration, a metal sheet with and without the air gap is also incorporated to investigate their effect on the resonance and the mutual coupling characteristics. The insertion of the metal sheet makes it possible to have two independent excitations with low mutual coupling using coaxial probes at the opposite ends of the CDRA. It appears to be a suitable design approach to realize a compact MIMO antenna with suppressed mutual coupling. The $|S_{11}|$ characteristics of all antenna variants are plotted in Fig 5.3(a). The curve corresponding to A_1, representing a coax-fed CDRA with a single port, exhibits resonances at 3.95 and 6.5 GHz, indicating the excitation of the $HEM_{11\delta}$ and $HEM_{21\delta}$ modes, respectively [89]. This is evident

from the E-field distributions of the CDRA shown in the inset of Fig. 5.3(a), at frequency points f_1 and f_2 on the $|S_{11}|$ curve for A_1. However, configuration A_2 with two ports (in phase) suppresses the $HEM_{11\delta}$ and supports $HEM_{21\delta}$ mode that resonates near 6.5 GHz (f_3). E-field distribution at frequency point f_3 confirms this. Configuration A_2 has a strong mutual coupling between its ports, as evident from Fig. 5.3(b). It is possible to restore the dominant $HEM_{11\delta}$ mode and reduce mutual coupling in configuration A_3 with a reduced size DRA [89]. Note that configuration A_3 is realized from A_2 by introducing a metal sheet of the same height as the half-split CDRA. The electric field portrayal of A_3, shown in Fig. 5.3(a), also confirms the excitation of $HEM_{11\delta}$ mode at frequency point f_4. The poor impedance matching performance of A_3 near its first resonance is significantly improved by incorporating two air gaps beside the metal sheet in A_4. The electric field distribution of A_4 at point f_5 is shown in Fig. 5.3(a) and is found to be similar to that of the $HEM_{11\delta}$ mode. This strategy further suppresses the mutual coupling, as shown in Fig. 5.3(b). However, there is a slight shift in resonance towards the higher side. This occurs due to the perturbation of the CDRA and the inclusion of air gaps. It should also be stated that the air gap will reduce the effective permittivity of the split DRA as explained in [90–92]. This reduction of the effective permittivity causes a reduction of the resonator Q-factor and, in turn, an increase in the antenna bandwidth.

Based on this concept, a vertical double-side copper-cladded substrate between two half-split CDRA elements changes the edge impedance to be high because it acts as a parallel plate transmission line shorted at the ground plane end. When the height of the substrate is close to a dielectric quarter wavelength, the impedance seen at the top of the substrate is very high (open circuit), forcing the normal electric field to the edge to be zero. Thus, eventually creating an almost zero field region and increasing the isolation significantly. Secondly, the air gaps between the metal plates and half-split DRAs have been created. These air gaps improve the impedance matching performance. The mutual coupling between the ports may be improved further by controlling the substrate thickness. In this proposed technique, the lower order fundamental mode ($HEM_{11\delta}$) is excited with size miniaturization, but there is a slight upward shift in its resonating frequency. The final antenna configuration is depicted in Fig. 5.4. The proposed two-port antenna consists of two perturbed half-split dielectric blocks ($\epsilon_{dra} = 10$), which are created by cutting it along the diameter of the cylindrical dielectric block. In the air gap region, an FR-4 sheet (both sides copper cladding) is placed between DRA 1 and DRA 2. This sheet

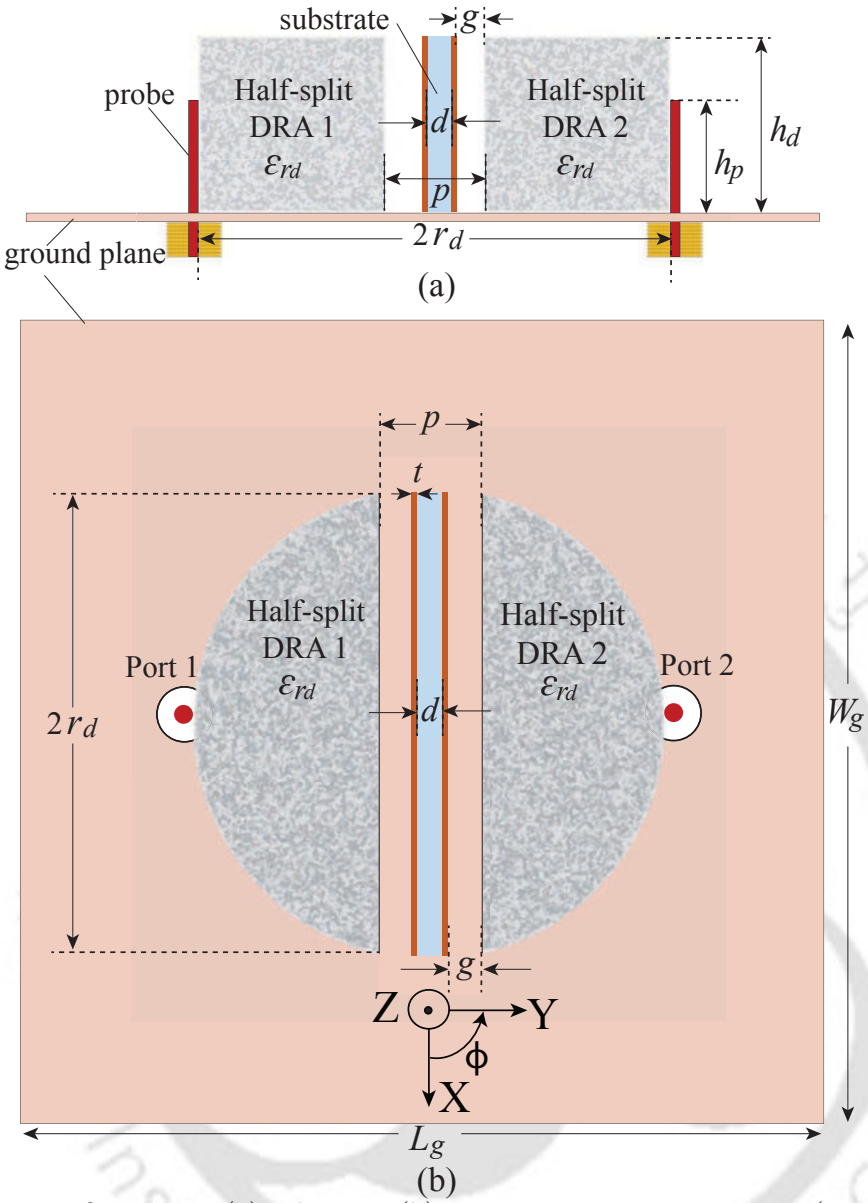

Fig. 5.4: Antenna configuration: (a) side view, (b) top view. Design parameters (in mm): $L_g = W_g = 50,\ r_d = 10,\ h_d = 10,\ h_p = 6.6,\ p = 3,\ d = 0.8,\ g = 1.065$.

has a thickness (d) of 0.8 mm and ϵ_r of 4.4. The size of the ground plane is 50 mm × 50 mm.

The S-parameters for various values of d are plotted in Fig. 5.5(a). It is noted that for a particular value of d, the mutual coupling at the resonant frequency reduced significantly compared to the mutual coupling of A_4 (refer to Figs. 5.3(b) and 5.5(a)). This is because the copper-cladded FR-4 sheet primarily functions as a parallel plate capacitor (C_p). Therefore, the mutual impedance between antenna ports changes by varying its thickness. For a particular value of d, the mutual impedance can be brought to near zero. The same is depicted in Fig. 5.5(b). The S-parameters for different values of p for a fixed value of d = 0.8 mm are plotted

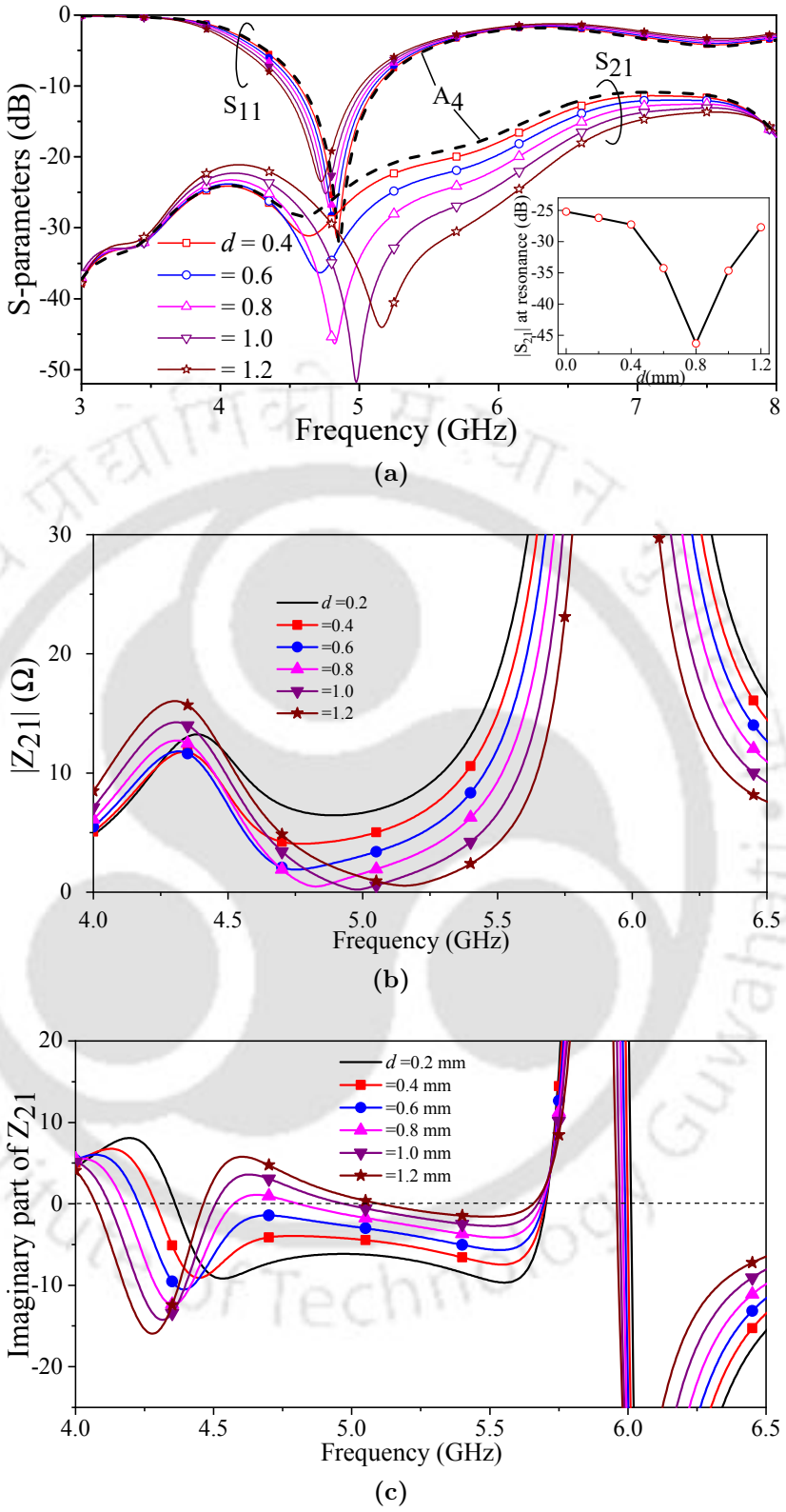

Fig. 5.5: Parametric study for different values of d (in mm): (a) S-parameters, (b) magnitude of mutual impedance ($|Z_{21}|$), and (c) imaginary part of mutual impedance.

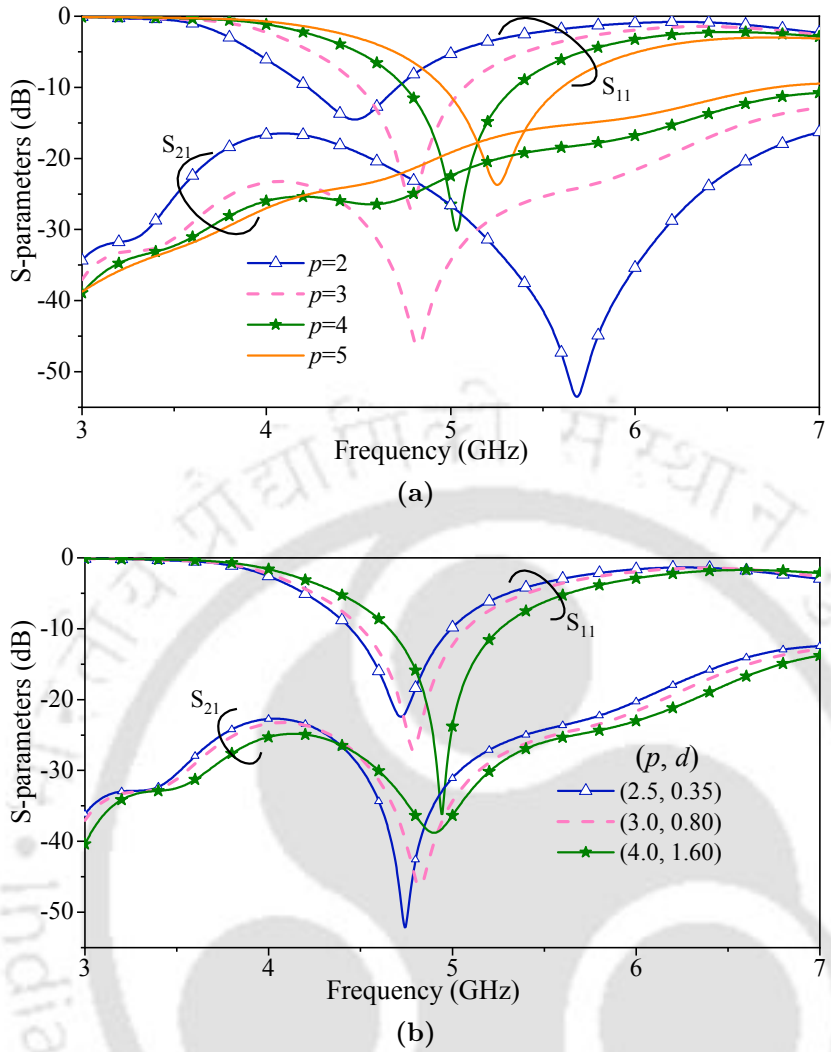

Fig. 5.6: S-parameters study for: (a) different values of p with $d = 0.8$, (b) various combinations of p and d. Dimensions are in mm.

in Fig. 5.6(a). It is noted that increasing the value of p alone is not sufficient to reduce the mutual coupling effectively at the resonance frequency. However, a particular combination of p and d helps to reduce the mutual coupling efficiently at the resonance frequency, as shown in Fig. 5.6(b).

The two-port DRA can be modeled as its equivalent R-L-C circuit to get better insight into the proposed mutual coupling reduction mechanism. The equivalent circuit models are shown in Figs. 5.7(a) and 5.7(b). A parallel R-L-C resonator is considered to model each half-split perturbed DRA with an air gap, where C_d, L_d, R_d are the capacitance, the inductance, and the resistance associated with each DRA block. C_{air} is the capacitance due to the air gap. C is the capacitance between the copper clad of the FR-4 sheet and the ground plane, whereas L is

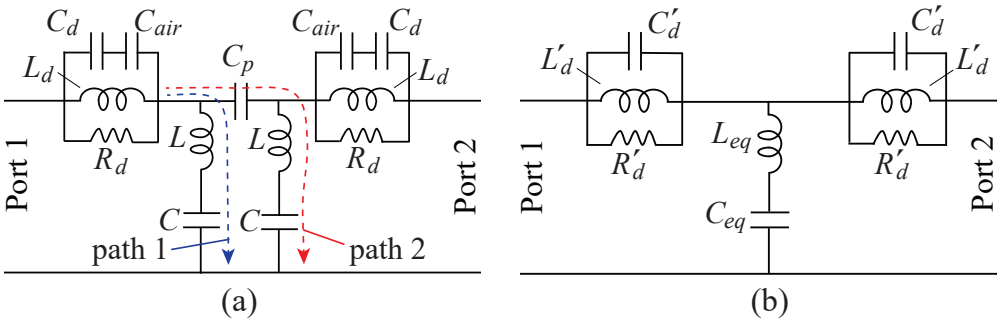

Fig. 5.7: Proposed circuit model of the two-port DRA: (a) detailed equivalent circuit, (b) simplified equivalent circuit. Circuit parameters at 4.79 GHz: $R'_d = 50\ \Omega$, $C'_d = 3.97$ pF, $L'_d = 0.2786$ nH, $L_{eq} = 0.663$ nH, and $C_{eq} = 1.67$ pF.

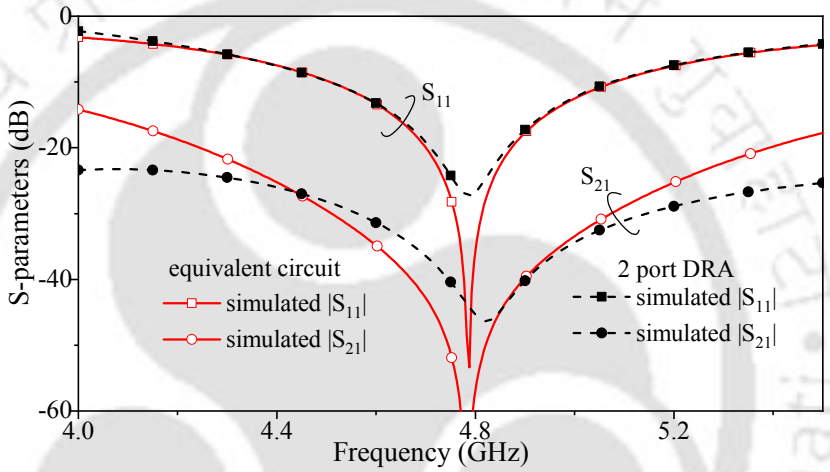

Fig. 5.8: Model validation by comparing the S-parameters of the equivalent circuit model with the S-parameters of the two-port DRA.

the inductance of the copper clad. C_p denotes the capacitance of the FR-4 sheet. When there is a resonance in path 1, i.e., short-circuit, the signal that is supposed to be coupled from Port 1 to Port 2 follows path 1 and ensures minimum mutual coupling with the other port. If there is no resonance in path 1, then C_p can be varied by changing the thickness of the FR-4 sheet and can ensure resonance in path 2. From Fig. 5.5(b), it is clear that for $d = 0.8$ mm, the minimum mutual impedance is seen, and for this particular value of d, the minimum mutual coupling is observed at the resonating frequency (refer to the inset of Fig. 5.5(a)). In this manner, copper cladded FR-4 sheet reduces the mutual coupling precisely at the resonating frequency. The circuit diagram of Fig. 5.7(a) can be reduced to the circuit diagram of Fig. 5.7(b). At the resonating frequency of the antenna, the equivalent circuit parameters of Fig. 5.7(b) are calculated, and its S-parameters with the simulated S-parameters of the antenna are

plotted in Fig. 5.8. A close match between them further validates the proposed equivalent circuit. By using the center frequency and bandwidth, the Q-factor is calculated from the $|S_{11}|$ curve. Knowing the Q-factor and applying the condition of resonance in parallel R-L-C circuit, L'_d and C'_d values are calculated. The antenna impedance (R'_d) at resonance should be 50 Ω. Under the resonance condition, the parallel R-L-C circuit in the left arm (corresponding to Port 1) of Fig. 5.7(b) reduces to a purely resistive circuit having R'_d. To ensure that no signal flows to Port 2, the resonance condition is applied to a series R-L-C circuit (R'_d = 50 Ω, L_{eq}, and C_{eq}) as seen from Port 1. The values of the L_{eq}, and C_{eq} are determined by using the resonance condition for the series R-L-C circuit and its Q-factor value, which is calculated from the bandwidth and center frequency of the $|S_{21}|$ curve.

Table 5.1: Design parameters for various cases.

Cases	ϵ_{rd}	r_d	p	d	g	L_g	W_g
Case A	7.5	9	3	1	0.965	50	50
Case B	10	10	3	0.8	1.065	50	50
Case C	16	9	3	0.5	1.215	50	50

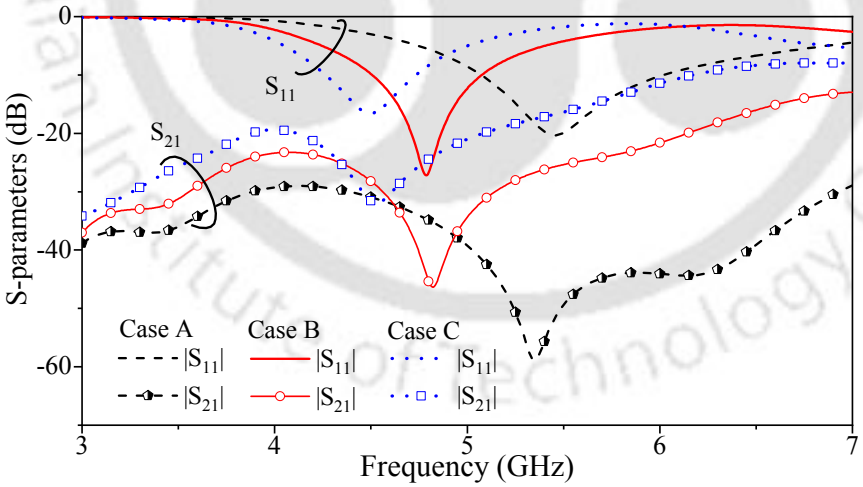

Fig. 5.9: S-parameters for various DRA configurations. Dimensions are in mm.

The FR-4 sheet for the mutual coupling reduction is also used for different DRA materials and design parameters, as depicted in Table 5.1. The S-parameters for these cases are shown in Fig. 5.9. It appears to work quite well in reducing the mutual coupling for all three cases.

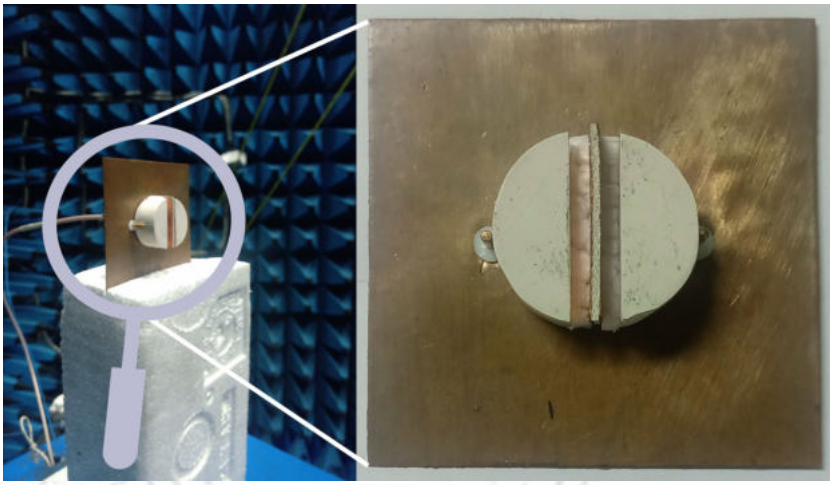

Fig. 5.10: Fabricated prototype of two-port MIMO DRA in an anechoic chamber and its magnified view. All dimensions are as per Fig. 5.4.

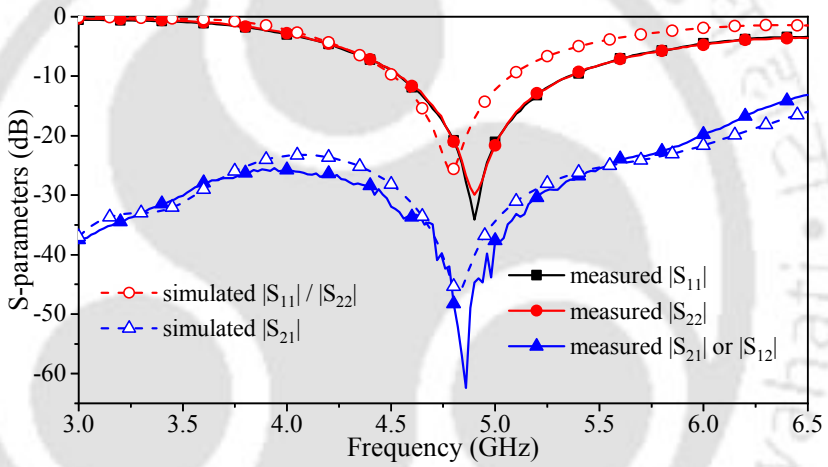

Fig. 5.11: Simulated and measured S-parameters of proposed antenna.

5.3 Results and Discussions

Fig. 5.10 shows a prototype of the two-port MIMO DRA that is fabricated and tested to validate the proposed design. Measurements are done using a 2-Port ShockLine vector network analyzer (MS46122B) in an automated anechoic chamber. The simulated and measured S-parameters for the fabricated prototype are shown in Fig. 5.11. The measured impedance bandwidth is approximately 16% (4.54-5.34 GHz), which is slightly higher than the simulated bandwidth, 4.51 to 5.07 GHz (12%). Despite this, the reflection coefficient characteristics are close to those measured and simulated. The $|S_{21}|$ parameter measures the mutual coupling or isolation between the MIMO antenna's ports. It is measured to be about -44 dB near the center

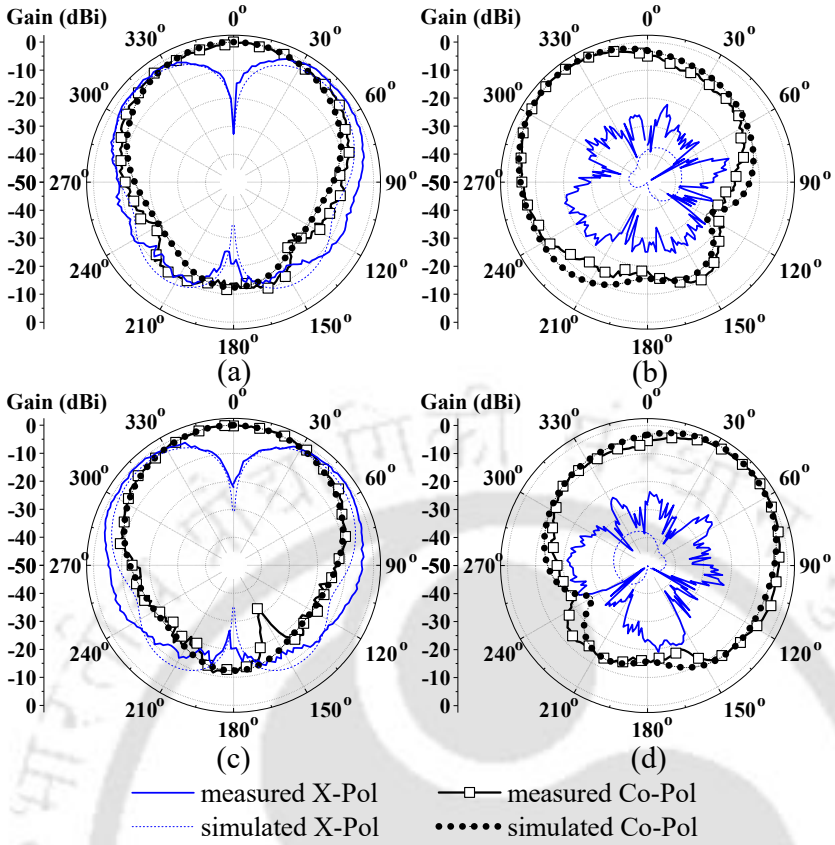

Fig. 5.12: Co- and cross-polar radiation patterns at 4.9 GHz: for Port 1 (a) $\phi = 0^0$ plane, (b) $\phi = 90^0$ plane; for Port 2 (c) $\phi = 0^0$ plane, (d) $\phi = 90^0$ plane.

frequency (4.9 GHz) and maintained below -27.5 dB over the entire operating bandwidth.

The measured and simulated radiation patterns in $\phi = 0^0$ plane (H-plane) and $\phi = 90^0$ plane (E-plane) for Port 1 and 2 are plotted in Fig. 5.12. During the radiation pattern measurement, the concerned port is excited while the other port is terminated with a 50 Ω matched load. The direction of the maximum radiation for Port 1 and Port 2 excitations are noted in the $\theta = 320^0$ and $\theta = 40^0$ direction, respectively. Note that the radiation patterns corresponding to Port 1 and 2 excitations are almost identical in the $\phi = 0^0$ plane. This is mainly due to the use of a double-side metal-backed FR-4 sheet that is used to reduce the mutual coupling and the DRA size. The tilt in the radiation beam is advantageous for the MIMO antennas used for access points in wireless communications. Very close agreement between the simulated and measured results is revealed for the co-polar (Co-pol) radiation patterns in both the principal planes. However, the cross-polar (X-pol) radiation pattern in $\phi = 90^0$ plane is not matching perfectly. It is because the X-pol radiation is highly sensitive near $\phi = 90^0$, as understood from the simulation results. The radiation patterns for Port 2 in the $\phi = 90^0$ plane are the mirror

images of those for Port 1 with $\phi = 0^0$ plane as the mirror plane. The measured and simulated gain of the antenna for a single port excitation (Port 1) are plotted in Fig. 5.13. The measured gain lies from 4.39 to 6.7 dBi within the antenna's operational bandwidth.

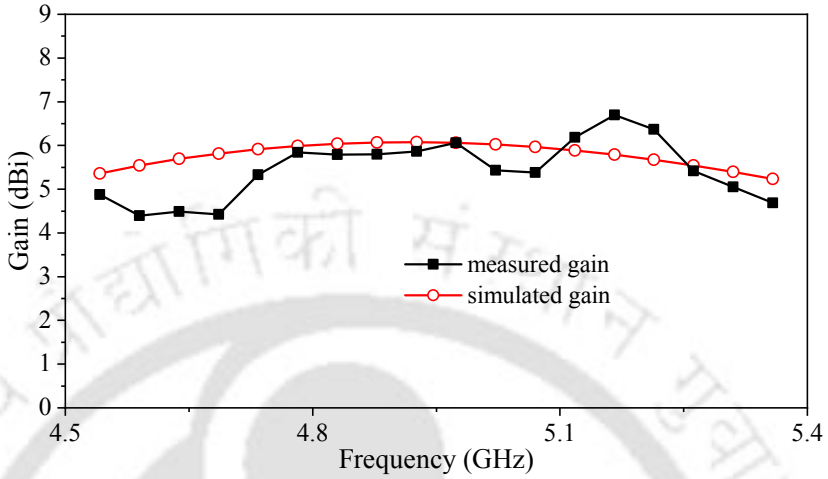

Fig. 5.13: Measured and simulated gain of the antenna.

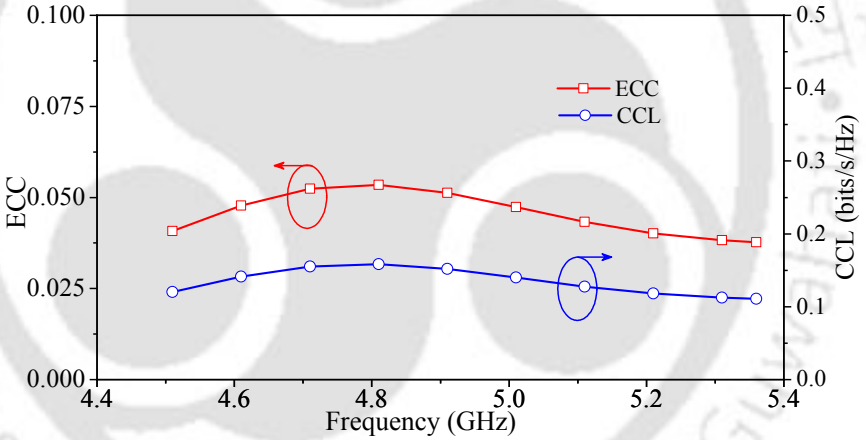

Fig. 5.14: ECC and CCL versus frequency.

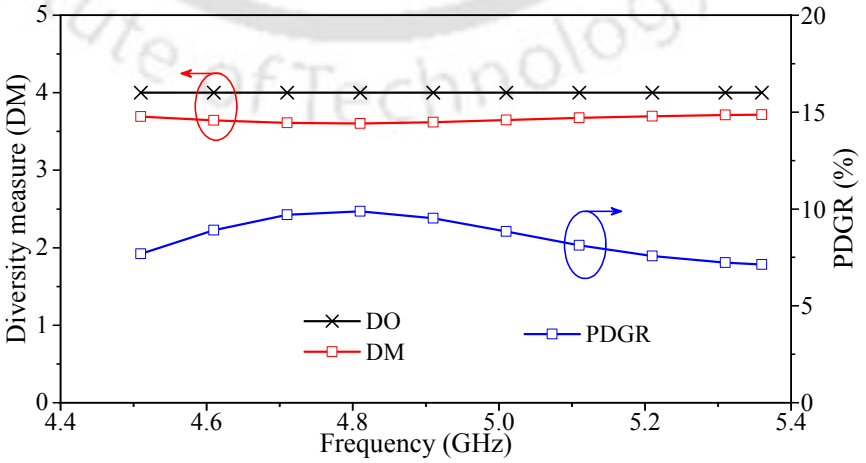

Fig. 5.15: DM and PDGR versus frequency.

The ECC is calculated using (1.12) and (1.13) from chapter 1 and is plotted in Fig. 5.14. The ECC for this dual-port MIMO antenna is noted to be less than 0.053. The correlation among antennas causes the loss in the channel capacity. Considering this MIMO antenna deployed on the transmitter and receiver sides of a 2×2 MIMO system, the channel capacity loss due to the correlation can be calculated using (1.24) from chapter 1 and is plotted in Fig. 5.14. The CCL for this MIMO system is noted to be less than 0.15 bits/s/Hz.

Table 5.2: Comparison of the proposed two-port half-split CDRA with other dielectric resonator-based two-port MIMO antennas.

Refs.	Band-width (GHz)	Volume (λ_0^3)	Gain (dBi)	Edge to edge spacing (λ_0)	Mutual Coupling (dB)	Min. of DRAs	Mutual coupling reduction technique
[57]	3.78-4.07 (7.3 %)	1.26×1.26×0.22	1.7-5.3	not applicable	below -17.7 & up to -24.3 dB	No	Orthogonal mode excitation
[58]	56.5-64.8 (13.6 %)	2.05×2.05×0.35	7.9	0.189	below -15 & up to -46.5 dB	No	Metasurface shield or wall between CDRAs
[59]	57-63 (10 %)	0.95×0.95×0.36	5.4-6.3	0.285	below -26.5 dB & up to -63.5 dB	No	Frequency selective surface wall between CDRAs
[70]	27.19-28.48 (4.7 %)	1.81×1.81×0.25	7.4-9.24	0.118	below -24 & up to -28 dB	No	Printing of metallic strips on RDRAs
[71]	25-27 (7.6 %)	1.48×1.33×0.13	5.8-6.6	0.07	below -24 & up to -50 dB	No	Insertion of metallic vias in RDRAs
Prop.	4.54-5.34 (16.2 %)	0.75×0.75×0.15	4.39-6.7	0.045	below -27.5 & up to -62.3 dB	Yes	Using copper cladded substrate between half-split CDRAs

Refs.: References, CDRA: cylindrical dielectric resonator antenna, RDRA: rectangular dielectric resonator antenna, λ_0: highest operating wavelength.

Using (1.18), the DO for the above described 2×2 MIMO system within the operating bandwidth is found to be 4. The DM is calculated using (1.19) and plotted along with the DO

in Fig. 5.15. The percentage diversity gain reduction (PDGR) is a parameter that measures the reduction in the diversity performance of a MIMO antenna due to correlation between antennas. The PDGR versus frequency curve is plotted in Fig 5.15 and is noted to be less than 9.88 %.

The performance comparison of the proposed MIMO antenna with other DRA-based 2-port antennas is summarized in Table 5.2. Compared to the previously reported works, the proposed MIMO antenna has the best mutual coupling performance and the smallest volume with the lowest edge-to-edge spacing. The proposed MIMO antenna offers a better percentage bandwidth than the other works. Moreover, among the other mutual coupling reduction techniques, the proposed method works effectively with an additional feature of size miniaturization. However, the gain of the proposed antenna is slightly low compared to [58] and [70]. It is mainly due to the size-miniaturized DRAs used in the proposed design.

5.4 Conclusions

A double-side copper-cladded substrate has been used to achieve high isolation between antenna ports in the E-plane while reducing the size of a CDRA by 50%. The fabricated prototype is tested, and the measured results are found to be in close agreement with the simulated prediction. The work demonstrates that the minimum mutual impedance has been achieved precisely at the resonance frequency by controlling the substrate thickness, resulting in a low mutual coupling. The validity of the proposed technique is tested for different resonating frequencies by changing dielectric materials and design parameters, and found to work well. The low values of mutual coupling, ECC, and PDGR over the operating bandwidth have made this antenna a promising candidate for MIMO-based wireless communication. Various shapes and configurations of DRAs with more ports can be explored in the future to improve the MIMO performance further.

6

Π/8-Mode Partial SIW Cavity Based 8-Port MIMO Antenna

Because of various design and fabrication challenges involved in the substrate-integrated waveguide (SIW) antenna design, SIW-based MIMO antennas have not been reported much unlike microstrip-based MIMO antennas in the literature. Half mode SIW (HMSIW) and quarter mode SIW (QMSIW) antennas have gained enormous interest in the antenna community due to the offered advantage of size reduction compared to full mode SIW antennas. Thus, by utilizing the fraction-mode SIW antenna technology, compact MIMO designs can be realized. This chapter presents one such Π/8-mode partial SIW cavity-based compact 8-port MIMO antenna.

6.1 Introduction

It is noted that SIW-based MIMO antennas have not been reported much like microstrip-based MIMO antennas in the literature because of various design and fabrication challenges involved in the SIW antenna design. However, SIW cavity-based antennas possess a noteworthy feature of size miniaturization by employing fraction mode SIWs (half-mode (HM), quarter-mode (QM), eight-mode (8M), etc.) [93, 94]. In addition, SIW cavities are known for their low profile, ease of integration, and self-consistent electrical shielding [95]. The size miniaturization feature of fraction-mode SIW antennas enables placing more antennas into limited space on the receiver/transmitter sides with low mutual coupling.

A few SIW-based multi-port MIMO antennas are presented in chapter 2 [34], [72–77]. The SIW cavity-based MIMO antennas have either two or four ports because of various limitations in the HM, QM, and 8M designs to get an aperture (the wall or boundary with no vias) for radiation. Rotational symmetry may help in packing more antennas in a limited space. Various rotationally symmetric MIMO antennas are reported in [96–100]. Most of them have either three or four ports. An SIW horn-based array antenna in [101] uses an electrically thick substrate ($0.13\lambda_0$) and provides the end-fire radiation. However, the presented work uses an electrically thin substrate ($0.03\lambda_0$) and has a broadside beam.

This chapter presents a $\pi/8$-mode[1] partial[2] SIW (PMPSIW) radiator. It is demonstrated that the field configuration of TM_{220} diagonal mode in the rectangular cavity made up of complete via walls can be retained using partial via walls. To the best of the authors' knowledge, such a realization of a sector-shaped PMPSIW antenna design from the TM_{220} diagonal mode of the entire rectangular cavity is presented for the first time. The vias contribute not only to the realization of PMPSIW radiators but also help to achieve low mutual coupling among the radiators. Using this PMPSIW design concept, an 8-port MIMO antenna is designed. The 8-port MIMO antenna bandwidth is increased by more than 100% by etching radiating slots in each antenna's top and bottom layers. The slot-loading increases the radiated power, which causes a reduction of the cavity Q-factor. In addition, the slots are other resonators whose resonant frequencies can be controlled by varying the slot dimension and location.

[1] As HM uses half of the full-mode SIW, QM uses a quarter of the full-mode SIW. Similarly, $\pi/8$-mode uses $\pi/8^{th}$ of the full-mode rectangular cavity.

[2] The antenna is derived from the rectangular SIW cavity that has few vias in place of full via-walls, unlike [34], [72–77] in chapter 2.

The remainder of this chapter is organized as follows. The concept and design evolution of the proposed PMPSIW antenna are explained in Section II. Section III introduces an 8-port MIMO antenna. In Section IV, the results and discussions are presented. Lastly, conclusions are drawn in Section V of this chapter.

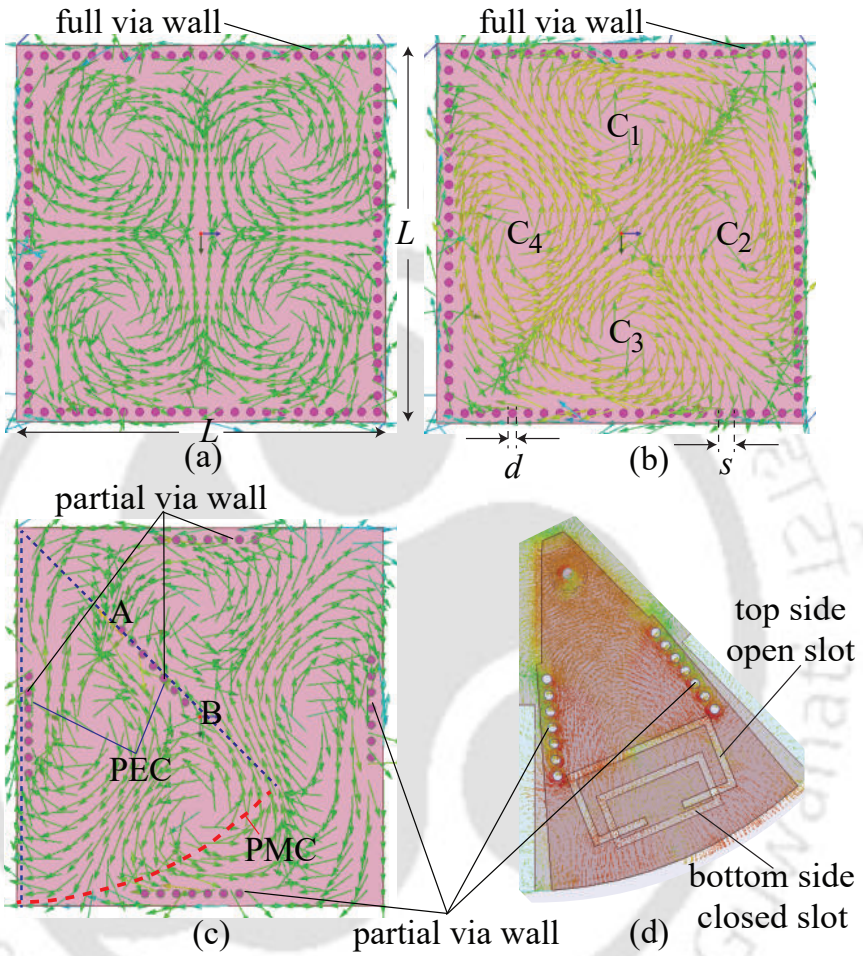

Fig. 6.1: Magnetic field lines: (a) TM_{220} side full SIW mode, (b) TM_{220} diagonal full SIW mode, (c) TM_{220} diagonal partial SIW mode, and (d) TM_{220} diagonal-PMPSIW using partial PEC and PMC truncation (PMPSIW MIMO antenna element).

6.2 Concept and Design Evolution

The TM_{220} mode of the rectangular SIW cavity can be classified into two categories: the conventional TM_{220} mode, the TM_{220} side mode, and the TM_{220} diagonal mode. The indices m, n in TM_{mn0} side mode indicate the number of variations in the standing wave pattern in the x- and y-axis directions. The index zero corresponds to the z-axis direction because the

cavity is thin and very small compared to the wavelength. Similarly, in the TM_{mn0} diagonal mode, m, n indicates the number of variations in the standing wave pattern in the diagonal one and two directions, respectively. The HFSS eigenmode analysis of the entire SIW cavity shows that the resonance frequency of the TM_{220} diagonal mode is close to that of TM_{220} side mode. The TM_{220} side and diagonal modes in the SIW cavity are shown in Figs. 6.1(a) and 6.1(b), respectively. It can be observed that magnetic field lines form four loops, and the region where two magnetic field loops split, the electric field is zero (weak electric field region). The center of each loop (denoted as C_1, C_2, C_3, and C_4) has a maximum electric field, where a vertical electric current can be used to excite the entire cavity. Notice that one current at this location can excite such a cavity mode, but also other modes can be excited. To purely excite this particular mode, four electric current sources should be used with the same magnitude but with alternating phases. The phases will be, for example, clockwise arranged to be 0^0 at C_1, 180^0 at C_2, 0^0 at C_3, and 180^0 at C_4. Thus, a perfect electric conductor (PEC) can be placed vertically without disturbing the field distribution or the cavity resonance frequency. This will create four smaller cavities quarter the size of the entire cavity. This is similar to the concept used in [89] with dielectric resonators, where PEC and perfect magnetic conductors (PMC) were used to reduce the cavity size by using only a part of the entire cavity. In addition, it is possible to split even the quarter-size cavity into two or four using the concept in [89] and implemented in [64] to create a four-port MIMO DRA. Also, if the PEC wall size is reduced to be part of the whole wall and represented by vertical vias to replace the PEC partially, this can be considered as cavity perturbation that will cause the tuning of the original resonant frequency, but the field distribution will be almost the same as the original distribution. As can be seen in Fig. 6.1(c), by just using a few metallic vias at the side walls and a few vias at the minimum electric field region along the diagonal between them (i.e., along the line AB), the field distribution of the TM_{220} diagonal mode is almost retained.

The main advantage of this configuration is that it has open apertures, reducing the Q-factor and increasing the antenna bandwidth. The possible truncation of the cavity as a sector by using PEC boundaries in the form of partial via wall and a curved PMC boundary as an open aperture, depicted in Fig. 6.1(c) with dotted lines, makes the structure compact, keeping the same magnetic field distribution in a smaller area. The ratio of the sector area shown in Fig. 6.1(d) to the rectangular SIW entire cavity is $\pi/8$. Hence, this design is named $\pi/8$-mode partial

SIW cavity. The PMPSIW design evolved from the fraction-mode design concept [94] from the rectangular SIW cavity that presents a compact sector-shaped individual radiator, which can fit well in the neighboring space to realize a compact rotationally symmetric 8-element MIMO antenna.

As a non-radiating cavity, it can also be used as a multi-port power divider, as in [102–104], which for this particular mode is a 1:3 power divider with the opposite port in-phase and the other surrounding ports being out of phase. It will be proposed in the near future.

The resonant frequency of the TM_{mn0} side mode of the thin rectangular SIW resonator can be calculated using (6.1) & (6.2) from [105] and [106], respectively.

$$f_{mn0}^{SIW} = \frac{c}{2\pi\sqrt{\epsilon_r \mu_r}} \sqrt{\left(\frac{m\pi}{L_{\text{eff}}}\right)^2 + \left(\frac{n\pi}{L_{\text{eff}}}\right)^2} \tag{6.1}$$

$$L_{\text{eff}} = L - 1.08\frac{d^2}{s} + 0.1\frac{d^2}{L} \tag{6.2}$$

where c is the velocity of light in free space, $m = 1, 2, ...$, $n = 1, 2, ...$, and ϵ_r & μ_r are the relative permittivity and permeability of the substrate, respectively. L is the cavity side-length, d is the via diameter, and s is the distance between the centers of vias.

An 8-port MIMO antenna utilizing this PMPSIW radiator is shown in Fig. 6.2. The initial dimension (L) of the sector-shaped patch for the TM_{220} diagonal-PMPSIW antenna design is calculated using (6.1) and (6.2) for the TM_{220} side mode because of their proximity in the resonance frequency. For the TM_{220} side mode to resonate at 6 GHz, the initial dimension (L, as shown in Fig. 6.2) is found to be 46.8 mm with $d = 1$ mm and $s = 2$ mm, which is further optimized as $L = 46.5$ mm for better results. The parameters d and s are chosen to satisfy the criteria $d < \lambda_g/5$ and $s \leq 2d$ to minimize the power leakage between the vias. The PMPSIW radiators are placed at a radially offset distance from the center to accommodate coaxial connectors in the bottom layer.

A circular substrate made up of Rogers RT-Duroid 5870 with thickness h of 1.57 mm, a dielectric constant of $\epsilon_r = 2.33$, and a loss tangent of $\tan(\delta) = 0.0012$ is used for the antenna design. Each antenna has a sector-shaped patch in the top layer with metallic vias along its straight edges. Ports P_1-P_8 are placed towards the end of the sector-shaped patch's narrower side.

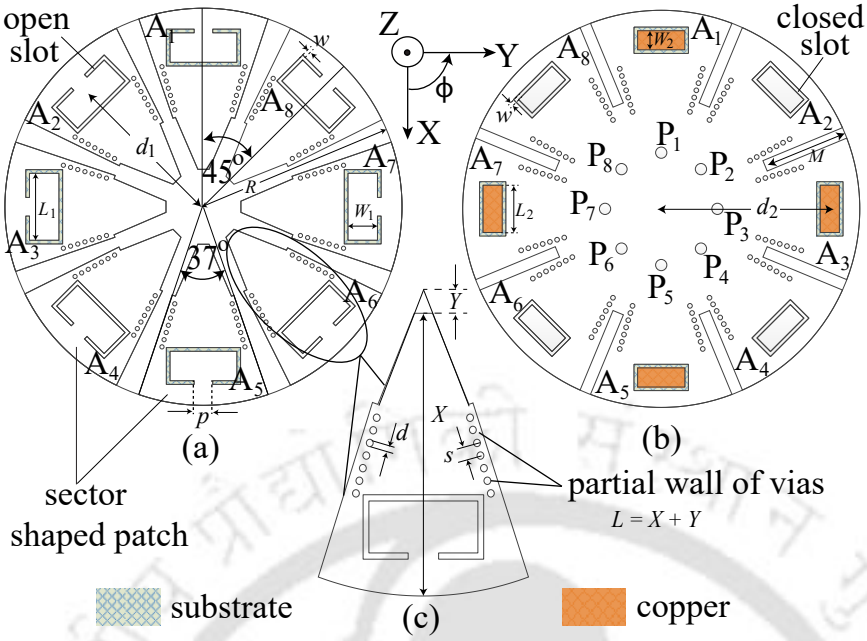

Fig. 6.2: Antenna geometry for 8-port MIMO operation: (a) top layer, (b) bottom layer, and (c) magnified view of the patch. Design parameters: $R = 53, W_1 = 7.6, L_1 = 17.6, W_2 = 5.1, L_2 = 12.6, M = 23, p = 5, s = 2, d = 1.2, Y = 3.5, X = 43, d_1 = 42.6, d_2 = 45.2, w = 0.95$. All dimensions are in mm.

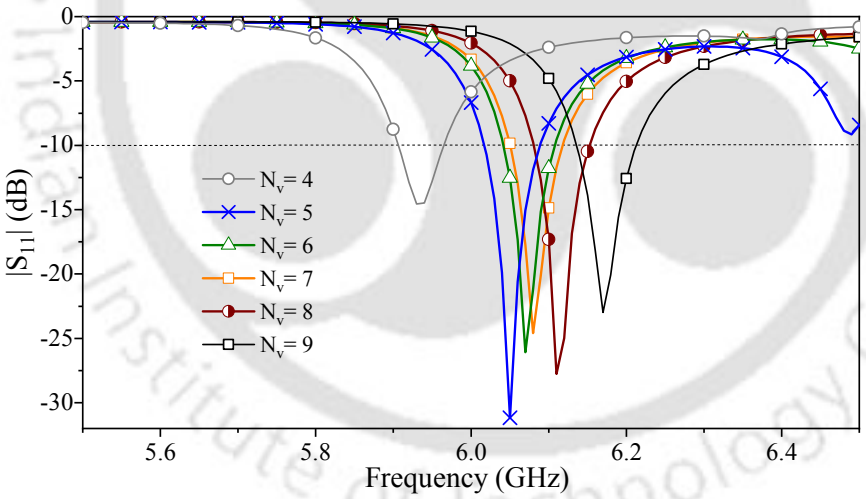

Fig. 6.3: S-parameters of stage 1 for different number of vias (N_v).

6.3 8-port MIMO Antenna

The various intermediate stages are analyzed before the final design. The first stage, i.e., stage 1, has no slot. As stated previously, the change in the number of vias causes cavity perturbation and consequently changes the resonating frequencies. It can be seen in Fig. 6.3, where S-parameters are plotted for the different numbers of via. We have considered seven vias

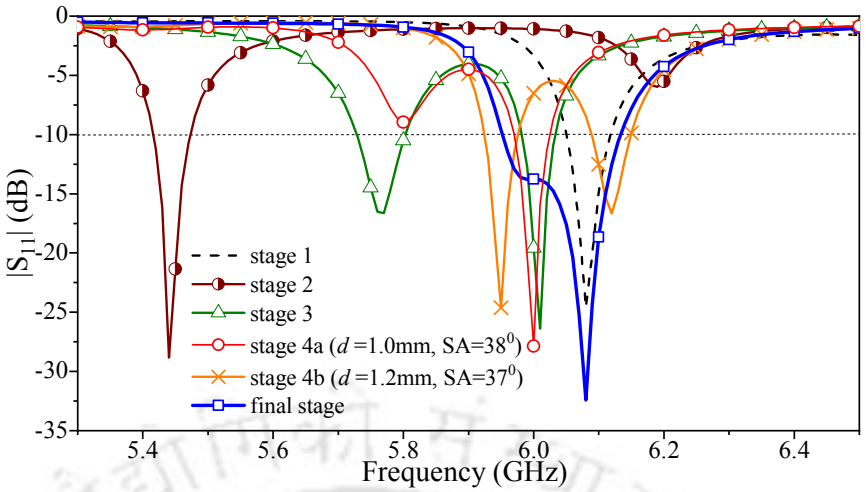

Fig. 6.4: S-parameters for various antenna stages in MIMO operation

for this antenna design. Stage 2 has a rectangular-shaped annular slot (closed slot) beneath each patch in the bottom layer. Similarly, stage 3 has a closed slot, but on the top layer only. Note that for stages 1-4a, $d = 1$ mm, and the sector angle (SA) is 38^0. Stages 4a and 4b have closed slots in the bottom and top layers. The final stage has a closed slot in the bottom layer and an open (C-shaped) slot in each patch in the top layer. Fig. 6.4 shows the S-parameters corresponding to the various stages (design evolution). In stage 1, the antenna resonates at 6.04 GHz and has a bandwidth of 70 MHz. Using (6.1), (6.2), the resonating frequency corresponds to TM_{220} side mode for $L = 46.5$ mm, evaluated as 6.047 GHz, which is very close to the simulated frequency (6.08 GHz) of this PMPSIW radiator without any slot (stage 1 with $N_v = 7$). When a closed slot is loaded in the bottom layer (stage 2), it is seen that the resonating frequency decreases to 5.44 GHz from 6.08 GHz. In stage 3, there are two resonances, one close to the resonance of stage 1 and another at 5.77 GHz. Stage 4a has relatively close resonances than stage 3 but poor impedance matching in the lower resonating frequency range. In stage 4b, via diameter d is changed from 1 to 1.2 mm, and the SA is changed to 37^0 from 38^0 to obtain good impedance matching in both frequency bands. The two resonances of stage 4b are observed at 5.95 and 6.12 GHz. The notable point is that the resonances in stages 4a and 4b are closer than in stage 3. In the final stage, choosing to have a closed slot in the bottom and an open slot in the top layer is basically to achieve more bandwidth. With a closed slot at the bottom layer, having an open slot instead of the closed one in the top layer provides more capacitive loading. It helps to merge the resonances, leading to a better bandwidth (180 MHz),

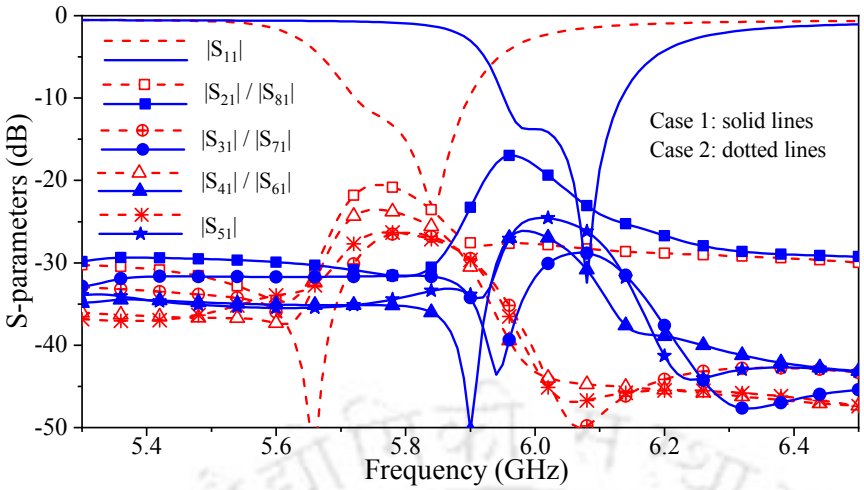

Fig. 6.5: S-parameters for case 1 and case 2.

which is more than 100% improvement from the stage 1 antenna's bandwidth.

The S-parameters for two variations of the final stage (case 1 and case 2) are plotted in Fig. 6.5. For case 1, $d_1 = 44$ mm and $d_2 = 44$ mm, whereas for case 2, $d_1 = 42.6$ mm and $d_2 = 45.2$ mm. The -10 dB impedance bandwidth for case 1 is 120 MHz and 180 MHz for case 2. It can be seen from Fig. 6.2 that ports 2 and 8 are located at rotationally symmetric positions with respect to port 1, and the same is noted in the case of ports 3 & 7 and ports 4 & 6. Thus, only $|S_{21}|$, $|S_{31}|$, $|S_{41}|$, and $|S_{51}|$ are shown in Fig. 6.5. The mutual coupling between the antenna ports is below -17 and -20 dB for cases 1 and 2, respectively.

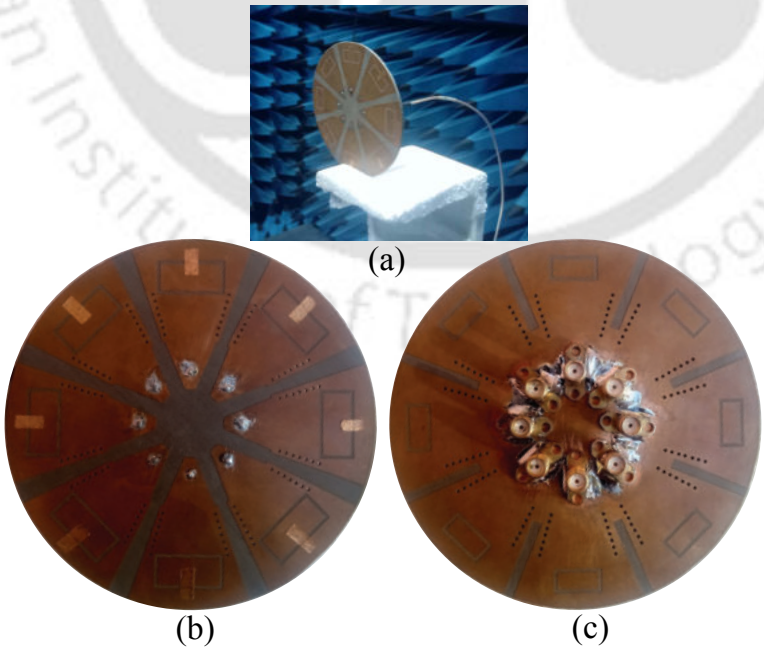

Fig. 6.6: Fabricated antenna prototype: (a) during pattern measurement in an anechoic chamber, (b) top view, and (c) bottom view.

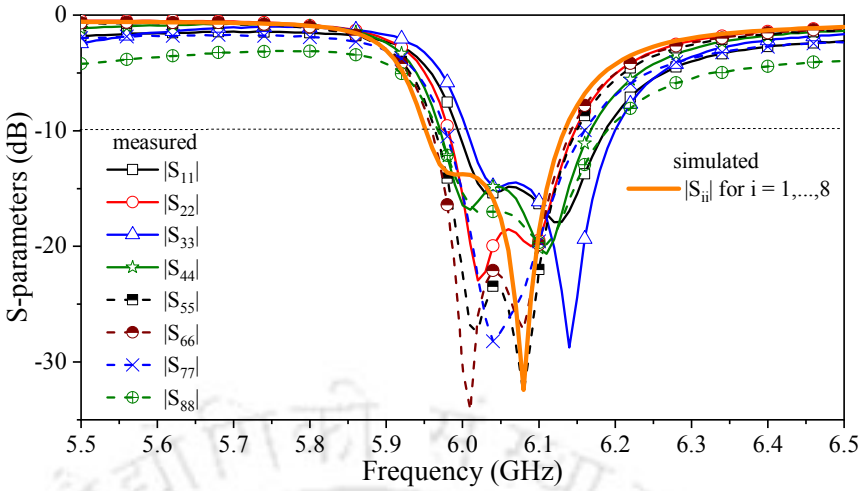

Fig. 6.7: Measured and simulated $|S_{ii}|$ parameters for 8-port MIMO antenna (case 1).

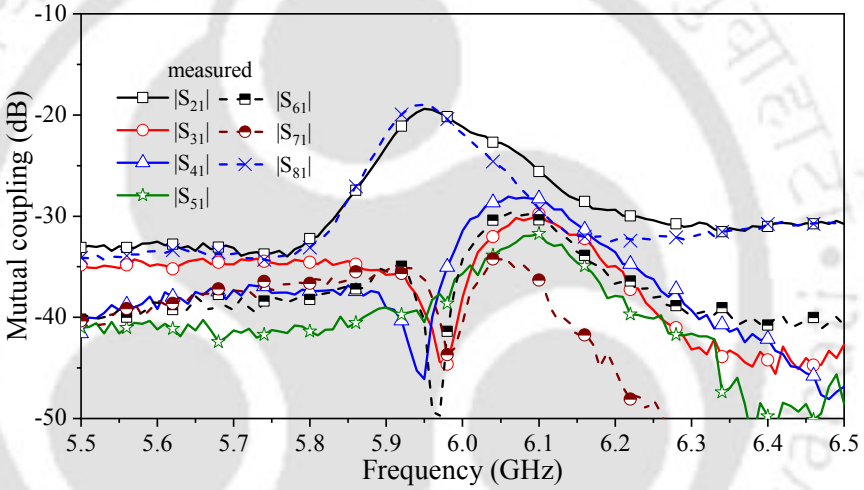

Fig. 6.8: Measured mutual coupling of 8-port MIMO antenna (case 1).

6.4 Results and Discussions

To validate the concept presented, a prototype of the eight-port MIMO configuration (Fig. 6.2) is fabricated (see Fig. 6.6) and tested. The measured and simulated $|S_{ii}|$ parameters for all ports are shown in Fig. 6.7. An N9952A Keysight vector network analyzer is used for the S-parameters measurements. The common measured -10 dB reflection bandwidth for all antennas is from 6.006 to 6.143 GHz (137 MHz), whereas the simulated bandwidth is from 5.95 to 6.13 GHz (180 MHz). The measured mutual coupling within the common bandwidth for all antenna ports is below -21 dB, as shown in Fig. 6.8. The slight deviation between the measured and simulated $|S_{ii}|$ is likely due to fabrication tolerances.

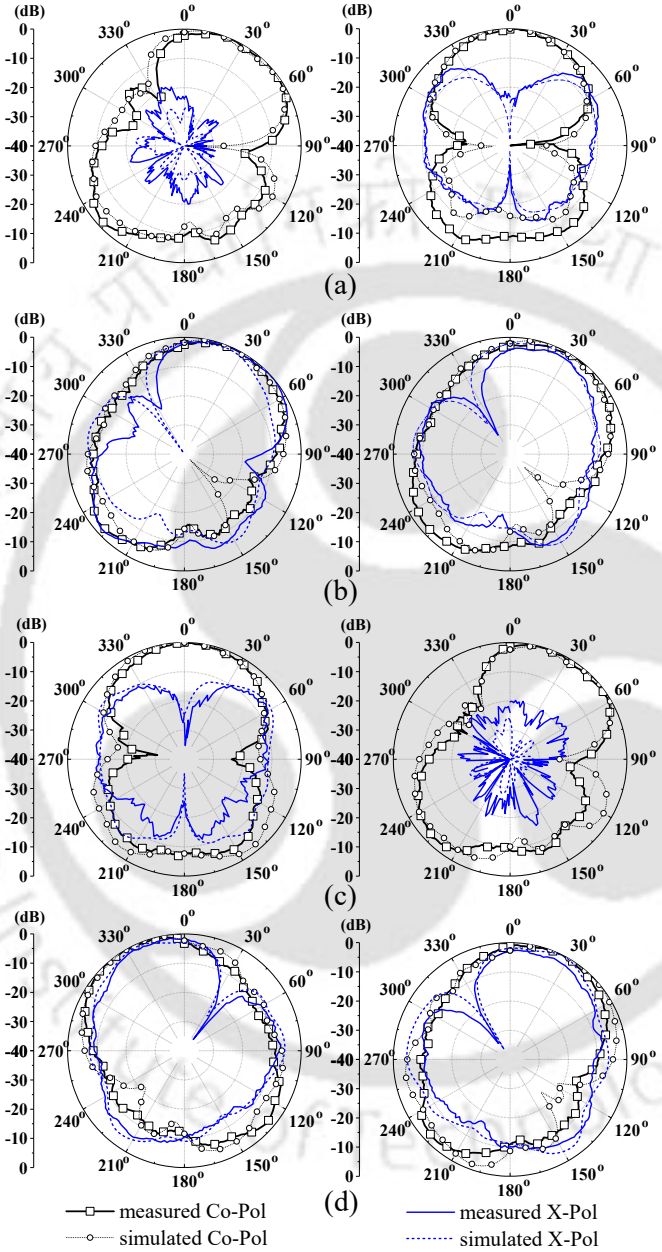

Fig. 6.9: Radiation patterns at 6.08 GHz for $\phi = 0^0$ (LHS), $\phi = 90^0$ planes (RHS): (a) antenna A_1, (b) antenna A_2, (c) antenna A_3, and (d) antenna A_4.

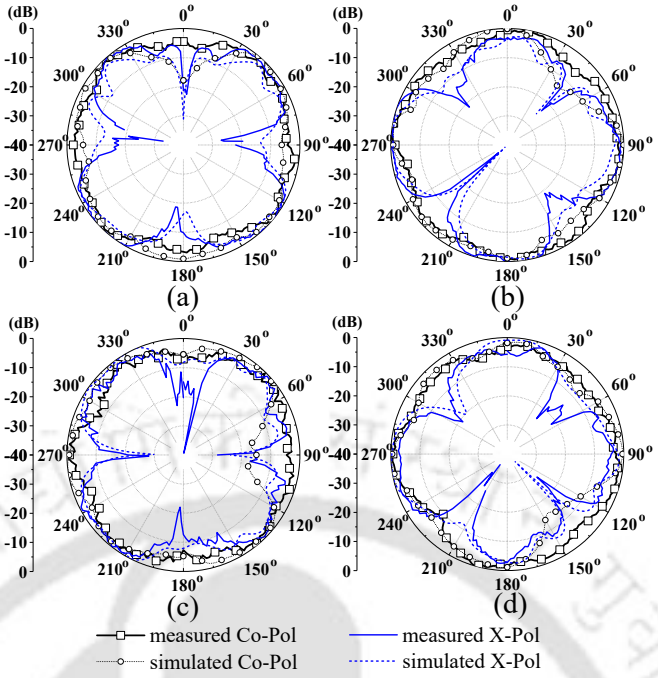

Fig. 6.10: Radiation patterns at 6.08 GHz for $\theta = 90^0$ plane: (a) antenna A_1, (b) antenna A_2, (c) antenna A_3, and (d) antenna A_4.

The radiation patterns in $\phi = 0^0$ and $\phi = 90^0$ planes for ports P_1, P_2, P_3, and P_4 are shown in left-hand side (LHS) and right-hand side (RHS) of Fig. 6.9, respectively. The radiation patterns in $\theta = 90^0$ plane for ports P_1, P_2, P_3, and P_4 are plotted in Fig. 6.10. A good match between simulated and measured radiation patterns is observed. Note that only the concerned port is excited during the pattern measurements, and the rest are terminated with the matched loads. The antenna's measured gain lies between 3.46-4.72 dBi within the common measured bandwidth and is shown in Fig. 6.11.

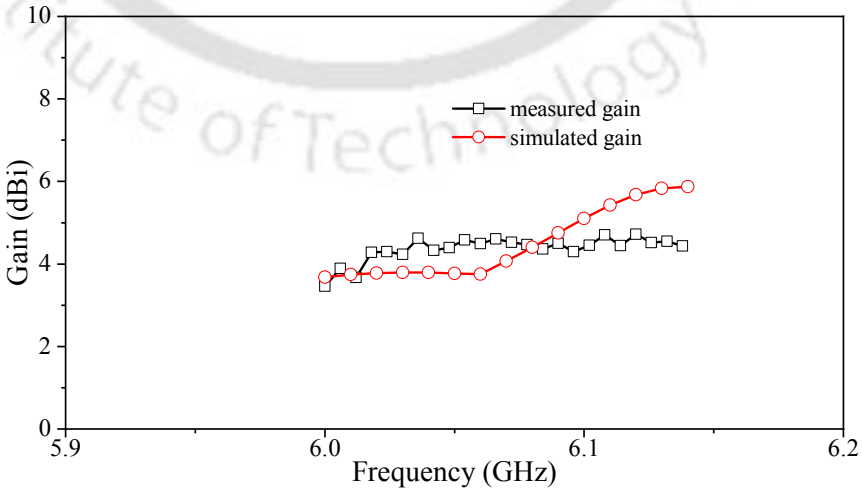

Fig. 6.11: Simulated and measured gain.

The ECC is calculated using (1.12) and (1.13) from chapter 1 and is plotted in Fig. 6.12. The ECC for this 8-port MIMO antenna with the common measured bandwidth (6.006 to 6.143 GHz) is noted to be less than 0.0027. The correlation among antennas causes the loss in the channel capacity. Considering this MIMO antenna deployed on the transmitter and receiver sides of a 8×8 MIMO system, the channel capacity loss due to the correlation can be calculated using (1.24) from chapter 1 and is plotted in Fig. 6.12. The CCL for this MIMO system is noted to be less than 0.108 bits/s/Hz within 6.006 to 6.143 GHz.

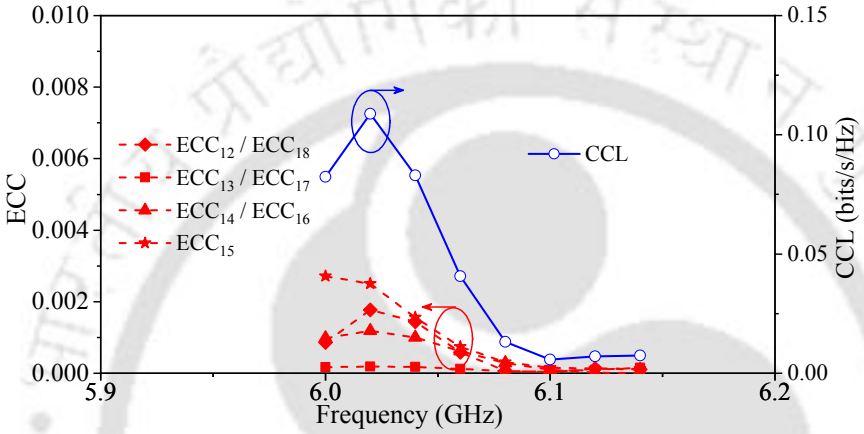

Fig. 6.12: ECC and CCL versus frequency.

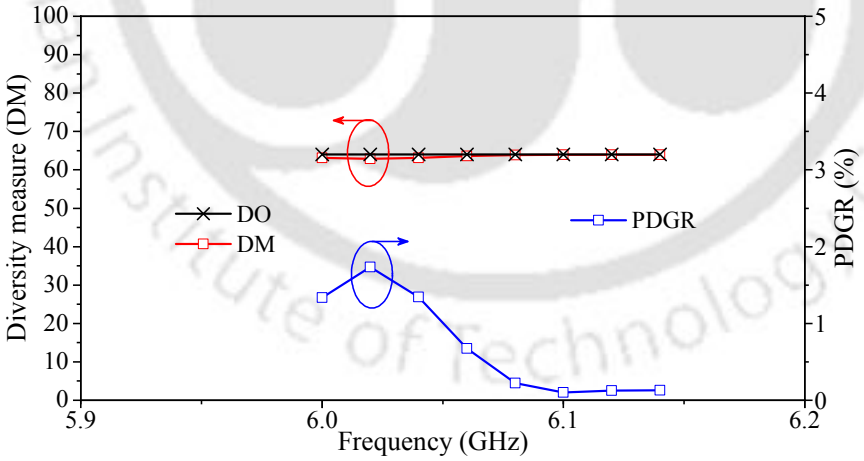

Fig. 6.13: DM and PDGR versus frequency.

Using (1.18), the DO for the above described 8×8 MIMO system within the common measured bandwidth (6.006 to 6.143 GHz) is found to be 64. The DM is calculated using (1.19) and plotted along with the DO in Fig. 6.13. The PDGR is a parameter that measures the reduction in the diversity performance of a MIMO antenna due to the correlation between antennas. The

PDGR versus frequency curve is plotted in Fig 6.13 and is noted to be less than 1.73 %.

Table 6.1: Comparison of the proposed MIMO antenna with other rotationally symmetric MIMO antenna.

Refs.	Band-width (GHz)	Volume (λ_0^3)	Mutual Coupling (dB)	ECC	Effi-ciency	Gain (dBi)	N_p
[96]	3.3-4.2	0.2995	≤ -14	≤ 0.05	≥ 88	6.6	3
[97]	3.3-4.2	0.2351	≤ -15	≤ 0.01	≥ 88	NA	3
[98]	3.5-5	0.2351	≤ -13	≤ 0.05	≥ 84	6.8	4
[99]	3.3-4.2	0.00235	≤ -9.5	≤ 0.06	≥ 40	2	4
[100]	3.3-4.2 (-6 dB refl.)	0.00245	≤ -9.7	≤ 0.48	≥ 36	0.00416	4
Prop.	6.006-6.143	0.112	≤ -21.17	≤ 0.0027	≥ 90	4.72	8

Refs.: References, Prop.: proposed work, λ_0: highest operating wavelength, N_p: number of ports, NA: information not available.

It can be observed from Table 6.1 that the proposed MIMO antenna has the highest number of ports, the lowest mutual coupling, and ECC with the highest efficiency among the rotationally symmetric MIMO antennas reported in the comparison table. It is also more compact than the existing MIMO antennas except [99] and [100], but these two have much lower gain than our MIMO antenna. In terms of bandwidth, our MIMO antenna has the lowest bandwidth, an inherent property of SIW-cavity-based antennas. However, the bandwidth provided by our antenna is more than sufficient for applications such as MIMO-based video transmitting applications (case 2: 5.7-5.90 GHz) [107–109] or robust Wi-Fi connectivity in unmanned aerial vehicles (UAVs) operating in the 5G New Radio (NR) Frequency Range 1 (FR1) [110, 111] and small access points.

6.5 Conclusions

Using the TM_{220} diagonal mode, a space-efficient PMPSIW antenna can be designed with 61% size miniaturization than the SIW rectangular cavity in its complete mode configuration. The antenna bandwidth is enhanced significantly using the proper slot combinations in the top and bottom layers. The 8-port MIMO antenna bandwidth is from 6.006 to 6.143 GHz, and

antenna efficiency is better than 90%. The low inter-port mutual coupling, ECC, and PDGR make this antenna suitable for MIMO-based video transmitting applications or robust Wi-Fi connectivity in unmanned aerial vehicles (UAVs) operating in the 5G NR FR1 and small access points.

7

Summary of Contributions and Future Scope

A good amount of work has been done in the literature so far in the context of multi-port MIMO antenna design. This thesis presents 2-port, 6-port, and 8-port space-efficient, low electromagnetically coupled MIMO antenna designs with small edge-to-edge spacing. The performance of all proposed antennas has been analyzed in terms of mutual coupling, envelope correlation coefficient, channel capacity loss, and percentage diversity gain reduction. Contributions from each chapter are summarized here with their future scopes.

7.1 Conclusions and Future Scope

This chapter summarizes the contribution of Chapters 1-6 with their future scopes.

Chapter 1 of the thesis provides a detailed overview of the importance and benefits of the MIMO communication system and associated challenges in its realization, mainly multi-port MIMO antenna design. This chapter discusses the reasons behind the electromagnetic coupling between antenna elements and their undesirable effects, such as higher correlation, channel capacity loss, etc. This chapter elaborates on how low mutual coupling and low correlation in MIMO antennas help to improve communication system performance.

Chapter 2 covers various state-of-the-art MIMO antenna design techniques to achieve low electromagnetically coupled antennas. These techniques include electromagnetic band-gap (EBG) structures, defected ground structures (DGS), neutralization line technique, decoupling surfaces, and SIW-based fraction mode designs. The mutual coupling reduction techniques mentioned above are explained with a few representative MIMO antenna designs from the literature, with their merits and further scope for improvements.

Achieving low mutual coupling with small inter-element spacing between antennas is a key challenge in the MIMO antenna design. Hence, this thesis aimed to design multi-port MIMO antennas with small edge-to-edge inter-element spacing (i.e., less than $0.1\lambda_0$) and low mutual coupling. Chapters 3 and 4 contain two MIMO antennas each, whereas chapters 5 and 6 include one MIMO antenna each. The conclusions with the future scope for each work are summarized herewith.

The first part of chapter 3 contains a two-port dual-band antenna, whereas the second part presents a six-port antenna for the MIMO applications. The spacings between antennas for the two-port and six-port MIMO antenna are noted to be $0.092\lambda_0$ and $0.076\lambda_0$, respectively. Compared to the electromagnetic band-gap and array decoupling surface technique, as discussed in the literature survey, the neutralization line technique offers a simple and effective method to design multi-port antennas with low mutual coupling. Using NLs, two-port, three-port, four-port, and six-port antennas with an inter-connected structure can be developed. The use of a neutralization line (NL) can be further extended to the multi-port MIMO DRA. An antenna with the integration of a filter is known as a filtering antenna or filtenna. Using the NL technique, MIMO-filtenna designs can be explored.

Chapter 4 of the thesis presents a single negative (SNG) meta-grid line structure. This struc-

ture can be integrated with the ground plane and can mitigate the mutual coupling in a two-port coplanar waveguide (CPW)-fed printed monopole antenna (TPCFMAA) and patch-fed two-port MIMO dielectric resonator antenna (TPMDRA) designs without adding any additional space. The edge-to-edge spacings between antennas in the TPCFMAA and the TPMDRA are noted to be $0.015\lambda_0$ and $0.09\lambda_0$, respectively. The possible extension of this work includes the use of SNG meta-grid lines with different shapes of the DRA. The usage of the SNG meta-grid line structure can also be investigated along with the neutralization line technique for mutual coupling reduction.

In chapter 5, a double-side copper-cladded substrate is used to achieve high isolation between antenna ports in the E-plane while reducing the size of a CDRA close to 50%. This work demonstrates that the minimum mutual impedance has been achieved precisely at the resonance frequency by controlling the substrate thickness, resulting in a low mutual coupling. The validity of the proposed technique is tested for different resonating frequencies by changing dielectric materials and design parameters and found to work well. The height of the copper-cladded substrate is kept the same as that of the half-split CDRAs. Therefore, this technique does not add additional space or height to the MIMO antenna profile and provides a space-efficient approach for mutual coupling reduction in the MIMO DRA. The edge-to-edge spacing in this two-port half-split CDRA is noted to be $0.045\lambda_0$. If in a two-port half-split CDRA, each split-DRA block has a different dielectric constant; the work can be extended to design the two-port diplexing antenna. The proposed use of vertical copper-cladded substrate for mutual coupling reduction may be further explored with various dielectric resonator antenna shapes, such as equilateral DRA, rhombus DRA, etc., in the future to improve the MIMO performance further.

The sixth chapter presents a space-efficient $\pi/8$-mode partial SIW (PMPSIW) cavity-based MIMO antenna from the TM_{220} diagonal mode of the SIW cavity. This technique can offer 61% size miniaturization compared to the SIW rectangular cavity in its complete mode configuration. It is possible to design 2-8 ports MIMO antennas using the PMPSIW radiator. The bandwidth of the MIMO antenna can be enhanced significantly by using slots in the top and bottom layers. The metallic vias used in the SIW implementation also reduce the coupled energy leakage among radiators, allowing mutual coupling between fraction mode radiators to be kept below -15 dB without extra effort. A further extension of this work is to design self-diplexing, self-triplexing,

and self-quadruplexing multi-port MIMO antennas operating at multiple frequency bands.

List of Publications

Journal publications

1. **M. Mishra**, S. Chaudhuri, R.S. Kshetrimayum, and H. Chel, "Low mutual coupling six-port planar antenna for the MIMO applications", *International Journal of RF and Microwave Computer-Aided Engineering*, Wiley, vol. 30, e22439, 2020 (**Chapter 3**)

2. **M. Mishra**, S. Chaudhuri, R.S. Kshetrimayum, A. Alphones, and K. P. Esselle, "Space efficient meta-grid lines for mutual coupling reduction in two-port planar monopole and DRA array", *IEEE Access*, vol. 10, pp. 49829-49838, 2022. (**Chapter 4**)

3. R. S. Kshetrimayum, **M. Mishra**, S. Aïssa, S. K. Koul, and M. S. Sharawi, "Diversity order and measure of MIMO antennas in single-user, multi-user and massive MIMO wireless communications," *IEEE Antennas and Wireless Propagation Letters*, vol. 22, no. 1, pp. 19-23, Jan. 2023. (**Chapter 1**)

4. **M. Mishra**, K. Dutta, R. S. Kshetrimayum, M. S. Sharawi, A. A. Kishk, S. Chaudhuri, and S. Bhunia "Mutual coupling reduction between two tightly packed half-split cylindrical dielectric resonator antenna," (**Revised manuscript submitted against major revision decision to**) *IEEE Transactions on Antenna and Propagation.* (**Chapter 5**)

5. **M. Mishra**, S. Chaudhuri, R. S. Kshetrimayum, M. S. Sharawi, and A. A. Kishk, "A highly efficient & low-mutual coupling partial $\pi/8$ SIW cavity based 8-port MIMO antenna," *IEEE Antennas and Wireless Propagation Letters*, doi: 10.1109/LAWP.2023.3262159. (**Chapter 6**)

Conference publications

1. **M. Mishra**, S. Chaudhuri, and R.S. Kshetrimayum, "Low mutual coupling dual-port dual-band MIMO antenna array for mobile terminal", in Proc. *XXXIIIrd General Assembly and Scientific Symposium of the International Union of Radio Science*, Rome, Italy, 2020, pp. 1–4. (**Chapter 3**)

2. **M. Mishra**, S. Chaudhuri, R.S. Kshetrimayum, and S. Bhunia, "Highly compact DRA array using metallic grid-shaped partial ground plane", in Proc. *2020 IEEE MTT-S International Microwave Workshop Series on Advanced Materials and Processes for RF and THz Applications (IMWS-AMP)*, Suzhou, China, 2020, pp. 1–3. (**Chapter 4**)

3. R. S. Kshetrimayum, **M. Mishra**, and S. Aïssa, "Multiplexing gain and sum-rate loss of MIMO antennas," accepted for *IEEE Microwave Antenna and Propagation Conference*, Bengaluru 2022. (**Chapter 1**)

Other publications

1. **M. Mishra**, S. Chaudhuri, and R.S. Kshetrimayum, "Low mutual coupling four-port MIMO antenna array for 3.5 GHz WiMAX application", in Proc. *2020 IEEE Region 10 Symposium (TENSYMP)*, Dhaka, Bangladesh, 2020, pp. 791–794.

2. **M. Mishra**, S. Chaudhuri, and R.S. Kshetrimayum, "Four-port DRA array for MIMO applications", in Proc. *2020 International Symposium on Antennas and Propagation (ISAP)*, Osaka, Japan, 2021, pp. 765–766.

3. **M. Mishra**, S. Chaudhuri, and R.S. Kshetrimayum, "New design approach for mutual coupling reduction in two-port compact antenna array for W-LAN MIMO applications", in Proc. *3rd URSI AT-AP-RASC*, Gran Canaria, Spain, 2022, pp.1–4.

A

Appendix

Contents

A.1 Mutual Coupling Mechanism in a Transmitting MIMO Antenna

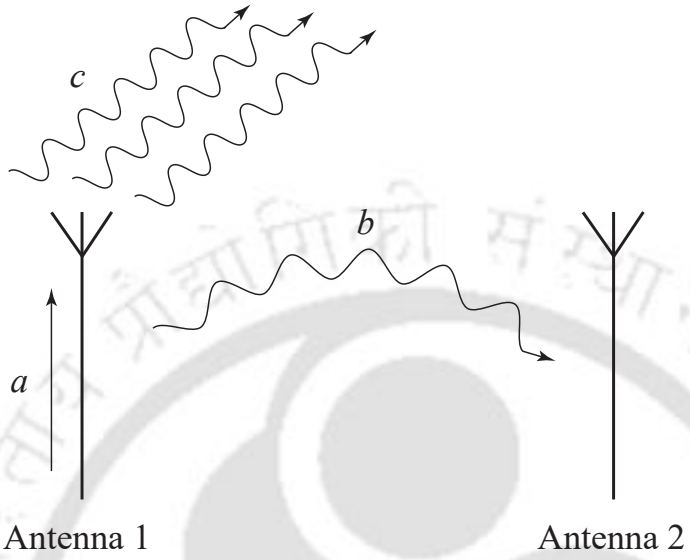

Fig. A.1: A MIMO antenna system with two elements in the transmitting mode.

In the transmit mode, all elements of a MIMO antenna are supposed to radiate the signal only, but this does not happen under practical scenarios. While transmitting, antenna elements also receive a part of the transmitted signal from the nearby antennas. As depicted in the two-antenna system of Fig. A.1, only Antenna 1 is excited with Antenna 2 in its proximity. The amount of power supplied to Antenna 1 is denoted by a, whereas the power radiated from it into the free space is labeled as c. The nearby Antenna 2 also receives some amount of the radiated power (labeled as b) from Antenna 1 due to the electromagnetic (EM) interactions between the closely placed antennas. The power received by Antenna 2 would get partially scattered into its vicinity. Again, Antenna 1 will receive a part of the scattered energy (from Antenna 2) because of the mutual coupling. Such a process will continue indefinitely. Thus, when both the antennas are excited, the EM radiation will be the sum of the radiated fields from the individual antennas and the re-scattered radiations from both the antenna elements [8, 9].

A two-element antenna system comprising two dipole antennas is considered for theoretical circuit modeling of the mutual coupling effect, as shown in Fig. A.2 [9]. Antenna elements are separated by a distance d. The equivalent circuit of these antennas with mutual coupling is shown in Fig. A.3. Let V_{S1} and V_{S2} are the excitation voltages of Antenna 1 and Antenna 2,

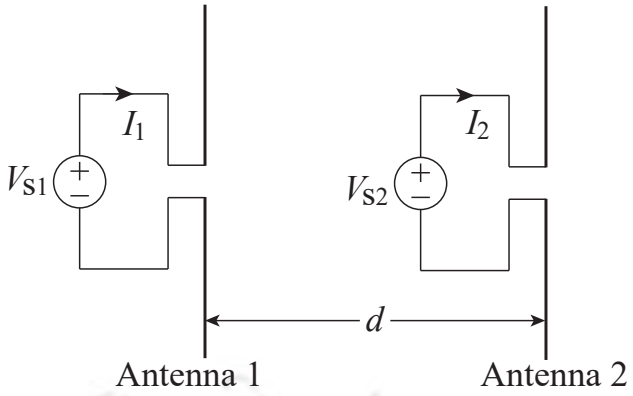

Fig. A.2: A MIMO antenna system comprising two dipole antennas in the transmitting mode.

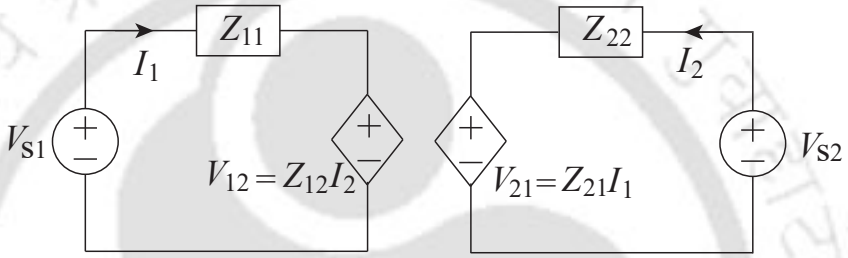

Fig. A.3: The equivalent circuit model of a two-element MIMO antenna system considering the mutual coupling.

respectively. Z_{11} and Z_{22} are the antenna impedances of Antenna 1 and Antenna 2, respectively. The mutual coupling effect is considered in terms of coupled voltage. V_{12} is the coupled voltage on Antenna 1 due to Antenna 2, and V_{21} is the same on Antenna 2 because of Antenna 1. Coupled voltage in terms of mutual impedance can be expressed using (A.1), which is given below.

$$V_{12} = Z_{12}I_2 \qquad V_{21} = Z_{21}I_1 \tag{A.1}$$

Using circuit diagrams shown in Fig. A.3 and Fig. A.4, mutual impedances (Z_{12} and Z_{21}) can be expressed as

Z_{12} = the mutual impedance seen by Antenna 1 with Antenna 2 excited

$$= \frac{V_{12}}{I_2} \tag{A.2}$$

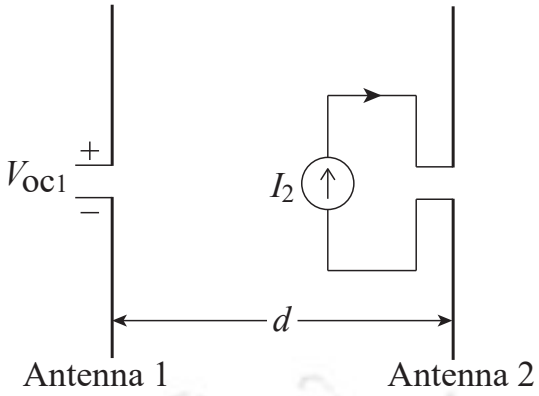

Fig. A.4: The circuit diagram for defining the mutual impedance.

$$= \frac{\text{the coupled voltage across Antenna 1's open circuit terminal}}{\text{the excitation current at Antenna 2's shorted terminal}}$$

$$= \frac{V_{OC1}}{I_2} \mid I_1 = 0, V_{S1} = 0 \tag{A.3}$$

Similarly, Z_{21} can be defined as

$$Z_{21} = \text{the mutual impedance seen by Antenna 2 with Antenna 1 excited}$$

$$= \frac{V_{21}}{I_1} \tag{A.4}$$

$$= \frac{\text{the coupled voltage across Antenna 2's open circuit terminal}}{\text{the excitation current at Antenna 1's shorted terminal}}$$

$$= \frac{V_{OC2}}{I_1} \mid I_2 = 0, V_{S2} = 0 \tag{A.5}$$

Let I_1 and I_2 are the actual terminal current on Antenna 1 and Antenna 2, respectively, with mutual coupling. From Fig. A.3, the following relation can be obtained.

$$I_1 = \frac{V_{S1} - V_{12}}{Z_{11}} \qquad I_2 = \frac{V_{S2} - V_{21}}{Z_{22}} \tag{A.6}$$

Let I_{S1} and I_{S2} are the antenna terminal current with no mutual coupling, i.e., only one antenna

is excited.

$$V_{S1} = Z_{11} I_{S1} \qquad V_{S2} = Z_{22} I_{S2} \tag{A.7}$$

Using (A.2), (A.4), & (A.7), (A.6) can be reduced to (A.8).

$$I_1 = I_{S1} - \frac{Z_{12} I_2}{Z_{11}} \qquad I_2 = I_{S1} - \frac{Z_{21} I_1}{Z_{22}} \tag{A.8}$$

The above expressions can be rearranged as (A.9).

$$I_1 = \frac{1}{D}\left[I_{S1} - Z_{12}^{'} I_{S2}\right] \qquad I_2 = \frac{1}{D}\left[I_{S2} - Z_{21}^{'} I_{S1}\right] \tag{A.9}$$

where

$$Z_{21}^{'} = \frac{Z_{21}}{Z_{22}} \qquad Z_{12}^{'} = \frac{Z_{12}}{Z_{11}} \quad and \quad D = 1 - \frac{Z_{12} Z_{21}}{Z_{22} Z_{11}}$$

The relationship between antenna terminal currents with and without the mutual coupling can be expressed in matrix form as

$$\begin{bmatrix} I_1 \\ I_2 \end{bmatrix} = \frac{1}{D} \begin{bmatrix} 1 & -\frac{Z_{21}}{Z_{22}} \\ -\frac{Z_{12}}{Z_{11}} & 1 \end{bmatrix} \begin{bmatrix} I_{S1} \\ I_{S2} \end{bmatrix} \tag{A.10}$$

V_{total1} and V_{total2} along the entire length of Antenna 1 and Antenna 2 can be written as

$$V_{total1} = Z_{11} I_1 \qquad V_{total2} = Z_{22} I_2 \tag{A.11}$$

and

$$V_{total1} = V_{S1} - Z_{12} I_2 \qquad V_{total2} = V_{S2} - Z_{21} I_1 \tag{A.12}$$

Using (A.11), (A.12) can be reduced to (A.13), as given below.

$$V_{total1} = V_{S1} - \frac{Z_{12}}{Z_{22}} V_{total2} \qquad V_{total2} = V_{S2} - \frac{Z_{21}}{Z_{11}} V_{total1} \tag{A.13}$$

The matrix form of (A.13) can be written as following.

$$\begin{bmatrix} V_{S1} \\ V_{S2} \end{bmatrix} = \begin{bmatrix} 1 & \frac{Z_{12}}{Z_{22}} \\ \frac{Z_{21}}{Z_{11}} & 1 \end{bmatrix} \begin{bmatrix} V_{total1} \\ V_{total2} \end{bmatrix} \tag{A.14}$$

$$[V_{total}] = [Z^t]^{-1}[Vs] \tag{A.15}$$

Here,

$$\begin{bmatrix} V_{S1} \\ V_{S1} \end{bmatrix} = V_S = \text{the uncoupled excitation voltage vector}$$

$$\begin{bmatrix} V_{total1} \\ V_{total2} \end{bmatrix} = V_{total} = \text{the coupled excitation voltage vector}$$

$$Z^t = \begin{bmatrix} 1 & \frac{Z_{12}}{Z_{22}} \\ \frac{Z_{21}}{Z_{11}} & 1 \end{bmatrix}$$

A.2 Mutual Coupling Mechanism in a Receiving MIMO Antenna

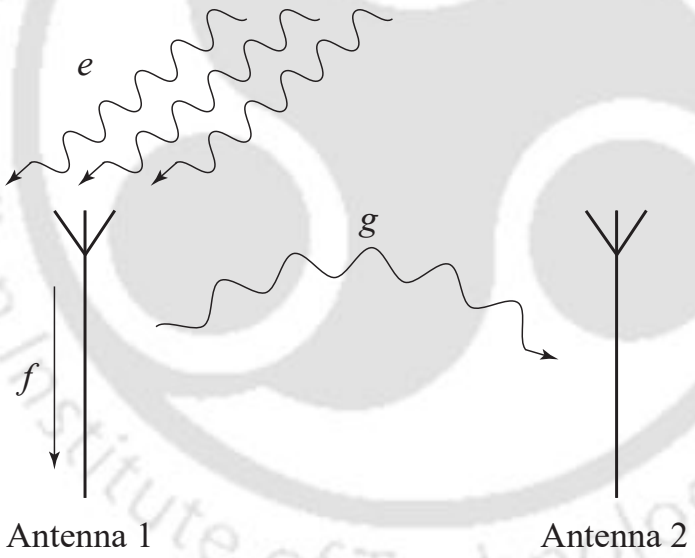

Fig. A.5: A MIMO antenna system with two elements in the receiving mode.

Ideally, in receiving mode, all antenna elements are supposed only to receive the signal, but this is not the case in a practical scenario. As depicted in Fig. A.5, the antenna elements receive the electromagnetic (EM) waves and convert them into an electrical signal. Assuming that the power of the incident EM waves on Antenna 1 is e. A significant part of this incident power gets converted to electrical power (labeled as f). However, a small part of the incident power gets scattered back by Antenna 1, labeled as g. Due to its proximity to Antenna 1,

Antenna 2 partially collects this scattered power because of the mutual coupling. Similarly, Antenna 2 also re-scatters some portion of the received energy, which is subsequently received by Antenna 1. The same process is followed when EM waves are incident over Antenna 2. Now considering that both the antennas receive simultaneously, as shown in Fig. A.6. In that case, the total signal received by the antenna array will be the sum of the signal received by individual antennas and the sum of the signal received because of the mutual coupling effect between them [8, 9].

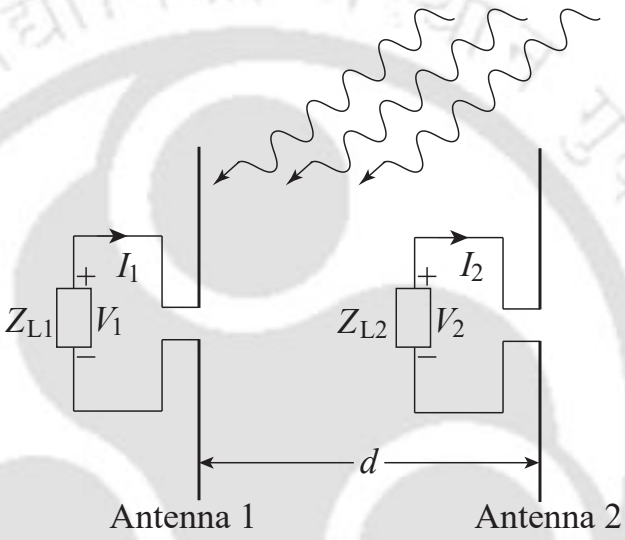

Fig. A.6: A MIMO antenna system comprising two dipole antennas in the receiving mode.

It should be noted the coupling paths between elements of a MIMO antenna during the transmitting and receiving modes are different. In addition, the excitation of the transmitting and receiving MIMMO antenna are not the same, thus having different mechanisms that cause the mutual coupling. Therefore, the problem of mutual coupling for antenna arrays should be treated differently for the transmitting and receiving antenna modules [9].

An antenna system with two dipole antennas is considered in Fig A.6 for analyzing and modeling the mutual coupling in receiving mode [10]. Note that Fig. A.6 depicts the reception of the signal with both antennas, whereas Fig. A.7 illustrates the signal reception in the standalone case for each antenna. The notations used in these figures are as follows:

Z_{L1}: is the termination load connected to Antenna 1.

Z_{L2}: is the termination load connected to Antenna 2.

I_1: is the terminal current in Antenna 1.

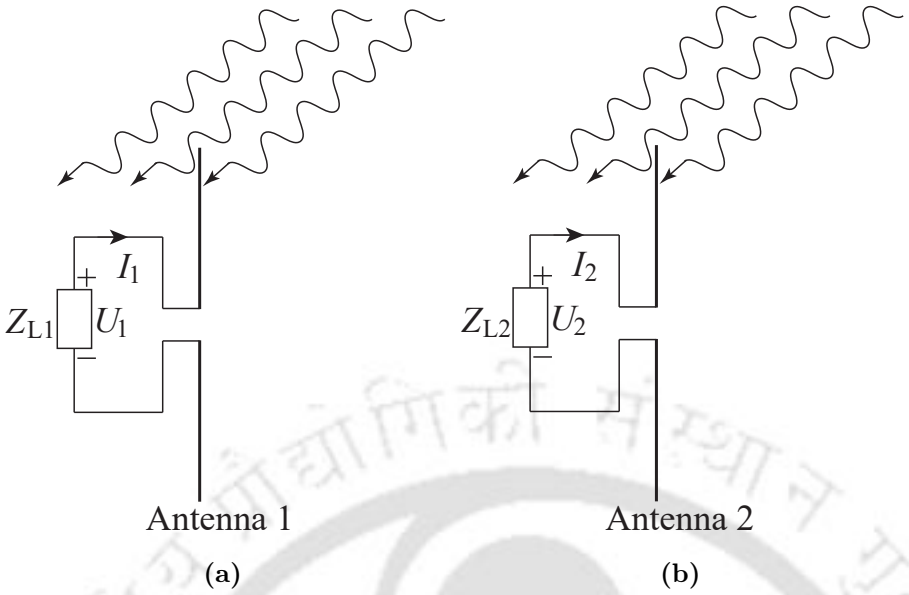

Fig. A.7: Antennas receiving in the stand alone mode: (a) only Antenna 1, (b) only Antenna 2.

I_2: is the terminal current in Antenna 2.

V_1: is the measured voltage at Antenna 1's terminal in the presence of dipole 2.

V_2: is the measured voltage at Antenna 2's terminal in the presence of dipole 1.

U_1: is the measured voltage at Antenna 1's terminal in the absence of dipole 2.

U_2: is the measured voltage at Antenna 2's terminal in the absence of dipole 2.

Let V_{12} and V_{21} be the coupled voltage at the antenna load terminals of Antenna 1 and Antenna 2, respectively. Using Figs. A.6 and A.7, the following expressions can be obtained.

$$V_1 = U_1 + V_{12} \qquad V_2 = U_2 + V_{12} \tag{A.16}$$

$$V_1 = U_1 + Z_{12}I_2 \qquad V_2 = U_1 + Z_{21}I_1 \tag{A.17}$$

$$I_1 = -\frac{V_1}{Z_{L1}} \qquad I_2 = -\frac{V_2}{Z_{L2}} \tag{A.18}$$

The above expressions can be reduced as (A.19).

$$U_1 = V_1 + V_2\frac{Z_{12}}{Z_{L2}} \qquad U_2 = V_2 + V_1\frac{Z_{21}}{Z_{L1}} \tag{A.19}$$

The matrix form of (A.19) can be written as given below.

$$\begin{bmatrix} U_1 \\ U_2 \end{bmatrix} = \begin{bmatrix} 1 & \frac{Z_{12}}{Z_{L1}} \\ \frac{Z_{21}}{Z_{L1}} & 1 \end{bmatrix} \begin{bmatrix} V_1 \\ V_2 \end{bmatrix} \tag{A.20}$$

$$[V] = [Z^r]^{-1}[U] \tag{A.21}$$

Here,

$$\begin{bmatrix} V_1 \\ V_2 \end{bmatrix} = V = \textit{the coupled received voltage vector}$$

$$\begin{bmatrix} U_1 \\ U_2 \end{bmatrix} = U = \textit{the uncoupled received voltage vector}$$

$$Z^r = \begin{bmatrix} 1 & \frac{Z_{12}}{Z_{L1}} \\ \frac{Z_{21}}{Z_{L1}} & 1 \end{bmatrix}$$

Using (A.19), **mutual impedances** Z_{21} and Z_{12} can be defined as given below [10].

$$Z_{21} = \frac{U_2 - V_2}{V_1} Z_{L1} \qquad Z_{12} = \frac{U_1 - V_1}{V_2} Z_{L2} \tag{A.22}$$

A.3 Effect of Mutual Coupling on Radiation Pattern

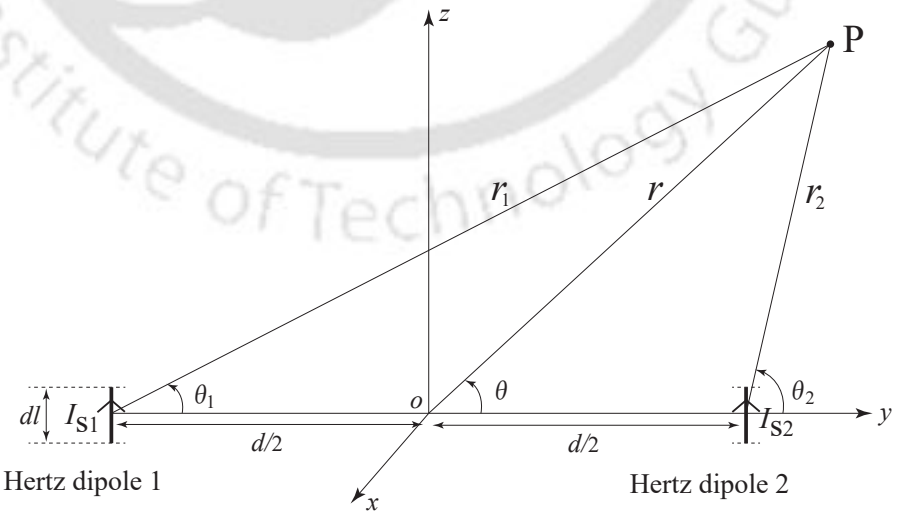

Fig. A.8: A MIMO antenna system comprising two Hertz dipoles in the transmitting mode.

The mutual coupling effect changes the net excitation current of the antenna element, which in turn changes its radiation pattern. Hence, the radiation pattern of a multiple antenna system would change as the individual antennas' radiation patterns change. To understand the same, an antenna system comprising two Hertz dipoles (shown in Fig. A.8) is considered. A Hertz dipole is an infinitesimally small current element of length dl. Let I_{S1} and I_{S2} be the excitation current in the Hertz dipole 1 and Hertz dipole 2, respectively. The combined E-field radiation by both elements at a point P (in the far-field region), considering the mutual coupling, can be related to the combined E-field radiation without the mutual coupling [16].

$$\vec{E}_{\theta(total)} = \vec{E}_{\theta(1)} + \vec{E}_{\theta(2)} \tag{A.23}$$

$$\vec{E}_{\theta(total)} = j\frac{I_{S1}dl\sin\theta_1 \exp^{-j\beta r_1}\beta^2}{4\pi\epsilon\omega r_1} + j\frac{jI_{S2}dl\sin\theta_2 \exp^{-j\beta r_2}\beta^2}{4\pi\epsilon\omega r_2} \tag{A.24}$$

For a point P lying in the far-field region, the following assumptions are taken:

$$\theta_1 \equiv \theta_2 \equiv \theta \tag{A.25}$$

For phase variation,

$$r_1 \equiv r + \frac{d}{2}cos\theta \qquad\qquad r_2 \equiv r - \frac{d}{2}cos\theta \tag{A.26}$$

For amplitude variation,

$$r_1 \equiv r_1 \equiv r \tag{A.27}$$

(A.24) reduces to (A.28) using (A.25), (A.26), and (A.27).

$$\vec{E}_{\theta(total)} = j\frac{dl\exp^{-j\beta r}\sin\theta\beta^2}{4\pi\epsilon\omega r}\left(Is_1\exp^{-j\frac{d}{2}cos\theta} + Is_2\exp^{+j\frac{d}{2}cos\theta}\right) \tag{A.28}$$

The above expression defines the radiation pattern considering no mutual coupling. Let I_1 and I_2 are the current distribution in the Hertz dipole 1 and Hertz dipole 2 considering the mutual coupling. Using (A.28), the electric field vector can be written as

$$\vec{E}_{\theta(total-mc)} = j\frac{j\exp^{-j\beta r}\sin\theta\beta^2}{4\pi\epsilon\omega r}\left(I_1\exp^{-j\frac{d}{2}cos\theta} + I_2\exp^{+j\frac{d}{2}cos\theta}\right) \tag{A.29}$$

Using (A.29) and (A.9) from section A.1, $\vec{E}_{\theta(total)}$ for this two-element MIMO antenna

system with the mutual coupling can be written as

$$\begin{aligned}\vec{E}_{\theta(total-mc)} = j\frac{\exp^{-j\beta r}\sin\theta\beta^2}{4\pi\epsilon\omega r D}\left[\left(Is_1 - Z'_{12}Is_2\right)\exp^{-j\frac{d}{2}cos\theta} + \right.\\ \left.\left(Is_2 - Z'_{21}Is_1\right)\exp^{+j\frac{d}{2}cos\theta}\right]\\ = \frac{B}{D}\left[(Is_1)\exp^{-j\frac{d}{2}cos\theta} + (Is_2)\exp^{+j\frac{d}{2}cos\theta}\right] -\\ \frac{B}{D}\left[\left(Z'_{12}Is_2\right)\exp^{-j\frac{d}{2}cos\theta} + \left(Z'_{21}Is_1\right)\exp^{+j\frac{d}{2}cos\theta}\right]\end{aligned} \tag{A.30}$$

where

$$B = \frac{j\exp^{-j\beta r}\sin\theta\beta^2}{4\pi\epsilon\omega r}$$

$$D = 1 - \frac{Z_{12}Z_{21}}{Z_{22}Z_{11}}$$

Using (A.28) and (A.30),

$$\vec{E}_{\theta(total-mc)} = \frac{\vec{E}_{\theta(total)}}{D} + Other\ terms \tag{A.31}$$

Here,

$$Other\ terms = -\frac{B}{D}\left[\left(Z'_{12}Is_2\right)\exp^{-j\frac{d}{2}cos\theta} + \left(Z'_{21}Is_1\right)\exp^{+j\frac{d}{2}cos\theta}\right]$$

Note that, $\vec{E}_{\theta(total-mc)}$ denotes the total electric field vector considering the mutual coupling and $\vec{E}_{\theta(total)}$ denotes the total electric field vector with no mutual coupling. Similarly,

$$\vec{H}_{\phi(total-mc)} = \frac{\vec{H}_{\phi(total)}}{D} + Other\ terms \tag{A.32}$$

Here,

$$Other\ terms = -\frac{C}{D}\left[\left(Z'_{12}Is_2\right)\exp^{-j\frac{d}{2}cos\theta} + \left(Z'_{21}Is_1\right)\exp^{+j\frac{d}{2}cos\theta}\right]$$

$$C = \frac{j\exp^{-j\beta r}\sin\theta\beta}{4\pi r}$$

$$D = 1 - \frac{Z_{12}Z_{21}}{Z_{22}Z_{11}}$$

A.4 Mutual Coupling Compensation by Considering the Modified Channel Matrix

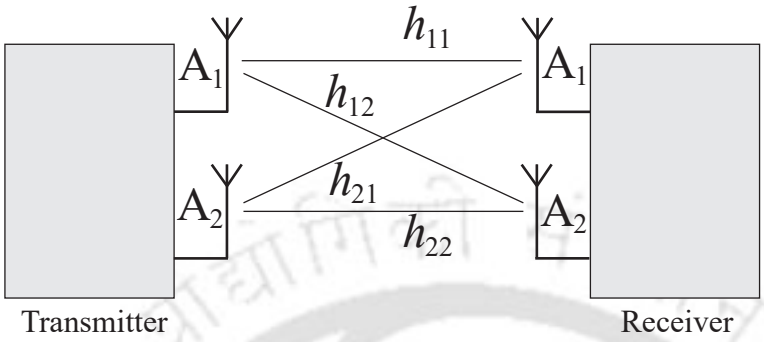

Fig. A.9: A 2×2 MIMO communication channel model.

The mutual coupling effect can be compensated by considering the modified channel matrix. To illustrate the same, let us consider a 2×2 MIMO system as shown in Fig. A.9 where channel matrix H can be given by

$$H = \begin{bmatrix} h_{11} & h_{12} \\ h_{21} & h_{22} \end{bmatrix} \tag{A.33}$$

Let the transmitted voltage vector from the transmitter is given by

$$V^t = \begin{bmatrix} V_1^t \\ V_2^t \end{bmatrix} \tag{A.34}$$

The actual transmitted voltage vector with mutual coupling can be given by (A.35) using (A.15).

$$[V^t_{actual}] = [Z^t]^{-1}[V^t] \tag{A.35}$$

At the receiver side, the actual received voltage with mutual coupling is given by

$$\begin{aligned} [V^r_{actual}] &= [H][V^t_{actual}] \\ [V^r_{actual}] &= [H][Z^t]^{-1}[V^t] \end{aligned} \tag{A.36}$$

The received voltage vector with no mutual coupling on receiver side can be given by using

(A.21).

$$[V^r] = [Z^r][V^r_{actual}] \tag{A.37}$$

Thus, using (A.36) and (A.37),

$$[V^r] = [Z^r][H][Z^t]^{-1}[V^t] \tag{A.38}$$

and

$$[V^r] = [H_{mutual-coupling}][V^t] \tag{A.39}$$

Hence, comparing (A.38) and (A.39),

$$H_{mutual-coupling} = [Z^r][H][Z^t]^{-1} \tag{A.40}$$

Here, $[Z^t]$ and $[Z^r]$ are the same as given in (A.15) and (A.21), respectively.

In this way, by using the circuit theoretic approach, the effect of mutual coupling can be compensated by considering the modified channel matrix.

Bibliography

[1] M. A. Jensen and J. W. Wallace, "A review of antennas and propagation for MIMO wireless communications", *IEEE Transactions on Antennas and Propagation*, vol. 52, no. 11, pp. 2810–2824, 2004.

[2] L. Zheng and D. N. C. Tse., "Diversity and multiplexing: a fundamental tradeoff in multiple-antenna channels", *IEEE Transactions on Information Theory*, vol. 49, no. 5, pp. 1073-1096, 2003.

[3] D. Tse and P. Viswanath, "*Fundamentals of Wireless Communication*", Cambridge University Press, 2005.

[4] S. Schindler, H. Mellein, "Assessing a MIMO channel white paper", Rohdge and Schwarz App Note, 2011.

[5] E. Biglieri, R. Calderbank, A. Constantinides, A. Goldsmith, A. Paulraj, and H. V. Poor, *MIMO Wireless Communications*, Cambridge, UK: Cambridge University Press, 2007.

[6] R. S. Kshetrimayum, *Fundamentals of MIMO Wireless Communications*. Cambridge, UK: Cambridge University Press, 2017.

[7] M. S. Sharawi, *Printed MIMO Antenna Engineering*. Artech House, 2014.

[8] C. A. Balanis, *Antenna Theory: Analysis and Design*. John Wiley & Sons, 2015.

[9] H. S. Lui, H. T. Hui, and M. S. Leong, "A note on the mutual-coupling problems in transmitting and receiving antenna arrays", *IEEE Antennas and Propagation Magazine*, vol. 51, no. 5, pp. 171–176, Oct 2009.

[10] H. T. Hui, "A new definition of mutual impedance for application in dipole receiving antenna arrays", *IEEE Antennas and Wireless Propagation Letters*, vol. 3, pp. 364-367, 2004.

[11] G. Dubost, "Influence of surface wave upon efficiency and mutual coupling between rectangular microstrip antennas", in *Proc. International Symposium on Antennas and Propagation*, Merging Technologies for the 90's, 1990, pp. 660–663.

[12] N. Dodov and P. Petkov, "The surface waves, impact on the coupling effect in microstrip antennas", *Electronics Letters*, vol. 31, pp. 792–793, 1996.

[13] D. R. Jackson, "Reduced surface wave microstrip antennas", in *Handbook of Antenna Technologies*, Z. N. Chen, D. Liu, H. Nakano, X. Qing, and T. Zwick, Eds. Springer Singapore: Springer Singapore, 2016, pp. 1933–1968.

[14] M. S. Sharawi, "Current misuses and future prospects for printed multiple-input, multiple-output antenna systems [wireless corner]", *IEEE Antennas and Propagation Magazine*, vol. 59, no. 2, pp. 162–170, 2017.

[15] M. Khayat, J. Williams, D. Jackson, and S. Long, "Mutual coupling between reduced surface-wave microstrip antennas", *IEEE Transactions on Antennas and Propagation*, vol. 48, no. 10, pp. 1581–1593, 2000.

[16] R. S. Kshetrimayum, *Electromagnetic Field Theory*, Cambridge University Press. Cengage Learning, 2012.

[17] R. Vaughan and J. Andersen, "Antenna diversity in mobile communications," *IEEE Transactions on Vehicular Technology*, vol. 36, no. 4, pp. 149–172, 1987.

[18] M. S. Sharawi, A. T. Hassan, and M. U. Khan, "Correlation calculations for MIMO antenna systems: a comparative study," *International Journal of Microwave and Wireless Technology*, vol. 9, no. 10, pp. 1991-2004, Sept. 2017.

[19] S. F. Roslan, M. R. Kamarudin, M. Khalily, and M. H. Jamaluddin, "An MIMO rectangular dielectric resonator antenna for 4G applications," *IEEE Antennas and Wireless Propagation Letters*, vol. 13, pp. 321-324, Feb. 2014.

[20] A. J. Alazemi and A. Iqbal, "A high data rate implantable MIMO antenna for deep implanted biomedical devices," *IEEE Transactions on Antennas and Propagation*, vol. 70, no. 2, pp. 998-1007, Feb. 2022.

[21] R. Chandel, A. K. Gautam, and K. Rambabu, "Tapered fed compact UWB MIMO-diversity antenna with dual band-notched characteristics," *IEEE Transactions on Antennas and Propagation*, vol. 66, no. 4, pp. 1677-1684, April 2018.

[22] M. T. Ivrlac and J. A. Nossek, "Quantifying diversity and correlation in Rayleigh fading MIMO communication systems," in *Proceedings of the 3rd IEEE International Symposium on Signal Processing and Information Technology*, 2003, pp. 158-161.

[23] S. H. Chae, S. Oh, and S. Park, "Analysis of mutual coupling, correlations, and TARC in WiBro MIMO array antenna," *IEEE Antennas and Wireless Propagation Letters*, vol. 6, pp. 122-125, 2007.

[24] M. Matthaiou, C. Zhong, M. R. McKay, and T. Ratnarajah, "Sum rate analysis of ZF receivers in distributed MIMO systems," *IEEE Journal on Selected Areas in Communication*, vol. 31, no. 2, pp. 180-191, Feb. 2013.

[25] H. S. Lui and H. T. Hui, "Mutual coupling compensation for direction finding using receiving mutual impedance." in *Proc. International Symposium on Antennas and Propagation*, pp. 61-62, 2014.

[26] F. Yang and Y. Rahmat-Samii, *Electromagnetic Band Gap Structures in Antenna Engineering*. Cambridge University Press, Cambridge, UK, 2009.

[27] F. Yang and Y. Rahmat-Samii, "Microstrip antennas integrated with electromagnetic bandgap (EBG) structures: A low mutual coupling design for array applications," *IEEE Transactions on Antennas and Propagation*, vol. 51, no. 10, pp. 2936–2946, 2003.

[28] F. Caminita, S. Costanzo, G. Di Massa, G. Guarnieri, S. Maci, G. Mauriello, and I. Venneri, "Reduction of patch antenna coupling by using a compact EBG formed by shorted strips with interlocked branch-stubs," *IEEE Antennas and Wireless Propagation Letters*, vol. 8, pp. 811–814, 2009.

[29] H. S. Farahani, M. Veysi, M. Kamyab, and A. Tadjalli, "Mutual coupling reduction in patch antenna arrays using a UC-EBG superstrate," *IEEE Antennas and Wireless Propagation Letters*, vol. 9, pp. 57–59, 2010.

[30] Y. Liu, X. Yang, Y. Jia, and Y. J. Guo, "A low correlation and mutual coupling MIMO antenna," *IEEE Access*, vol. 7, pp. 127 384–127 392, 2019.

[31] Y.-F. Cheng, X. Ding, W. Shao, and B.-Z. Wang, "Reduction of mutual coupling between patch antennas using a polarization-conversion isolator," *IEEE Antennas and Wireless Propagation Letters*, vol. 16, pp. 1257–1260, 2017.

[32] M. Alibakhshikenari, M. Khalily, B. S. Virdee, C. H. See, R. A. Abd-Alhameed, and E. Limiti, "Mutual coupling suppression between two closely placed microstrip patches using EM-bandgap metamaterial fractal loading," *IEEE Access*, vol. 7, pp. 23 606–23 614, 2019.

[33] M. Niroo-Jazi, T. A. Denidni, M. R. Chaharmir, and A. R. Sebak, "A hybrid isolator to reduce electromagnetic interactions between Tx/Rx antennas," *IEEE Antennas and Wireless Propagation Letters*, vol. 13, pp. 75-78, 2014.

[34] G. Zhai, Z. N. Chen, and X. Qing, "Enhanced isolation of a closely spaced four-element MIMO antenna system using metamaterial mushroom," *IEEE Transactions on Antennas and Propagation*, vol. 63, no. 8, pp. 3362–3370, 2015.

[35] D. Guha and Y. M. Antar, Microstrip and Printed Antennas: New Trends, Techniques and Applications. John Wiley & Sons, 2011.

[36] J. OuYang, F. Yang, and Z.Wang, "Reducing mutual coupling of closely spaced microstrip MIMO antennas for WLAN application," *IEEE Antennas and Wireless Propagation Letters*, vol. 10, pp. 310–313, 2011.

[37] M. A. Abdalla and A. A. Ibrahim, "Compact and closely spaced metamaterial MIMO antenna with high isolation for wireless applications," *IEEE Antennas and Wireless Propagation Letters*, vol. 12, pp. 1452–1455, 2013.

[38] H. Xing, X. Wang, Z. Gao, X. An, H.-x. Zheng, M. Wang, and E. Li, "Efficient isolation of an MIMO antenna using defected ground structure," *Electronics*, vol. 9, no. 8, p. 1265, 2020.

[39] A. Diallo, C. Luxey, P. Le Thuc, R. Staraj, and G. Kossiavas, "Study and reduction of the mutual coupling between two mobile phone PIFAs operating in the DCS1800 and UMTS Bands," *IEEE Transactions on Antennas and Propagation*, vol. 54, no. 11, pp. 3063–3074, 2006.

[40] Y. Wang and Z. Du, "A wideband printed dual-antenna system with a novel neutralization line for mobile terminals," *IEEE Antennas and Wireless Propagation Letters*, vol. 12, pp. 1428–1431, 2013.

[41] Y.Wang and Z. Du, "A wideband printed dual-antenna with three neutralization lines for mobile terminals," *IEEE Transactions on Antennas and Propagation*, vol. 62, no. 3, pp. 1495–1500, 2014.

[42] A. Cihangir, F. Ferrero, G. Jacquemod, P. Brachat, and C. Luxey, "Neutralized coupling elements for MIMO operation in 4G mobile terminals," *IEEE Antennas and Wireless Propagation Letters*, vol. 13, pp. 141–144, 2014.

[43] S. Wang and Z. Du, "Decoupled dual-antenna system using crossed neutralization lines for LTE/WWAN smartphone applications," *IEEE Antennas and Wireless Propagation Letters*, vol. 14, pp. 523–526, 2015.

[44] Y. Yu, L. Yi, X. Liu, and Z. Gu, "Compact dual-frequency microstrip antenna array with increased isolation using neutralization lines," *Progress In Electromagnetics Research Letters*, vol. 56, pp. 95–100, 2015.

[45] S. Zhang and G. F. Pedersen, "Mutual coupling reduction for UWB MIMO antennas with a wideband neutralization line," *IEEE Antennas and Wireless Propagation Letters*, vol. 15, pp. 166–169, 2016.

[46] H. Wang, L. Liu, Z. Zhang, Y. Li, and Z. Feng, "Ultra-compact three-port MIMO antenna with high isolation and directional radiation patterns," *IEEE Antennas and Wireless Propagation Letters*, vol. 13, pp. 1545–1548, 2014.

[47] K.-L. Wu, C. Wei, X. Mei, and Z.-Y. Zhang, "Array-antenna decoupling surface," *IEEE Transactions on Antennas and Propagation*, vol. 65, no. 12, pp. 6728–6738, 2017.

[48] F. Liu, J. Guo, L. Zhao, G.-L. Huang, Y. Li, and Y. Yin, "Dual-band metasurface-based decoupling method for two closely packed dual-band antennas," *IEEE Transactions on Antennas and Propagation*, vol. 68, no. 1, pp. 552–557, 2020.

[49] F. Liu, J. Guo, L. Zhao, H. Luyu, G. Huang, Y. Li, and Y. Yin, "Ceramic superstrate-based decoupling method for two closely packed antennas with cross-polarization suppression," *IEEE Transactions on Antennas and Propagation*, vol. 69, no. 3, pp. 1751–1756, 2021.

[50] J. Tang, F. Faraz, X. Chen, Q. Zhang, Q. Li, Y. Li, and S. Zhang, "A metasurface superstrate for mutual coupling reduction of large antenna arrays," *IEEE Access*, vol. 8, pp. 126 859–126 867, 2020.

[51] A. Jafargholi, A. Jafargholi, and J. H. Choi, "Mutual coupling reduction in an array of patch antennas using CLL metamaterial superstrate for MIMO applications," *IEEE Transactions on Antennas and Propagation*, vol. 67, no. 1, pp. 179–189, 2018.

[52] M. Li, M. Y. Jamal, L. Jiang, and K. L. Yeung, "Isolation enhancement for MIMO patch antennas sharing a common thick substrate: Using a dielectric block to control space-wave coupling to cancel surface-wave coupling," *IEEE Transactions on Antennas and Propagation*, vol. 69, no. 4, pp. 1853–1863, 2020.

[53] A. Petosa, *Dielectric Resonator Antenna Handbook*. Artech House, 2007.

[54] J. Yan and J. T. Bernhard, "Design of a MIMO dielectric resonator antenna for LTE femtocell base stations," *IEEE Transactions on Antennas and Propagation*, vol. 60, no. 2, pp. 438–444, Feb. 2012.

[55] S. F. Roslan, M. R. Kamarudin, M. Khalily, and M. H. Jamaluddin, "An MIMO rectangular dielectric resonator antenna for 4G applications," *IEEE Antennas and Wireless Propagation Letters*, vol. 13, pp. 321-324, Feb. 2014.

[56] Y. Gao, Z. Feng, and L. Zhang, "Compact CPW-fed dielectric resonator antenna with dual polarization," *IEEE Antennas and Wireless Propagation Letters*, vol. 10, pp. 544-547, June 2011.

[57] L. Zou, D. Abbott, and C. Fumeaux, "Omnidirectional cylindrical dielectric resonator antenna with dual polarization," *IEEE Antennas and Wireless Propagation Letters*," vol. 11, pp. 515-518, May 2012.

[58] A. Dadgarpour, B. Zarghooni, B. S. Virdee, T. A. Denidni, and A. A. Kishk, "Mutual coupling reduction in dielectric resonator antennas using metasurface shield for 60 GHz MIMO systems," *IEEE Antennas and Wireless Propagation Letters*, vol. 16, pp. 477–480, Mar. 2017.

[59] R. Karimian, A. Kesavan, M. Nedil, and T. A. Denidni, "Low mutual coupling 60-GHz MIMO antenna system with frequency selective surface wall," *IEEE Antennas and Wireless Propagation Letters*, vol. 16, pp. 373–376, Mar. 2017.

[60] M. J. Al-Hasan, T. A. Denidni, and A. R. Sebak, "Millimeter-wave compact EBG structure for mutual coupling reduction applications," *IEEE Transactions on Antennas and Propagation*, vol. 63, no. 2, pp. 823–828, Feb. 2015.

[61] M. S. Sharawi, S. K. Podilchak, M. U. Khan, and Y. M. Antar, "Dual-frequency DRA-based MIMO antenna system for wireless access points," *IET Microwaves, Antennas & Propagation*, vol. 11, no. 8, pp. 1174–1182, May 2017.

[62] G. Das, A. Sharma, R. K. Gangwar, and M. S. Sharawi, "Performance improvement of multiband MIMO dielectric resonator antenna system with a partially reflecting surface," *IEEE Antennas and Wireless Propagation Letters*, vol. 18, no. 10, pp. 2105-2109, Oct. 2019.

[63] M. Li and S. Cheung, "Isolation enhancement for MIMO dielectric resonator antennas using dielectric superstrate," *IEEE Transactions on Antennas and Propagation*, vol. 69, no. 7, pp. 4154-4159, July 2021.

[64] I. Messaoudene, S. Aidel, T. A. Denidni, and A. A. Kishk, "Quarter cylindrical dielectric resonator antenna with circular polarization for wideband MIMO systems," *Electronics Letters*, Vol. 56, no. 4, pp. 174-176, Feb. 2020.

[65] D. Guha, S. Biswas, T. Joseph, and M. Sebastian, "Defected ground structure to reduce mutual coupling between cylindrical dielectric resonator antennas," *Electronics Letters*, vol, 44, no. 14, pp, 836-837, 2008.

[66] A. Sharma and A. Biswas, "Wideband multiple-input–multiple-output dielectric resonator antenna," *IET Microwaves, Antennas & Propagation*, vol. 11, no. 4, pp. 496–502, 2017.

[67] G. Das, A. Sharma, R. K. Gangwar, and M. S. Sharawi, "Triple-port, two-mode based two element cylindrical dielectric resonator antenna for MIMO applications," *Microwave and Optical Technology Letters*, vol. 60, no. 6, pp. 1566–1573, 2018.

[68] A. Sharma, A. Sarkar, A. Biswas, and M. J. Akhtar, "A-shaped wideband dielectric resonator antenna for wireless communication systems and its MIMO implementation," *International Journal of RF and Microwave Computer-Aided Engineering*, vol. 28, no. 8, p. e21402, 2018.

[69] A. Abdalrazik, A. S. A. El-Hameed, and A. B. Abdel-Rahman, "A three port MIMO dielectric resonator antenna using decoupled modes," *IEEE Antennas and Wireless Propagation Letters*, vol. 16, pp. 3104-3107, 2017.

[70] Y. Zhang, J.-Y. Deng, M.-J. Li, D. Sun, and L.-X. Guo, "A MIMO dielectric resonator antenna with improved isolation for 5G mm-wave applications," *IEEE Antennas and Wireless Propagation Letters*, vol. 18, no. 4, pp. 747–751, 2019.

[71] Y. M. Pan, X. Qin, Y. X. Sun, and S. Y. Zheng, "A simple decoupling method for 5G millimeter-wave MIMO dielectric resonator antennas," *IEEE Transactions on Antennas and Propagation*, vol. 67, no. 4, pp. 2224–2234, 2019.

[72] G. Zhai, Z. N. Chen, and X. Qing, "Mutual coupling reduction of a closely spaced four-element MIMO antenna system using discrete mushrooms," *IEEE Transactions on Microwave Theory and Techniques*, vol. 64, no. 10, pp. 3060–3067, 2016.

[73] K. Kumar and S. Dwari, "Compact four-element MIMO SIW cavity backed slot antenna with high front-to-back ratio," *International Journal of RF and Microwave Computer-Aided Engineering*, vol. 29, no. 1, p.e21512, 2019.

[74] Y. Sung, "Closely spaced MIMO antenna based on substrate-integrated waveguide technology," *Microwave and Optical Technology Letters*, vol. 60, no. 7, pp. 1794–1798, 2018.

[75] B.-J. Niu and Y.-J. Cao, "Bandwidth-enhanced four-antenna MIMO system based on SIW cavity," *Electronics Letters*, vol. 56, no. 13, pp. 643–645, 2020.

[76] S. Nandi and A. Mohan, "A compact eighth-mode circular SIW cavity-based MIMO antenna," *IEEE Antennas and Wireless Propagation Letters*, vol. 20, no. 9, pp. 1834–1838, 2021.

[77] B.-J. Niu and J.-H. Tan, "Compact SIW cavity MIMO antenna with enhanced bandwidth and high isolation," *Electronics Letters*, vol. 55, no. 11, pp. 631–632, 2019.

[78] C.-Y. Chiu, J.-B. Yan, R. D. Murch, J. X. Yun, and R. G. Vaughan, "Design and implementation of a compact 6-port antenna," *IEEE Antennas and Wireless Propagation Letters*, vol. 8, pp. 767–770, 2009.

[79] W. Han, X. Zhou, J. Ouyang, Y. Li, R. Long, and F. Yang, "A six-port MIMO antenna system with high isolation for 5-GHz WLAN access points," *IEEE Antennas and Wireless Propagation Letters*, vol. 13, pp. 880–883, 2014.

[80] Z. Chen, W. Geyi, M. Zhang, and J. Wang, "A study of antenna system for high order MIMO device," *International Journal of Antennas and Propagation*, vol. 2016, 2016.

[81] J. Motohashi and M. Yamamoto, "Design of a wideband 6-port MIMO antenna using leaf-shaped monopole and notch antennas," in Proc. *International Symposium on Antennas and Propagation (ISAP), IEEE*, 2017, pp. 1–2.

[82] G. Kumar and K. Ray, *Broadband Microstrip Antennas*. Artech House Antennas and Propagation Library, ARTECH HOUSE, 2003.

[83] R. Marques, F. Martin, and M. Sorolla, *Metamaterials with Negative Parameters: Theory, Design, and Microwave Applications*. Artech House Antennas and Propagation Library, John Wiley & Sons, 2003.

[84] D. Guha and Y. M. Antar, *Microstrip and Printed Antennas: New Trends, Techniques and Applications*, John Wiley & Sons, 2011.

[85] H. A. Wheeler, "Fundamental limitations of small antennas," *Proceedings of the IRE*, vol. 35, no. 12, pp. 1479–1484, 1947.

[86] C. Y. Huang and J. S. Kuo, "Frequency-adjustable circularly polarized dielectric resonator antenna," *Microwave and Optical Technology Letters*, vol. 34, no. 3, pp. 211–213, 2002.

[87] K. Leung and K. Luk, *Dielectric Resonator Antenna*, Research Studies Press Ltd., Baldock, Inglaterra, Uk, 2003.

[88] D. Guha, A. Banerjee, C. Kumar, and Y. M. M. Antar, "Higher order mode excitation for high-gain broadside radiation from cylindrical dielectric resonator antennas," *IEEE Transactions on Antennas and Propagation*, vol. 60, no. 1, pp. 71-77, Jan. 2012.

[89] A. A. Kishk and W. Huang, "Size-reduction method for dielectric-resonator antennas," *IEEE Antennas and Propagation Magazine*, vol. 53, no. 2, pp. 26-38, Apr. 2011.

[90] G. P. Junker, A. A. Kishk, A. W. Glisson, and D. Kajfez, "Effect of an air gap on a cylindrical dielectric resonator antenna operating in the TM_{01} mode," *Electronics Letters*, vol. 30, no. 2, pp. 97-98, Jan. 1994.

[91] G. P. Junker, A. A. Kishk, A. W. Glisson, and D. Kajfez, "Effect of an air gap around the coaxial probe exciting a cylindrical dielectric resonator antenna," *Electronics Letters*, vol. 30, no. 3, pp. 177-178, Feb. 1994.

[92] M. R. Nikkhah, J. R. Mohassel, and A. A. Kishk, "Compact wideband rectangular dielectric resonator antenna with parasitic elements and air gaps," *Progress In Electromagnetics Research Letters*, vol. 42, pp. 129-139, Sept. 2013.

[93] T. Deckmyn, S. Agneessens, A. C. Reniers, A. B. Smolders, M. Cauwe, D. V. Ginste, and H. Rogier, "A novel 60 GHz wideband coupled half-mode/quarter-mode substrate integrated waveguide antenna," *IEEE Transactions on Antennas and Propagation*, vol. 65, no. 12, pp. 6915-6926, Dec. 2017.

[94] N. Nguyen-Trong and C. Fumeaux, "Half-mode substrate-integrated waveguides and their applications for antenna technology: A Review of the possibilities for antenna design," *IEEE Antennas and Propagation Magazine*, vol. 60, no. 6, pp. 20-31, Dec. 2018.

[95] M. Bozzi, A. Georgiadis, and K. Wu, "Review of substrate-integrated waveguide circuits and antennas," *IET Microwaves, Antennas & Propagation*, vol. 6 no. 8, pp. 909-20, June 2011.

[96] K.-L. Wong, C.-M. Chou, Y.-J. Yang, and K.-Y. Wang, "Multipolarized wideband circular patch antenna for fifth-generation multi-input-multi-output access-point application," *IEEE Antennas and Wireless Propagation Letters*, vol. 18, no. 10, pp. 2184–2188, Oct. 2019.

[97] K.-L. Wong, H.-J. Chang, J.-Z. Chen, and K.-Y. Wang, "Three wideband monopolar patch antennas in a Y-shape structure for 5G multi-input-multi-output access points," *IEEE Antennas and Wireless Propagation Letters*, vol. 19, no. 3, pp. 393–397, Mar. 2020.

[98] K.-L. Wong, J.-Z. Chen, and W.-Y. Li, "Four-port wideband annular ring patch antenna generating four decoupled waves for 5G multi-input-multi-output access points," *IEEE Transactions on Antennas and Propagation*, vol. 69, no. 5, pp. 2946-2951, May 2021.

[99] I. Barani, K. Wong, Y. Zhang, and W. Li, "Low-profile wideband conjoined open-slot antennas fed by grounded coplanar waveguides for 4×4 5G MIMO operation," *IEEE Transactions on Antennas and Propagation*, vol. 68, no. 4, pp. 2646–2657, Apr. 2020.

[100] L. Chang and H. Wang, "Miniaturized wideband four-antenna module based on dual-mode PIFA for 5G 4×4 MIMO applications," *IEEE Transactions on Antennas and Propagation*, vol. 69, no. 9, pp. 5297-5304, Sept. 2021.

[101] L. Wang and Q. Liao, "Wideband multibeam SIW horn array with high beam isolation and full azimuth coverage," *IEEE Transactions on Antennas and Propagation*, vol. 69, no. 9, pp. 6070-6075, Sept. 2021.

[102] L. K. Hady, A. A. Kishk, and D. Kajfez, "Power dividers based on dielectric resonator whispering-gallery modes fed by probe or slot type of coupling," *IEEE Transactions on Microwave Theory and Techniques*, vol. 57, no. 12, part 2, pp. 3404–3409, Dec. 2009.

[103] A. R. Moznebi, K. Afrooz, M. Danaeian, and P. Mousavi, "Four-way filtering power divider using SIW and eighth-mode SIW cavities with ultrawide out-of-band rejection," *IEEE Microwave and Wireless Components Letters*, vol. 29, no. 9, pp. 586-588, Sept. 2019.

[104] A. R. Moznebi, K. Afrooz, M. Danaeian, and P. Mousavi, "Compact filtering power divider based on corrugated third-mode circular SIW cavities," *Microwave and Optical Technology Letters*, vol. 69, no. 5, pp. 1900-1905, Jan. 2020.

[105] D. M. Pozar, *Microwave Engineering*, Third Edition. NewYork, NY, USA: Wiley, 2004.

[106] F. Xu and K. Wu, "Guided-wave and leakage characteristics of substrate integrated waveguide," *IEEE Transactions on Microwave Theory and Techniques*, vol.53, no. 1, pp. 66–73, Jan. 2005.

[107] M. Tecpoyotl-Torres, S. F. Rodriguez-Fuentes, F. S. Franco-Romero, M. A. Velasco-Castillo, J. G. Vera-Dimas, and R. V. Bernal, "Real-time video transmission in an FPV system using patch antennas," in Proc. *2021 International Conference on Mechatronics, Electronics and Automotive Engineering (ICMEAE)*, Cuernavaca, Mexico, 2021, pp. 251-256.

[108] "DJI Digital FPV System." Jun. 24, 2022. [Online]. Available: https//www.dji.com/fpv/info#specs

[109] "Caddx Vista Digital HD System for DJI." Jun. 24, 2022. [Online]. Available: https://www.getfpv.com/caddx-vista-digital-hd-system-for-dji-hd-fpv.html

[110] C. Hausl, J. Emmert, M. Mielke, B. Mehlhorn, and C. Rowell, "Mobile Network Testing of 5G NR FR1 and FR2 Networks: Challenges and Solutions," in Proc. *2022 16th European Conference on Antennas and Propagation (EuCAP)*, 2022, pp. 1-5.

[111] 3GPP TS 38.101-1, *NR; User Equipment (UE) Radio Transmission and Reception; Part 1: Range 1 Standalone*, V16.8.0, June 2021.

Authors' Biography

Department of Electronics and Electrical Engineering
Indian Institute of Technology Guwahati, India-781039

MOHIT MISHRA received the B.Tech. degree in Electronics and Communication Engineering from the Central University of Chhattisgarh, Bilaspur, C.G., India, in 2014. He joined IIT Guwahati in 2015 to pursue a dual degree course (M.S. [Engineering] and Ph.D.). His research interests include Printed MIMO Antennas and Dielectric Resonator Antennas for MIMO applications. Mohit has authored 16 research publications. He is a recipient of the COMSNETS Fellowship 2021. He chaired IIT Guwahati's IEEE Student Branch between May 2018 and July 2019. During this tenure, IEEE Kolkata Section's Best Student Branch Activity Award was given to the IEEE Student Branch, IIT Guwahati, at the STUDENT MEET during IEEE TENSYMP-2019. He previously held key positions in the Students Gymkhana Council, including Chairperson of the Students Senate and Vice-President of the Students Gymkhana Council of IIT Guwahati. He is also an active member of the IEEE APS society. He has been an organizing committee member (Chair, Publicity & Social Media) of the IEEE Microwave Antenna and Propagation Conference (MAPCON) 2022, organized at Bengaluru, India.


Thank you!